Doctoral Thesis

High Performance Cathode Materials for Lithium Ion Batteries

Min-Joon Lee

Department of Energy Engineering

(Battery Science and Technology)

Graduate School of UNIST

2015

High Performance Cathode Materials for Lithium Ion Batteries

Min-Joon Lee

Department of Energy Engineering
(Battery Science and Technology)

Graduate School of UNIST

High Performance Cathode Materials for Lithium Ion Batteries

A dissertation
submitted to the Graduate School of UNIST
in partial fulfillment of the
requirements for the degree of
Doctor of Philosophy

Min-Joon Lee

6. 16. 2015
Approved by

조 재필

Advisor
Jaephil Cho

High Performance Cathode Materials for Lithium Ion Batteries

Min-Joon Lee

This certifies that the dissertation of Min-Joon Lee is approved.

6. 16. 2015

Advisor: Jaephil Cho

Youngsik Kim

Yoon Seok Jung

Nam-Soon Choi

Kvu Tae Lee

CONTENTS

Abstract

With increasing interest in environmental and energy issues, the application fields of lithium ion batteries have been used for electric vehicle as well as portable devices. However, lithium ion batteries with present technology can't fulfill the requirement of full-range electric vehicles due to insufficient energy density and power density. The promising candidates of cathode materials for those drawbacks are Li-rich (Li_2MnO_3-$LiMO_2$, M=Ni, Mn and Co) and spinel (LiM_2O_4, M=Al, Li, Mg, etc.) cathode materials. However, those materials still has problem which should be overcome for application of electric vehicles. For examples, the Li-rich materials have very high gravimetric energy density but suffer from low initial coulombic efficiency, voltage decay upon cycling, large side reaction at elevated temperature and poor rate capability. The spinel cathode materials have high rate capability and thermal stability but suffer from Mn dissolution at elevated temperature. Also it delivers low capacity at high C rate if secondary particle size is large (>10㎛). To overcome this barrier, newly developed material modification methods for Li-rich and spinel cathode materials are proposed in this dissertation.

1) The chemical activation is frequently used to improve the first cycle efficiency for Li-rich material. However, it causes the formation of lithium impurities. Also the surface coating is carried out to reduce side reaction on the surface, but this method can solve the coulombic efficiency at 1st cycle and rate capability. To overcome these barriers, we here report an efficient and effective surface modification method. The chemical activation (acid treatment) and $LiCoPO_4$ coating were carried out simultaneously. During synthesis process, the lithium ions were extracted from the lattice leading to the improved columbic efficiency and these ions were used for the formation of $LiCoPO_4$. The Ni and Co doped spinel phase was formed at the surface of host material, which gives rise to the facile pathway of lithium ions. The $LiCoPO_4$ and highly doped spinel on the surface acted as the double protection layers that effectively prevented side reactions on the surface at 60^{o}C.

2) The surface coating is widely used to protect surface of spinel cathode material from acidic present electrolyte. However, metal compound coatings cause surface resistance because usually coating material is electrically and electrochemically inactive. Also even though the coating material is electrode material, it still has resistance issues due to structural mismatch (grain boundary). To overcome this barrier, we here report an imaginative material design; a novel hetero-structure $LiMn_2O_4$ with epitaxially grown layered ($R\bar{3}m$) surface phase. No defect was observed at the interface between the host spinel and layered surface phase, which provides an efficient path for the ionic and electronic mobility, leading to the improved rate capability. In addition, the layered surface phase protects the host spinel from being directly exposed to the highly active electrolyte at 60 ^{o}C.

3) Many researchers have investigated nanosized spinel cathode materials to increase their rate capability because the lithium diffusion pathway is reduced and the surface where the electrochemical reaction can occur increase. However, the nanosized materials can't fulfill the requirement of electrode density for the application of electric vehicles. Also the carbon coating is not able to be conducted on the spinel cathode materials due to the formation of oxygen deficiency. To overcome these problems, we report composites with super-p and nanosized spinel material via spray drying process. The acid-treated super-p was used for better distribution of super-p in secondary particle. The developed material showed outstanding rate capabilities at -10 ºC as well as 24 ºC.

List of Figures

List of Tables

1. Introduction

1. 1. Lithium-Ion Battery

The needs for energy are still increasing with developing industry and technology, even though the prices of fossil fuel are still being raised and reserves of that is decreasing. Also the environmental pollutions by consuming fossil fuel as the main energy sources are a serious problem that threatens the health of human and conservation of nature. The world have been made to replace the fossil fuels with renewable energy such as hydroelectric power, biofuel, geothermal energy, wind energy, solar energy and etc. However, most of them generate small energy when it doesn't need, so it should be stored in energy storage devices such as batteries.

In the 1980s, information technology (IT) advanced significantly with the development of portable devices such as video cameras, digital cameras, cell phones, laptop computer and so on. The revolution of products led to a demand for rechargeable energy storage devices with higher energy density, reduced size and weight. Conventional rechargeable batteries at that time such as lead acid batteries, Ni-Cd batteries and Ni-MH batteries used aqueous electrolytes, which hindered increasing operating voltage leading to limitations of energy density because the water is decomposed at -1.23 V versus standard hydrogen electrode (SHE).

Li-ion batteries are getting attention as a next generation energy storage devices because it offer a higher volumetric and gravimetric energy density than lead acid batteries, Ni-Cd batteries and Ni-MH batteries regardless of cell types (Figure 1). The reason is believed that lithium is the most electropositive (-3.04 V vs. SHE) and lightest metal (6.94 g mol^{-1}). It also uses the organic electrolytes, which guarantee higher working voltage compared to water electrolyte. The research on the lithium ion batteries started in 1976 with titanium sulfide as a cathode and lithium metal as an anode. Also in 1979, John B. Goodenough first proposed $LiCoO_2$ as a cathode material which is widely used at present. By using LiCoO2/Graphite system, the first commercialization was achieved by SONY in 1991. Since then, the markets and technologies of lithium ion batteries have grown to be the dominant power sources for electric vehicles (EVs) and large-scale energy storage systems (ESSs) as well as portable IT devices.

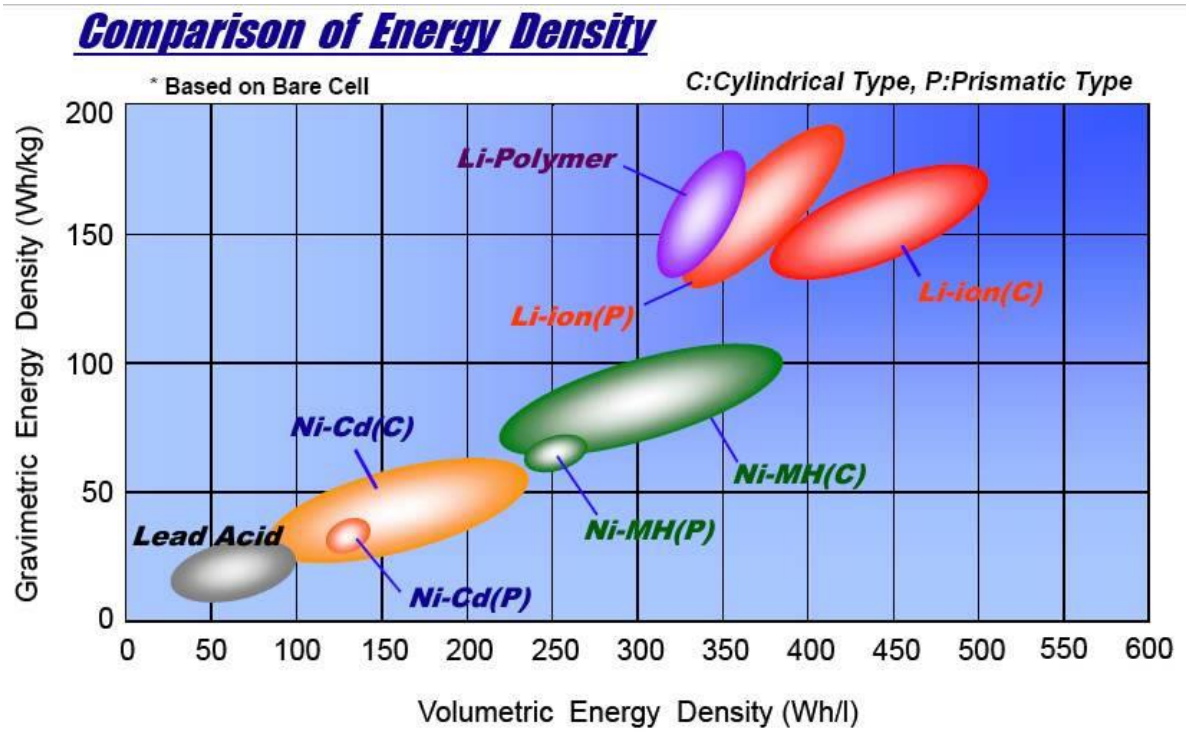

Figure 1.1. Comparison of the gravimetric and volumetric energy densities of various batteries

1. 2. Principle of Lithium-Ion Battery

There are four components of the lithium ion batteries, cathode, anode, electrolyte and separator (Figure 1.2). The lithium ion batteries generally produce an average cell voltage of around 3.7 V and operate on the relatively simple principle of reversible intercalation of Li ions in the cathode and anode. The most widely used and researched materials for the cathode are $LiCoO_2$, $LiMn_2O_4$ and $LiFePO_4$ and some form of carbon like graphite, hard carbon and soft carbon are generally used for the anode. During charge process, lithium ions are released from cathode and diffused to anode through the electrolyte. At the same time, the electrons are moved to anode through external circuit. The reverse reaction occurs during discharge process. The cell reaction mechanisms during charge are as follows;

Cathode electrode: $LiCoO_2 \rightarrow Li_{1-x}CoO_2 + xLi^+ + xe^-$

Anode electrode: $C_6 + xLi^+ + xe^- \rightarrow Li_xC_6$

Overall charge reaction: $LiCoO_2 + C_6 \rightarrow Li_{1-x}CoO_2 + Li_xC_6$

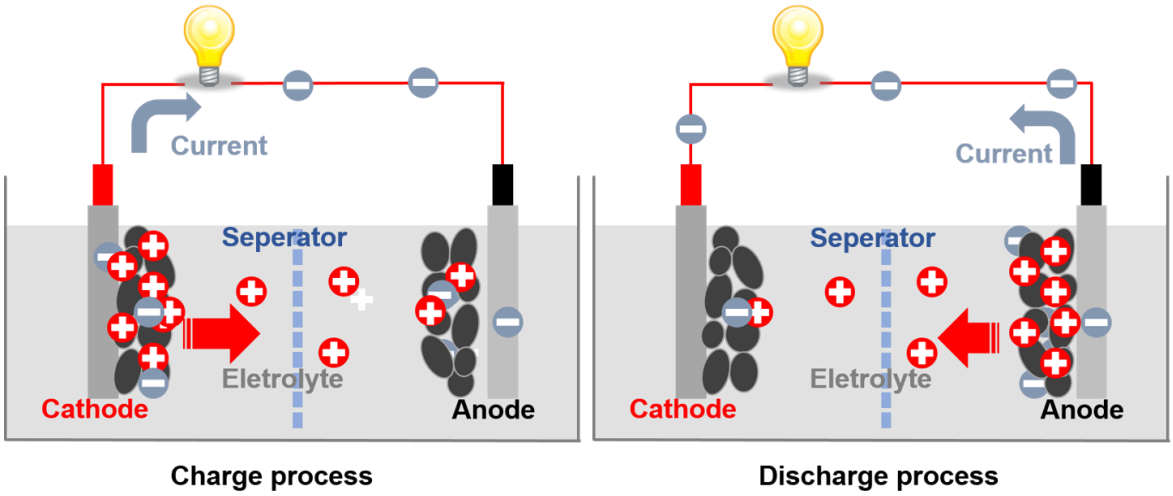

Figure 1.2. Schematic diagram of four components of lithium ion batteries and its charge and discharge process.

The electrochemical reaction of Li-ion batteries therefore involves three reaction steps: i) a mass-transfer reaction for the solid-state diffusion of Li^+ ions in the structure of the electrode materials, ii) a charge-transfer reaction at the interface between the electrode and electrolyte, and iii) Li^+ ion migration in the electrolyte.[2] The electrochemical performance of Li-ion batteries, such as their cycleability and rate capability, is greatly dependent on mass-transfer and charge-transfer reactions.

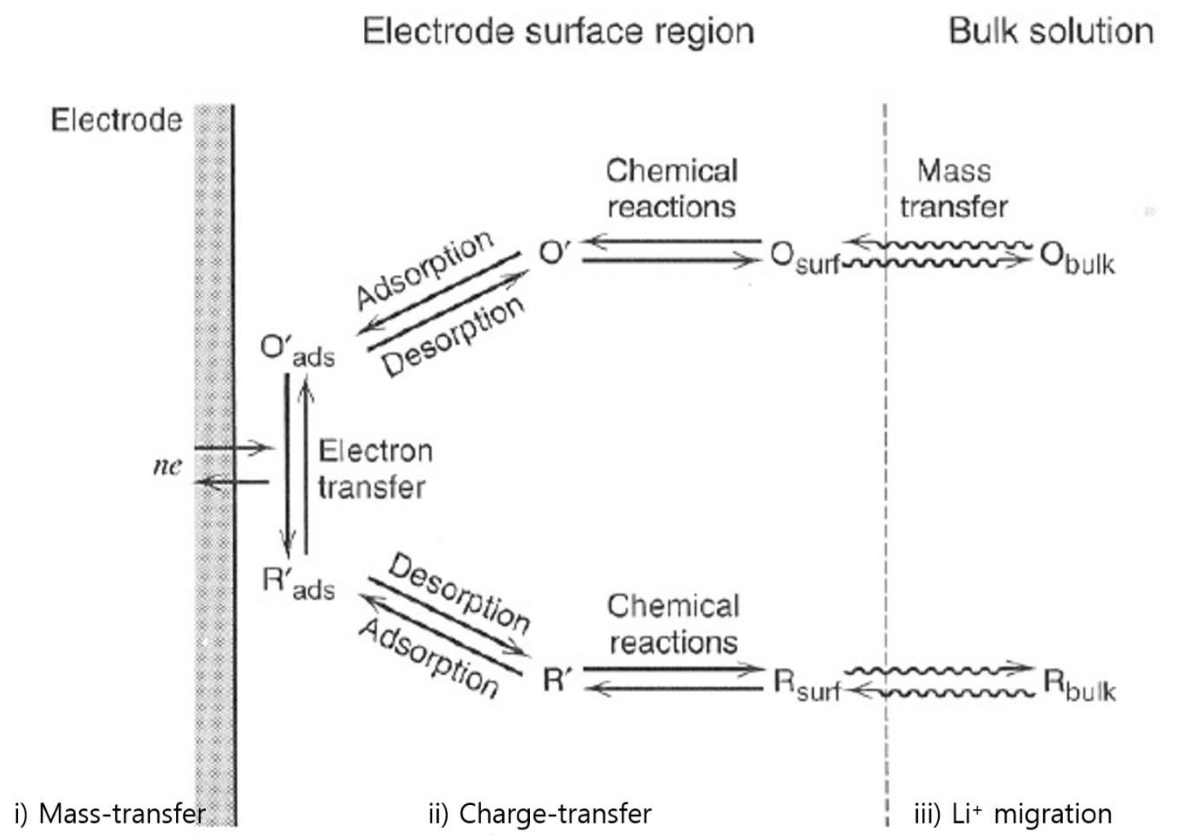

Figure 1.3. Schematic view of electrochemical reaction

2. Cathode Materials

The Cathode materials for lithium ion batteries are transition metal oxide containing lithium, and they are a type of functional ceramics. Also the lithium ions should be able to diffuse freely through the crystal structure. The transition metal ions are oxidized at the charge process and reduced at the discharge process. The operating voltages are dependent on its structure and transition metal ions (Table 2.1).

	$LiCoO_2$	$LiNi_{0.8}Co_{0.15}Al_{0.05}O_2$	$LiFePO_4$	$LiNi_{0.5}Mn_{1.5}O_4$	$LiMn_2O_4$
Structure	**Layered**	**Layered**	**Olivine**	**Spinel**	**Spinel**
Theoretical Capacity(mAh/g)	**274**	**279**	**170**	**147**	**148**
Available Capacity(mAh/g)	**160**	**185**	**150**	**120**	**110**
Operating Voltage(V) (vs. lithium)	**3.9**	**3.6**	**3.4**	**4.7**	**4.0**
Electrode density (g/cc)	**3.7**	**3.3**	**2.6**	**3.2**	**3.2**
Advantage	**High conductivity Easy synthesis**	**High Capacity**	**Good thermal stability**	**High power**	**Good thermal stability Low price High power**
Disadvantage	**High cost Thermal instability**	**Thermal instability**	**Low conductivity**	**Electrolyte Oxidation**	**Mn dissolution**

Table 2.1. Comparison of cathode materials for lithium ion batteries

2. Cathode Materials

2. 1. Layered Cathode Materials

The layered structure compounds has the chemical formula of $LiMO_2$ (M=transition metal elements). The layered structure has cubic closed packing oxygen framework and MO_6 make the layer along X and Y direction. The lithium ions are occupied into octahedral sites and transition metal ion are also located into octahedral sites. The ideal $LiMO_2$ crystal belongs to α-$NaFeO_2$ structure and $R\bar{3}m$ space group with ABCABC type stacking like O-Li-O-TM-O-Li-O. The lithium ions in lithium layers show 2-dimensional diffusion (Figure 2.1).

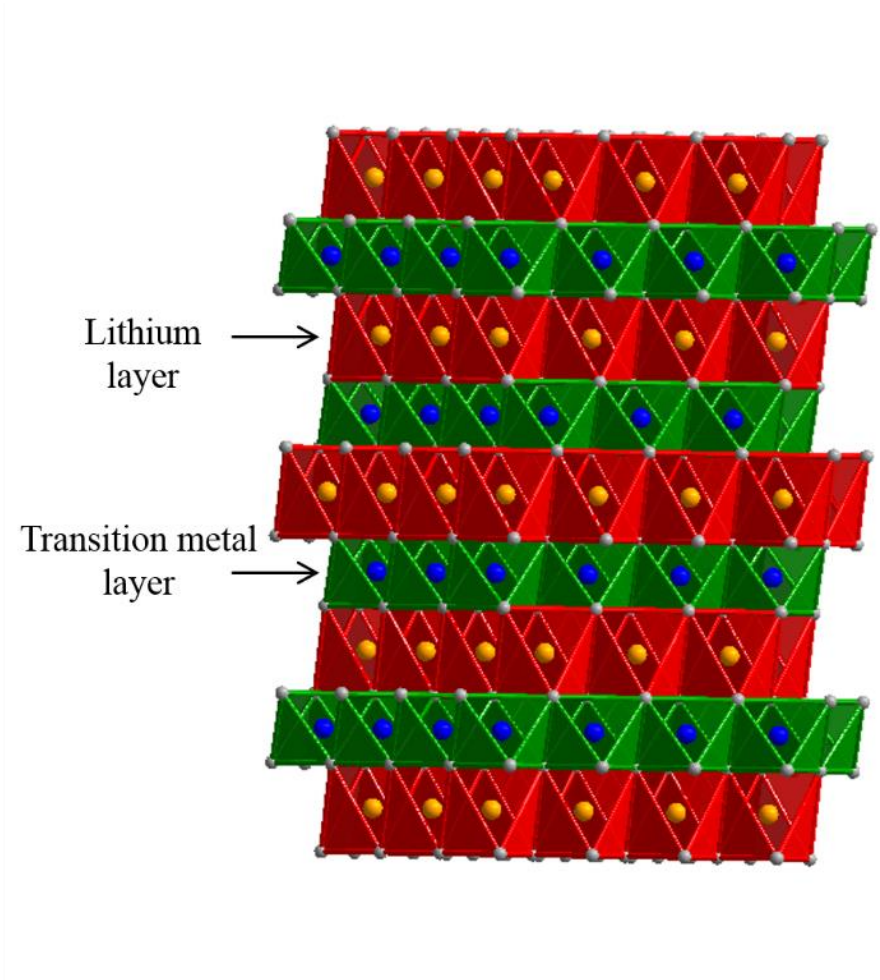

Figure 2.1. Crystal structure of layered cathode materials ($LiMO_2$)

2. 1. 1 $LiCoO_2$

$LiCoO_2$ is widely used cathode material which was the firstly commercialized by SONY for LIBs in 1991. This material was proposed by John B. Goodenough and still used in batteries. It is easy to synthesize $LiCoO_2$ at > 800 ºC. Also this material shows relatively high operating voltage of 3.9V and very stable cycling performance. However, if $LiCoO_2$ is highly delithiated state, the structure transition and oxygen lease occur causing fast capacity fading and safety issues. Figure 2.2 shows the evolution of the lattice constants *a* and *c* as a function of *x* in Li_xCoO_2 [1], and the phase diagram for Li_xCoO_2 *In-situ* X-ray diffraction indicates a sequence of three distinct phase transitions when x is changed from 1 to 0.4. Two of the transitions are situated slightly above and below $x=0.5$, and are caused by an order-disorder transition of the lithium ions. The order-disorder (monoclinic-hexagonal phase) transition has been studied as a function of temperature, allowing the determination of an order-disorder diagram. The other phase transition is shown to be first order (hexagonal Ⅰ + Ⅱ) involving a significant expansion of the lattice constant *c* of the hexagonal unit cell.[1-2] Therefore, it can deliver only 150 mAh g^{-1} in spite of its high theoretical capacity of 274 mAh g^{-1}. To overcome these barriers, the surface coating by using nano-sized surface layer such as metal oxides, fluorides and phosphates have been investigated.[3] The surface coating has effect on the thermal stability as well as cycling performance.[3a, 3c] (Figure 2.3 and Figure 2.4)

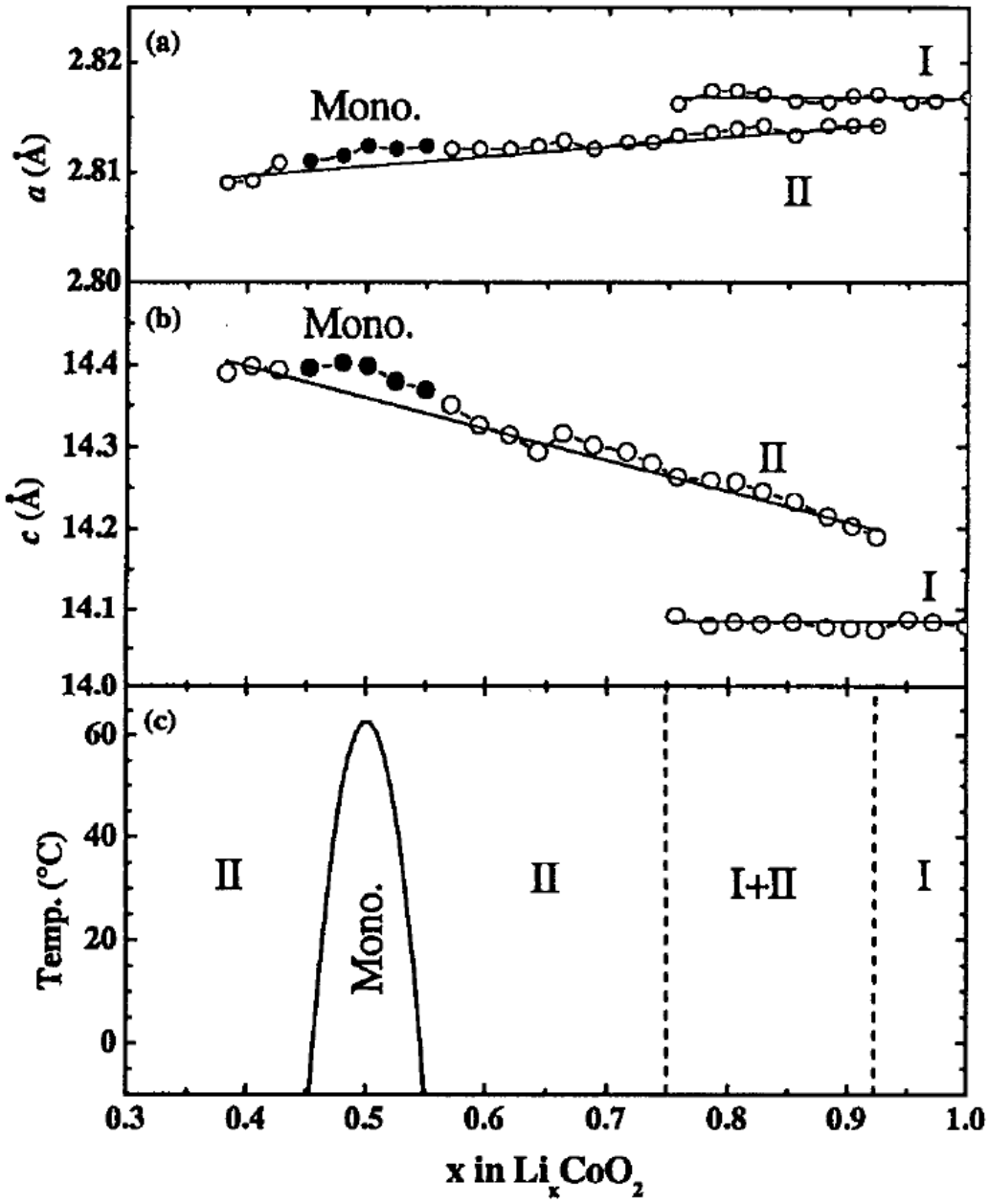

Figure 2.2. Lattice constants a (a) and c (b) as a function of the lithium concentration x in Li_xCoO_2. (c) Phase diagram for $LixCoO_2$.[1]

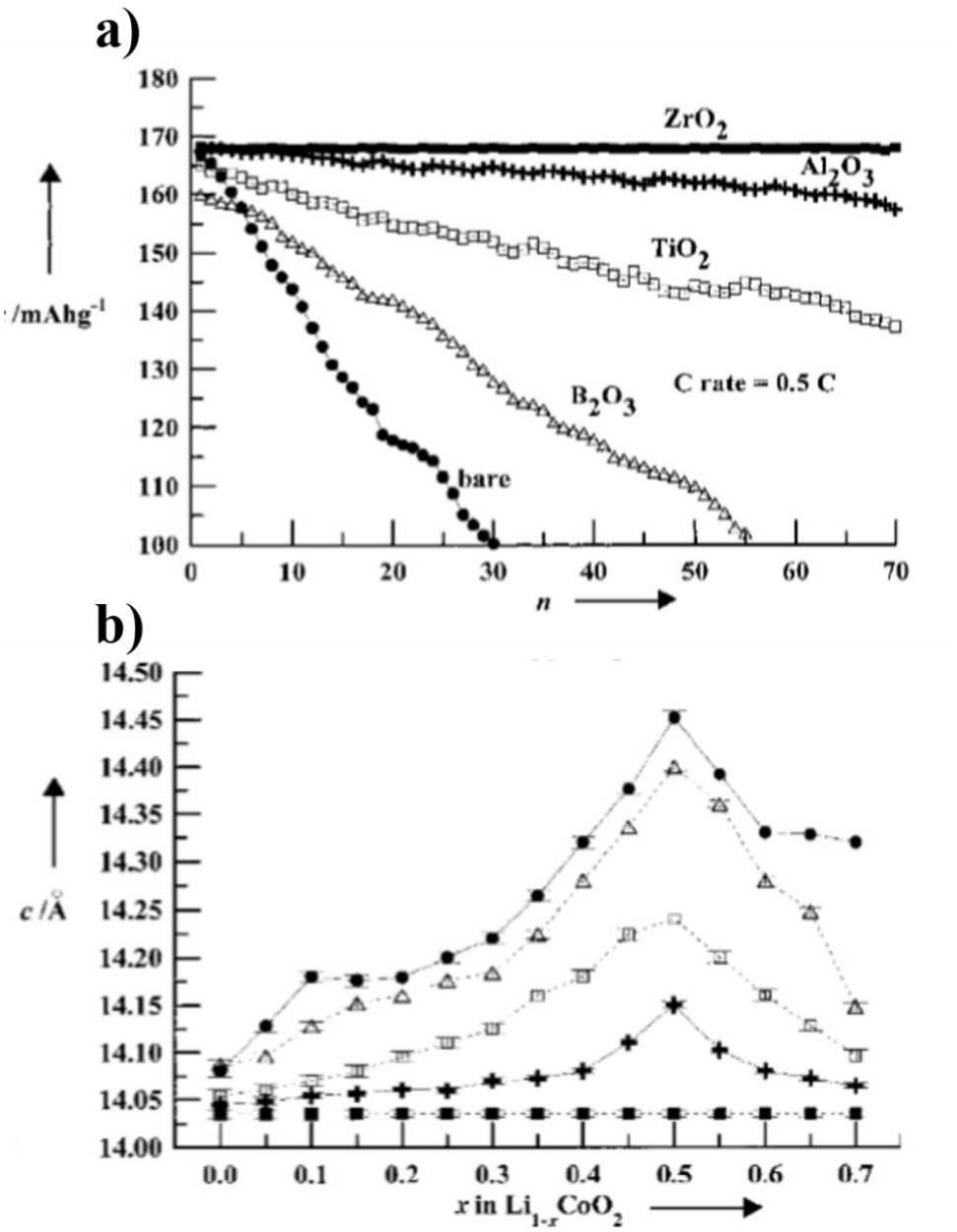

Figure 2.3. a) The cycling performance of various coating materials coated $LiCoO_2$ and bare $LiCoO_2$. b) Lattice constants c in ZrO_2 (■), Al_2O_3 (+), TiO_2 (□), B_2O_3 (△) coated, and bare $LiCoO_2$ (●) as a function of x in $Li_{1-x}CoO_2$ during the first charge.[3a]

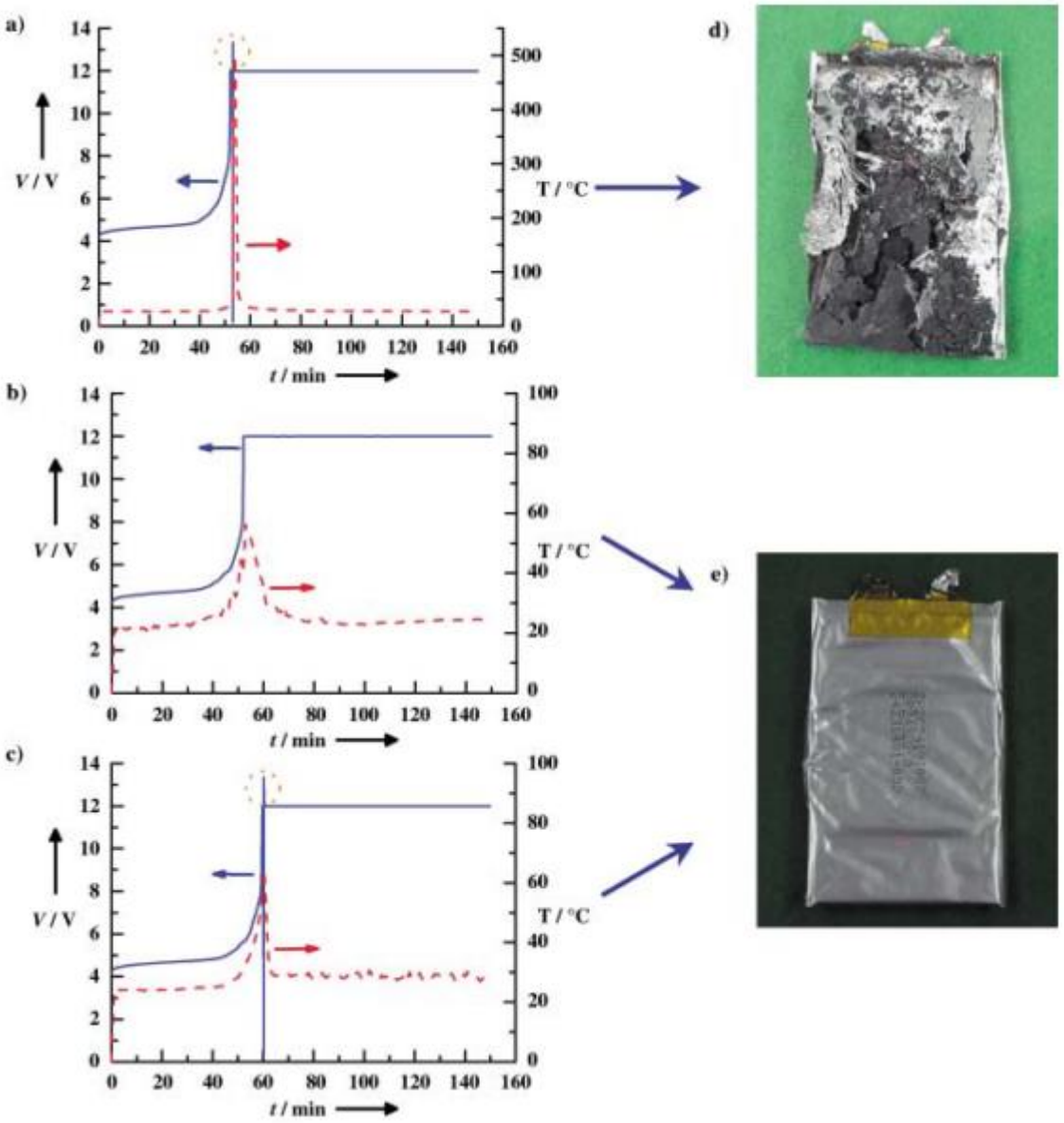

Figure 2.4. Voltage and temperature profiles of cell with a) bare $LiCoO_2$ and b,c) $AlPO_4$ coated LiCoO2 as a function of time. The pictures of cell with d) a bare $LiCoO_2$ and e) $AlPO_4$ coated $LiCoO_2$ after the 12V overcharge test.[3c]

2. 1. 2 $LiNiO_2$

The $LiNiO_2$ was first developed by Dyer group and considered as promising candidate for cathode material as alternatives to $LiCoO_2$.[4] The $LiNiO_2$ has a higher gravimetric capacity of >200 mAh g^{-1} and lower cost than $LiCoO_2$. However, it is very difficult to synthesize stoichiometric $LiNiO_2$. The Ni ions prefer Ni^{2+} instead of Ni^{3+} and the ionic radius of Ni^{2+} (r_{Ni+} =0.69Å) is similar to Li^+ (r_{Li+} =0.76Å). Therefore, Ni^{2+} is easily occupied into Li sites which leads to the formation of electrochemically inactive cation-disorder layer. This undesired structure hinder lithium ion diffusion causing poor electrochemical performances. Unlike $LiCoO_2$, the $LiNiO_2$ exhibits several phase transitions during electrochemical charge and discharge. There are four reaction regions of Li_xNiO_2 according to lithium stoichiometric x in terms of the change of lattice parameters.[5] (Figure 2.5) The final phase transition (x=0.25) is irreversible reaction which causes distortion of the crystal lattice structure. In addition, the delithiated state of $LiNiO_2$ is very unstable leading to accelerated structural instability. This side reaction generally accompanies with partly structure transformation to spinel and NiO-type rock salt phases causing fast capacity decay. Also the oxygen release occurs if the $LiNiO_2$ electrode is highly charged which resulting in thermal instability.

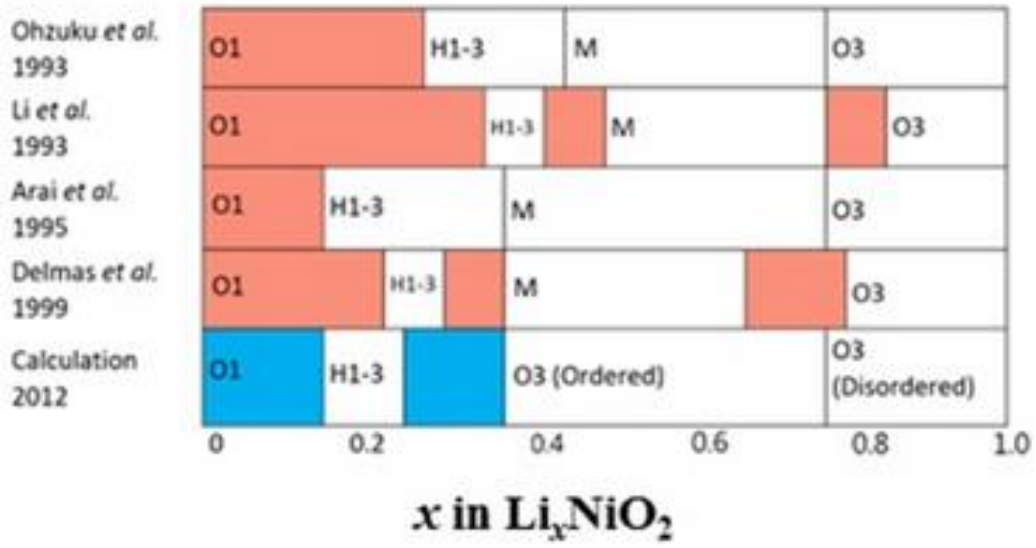

Figure 2.5. Phase diagram of the $LiNiO_2$-NiO_2 pseude-binary system from experimental data and calculation.[5b]

2. 1. 3 $LiNi_{1-x-y}Co_xMn_yO_2$

Generally, the $LiCoO_2$ forms a solid solution with $LiNiO_2$, but it doesn't form a solid solution with $LiMnO_2$. Also $LiNiO_2$ can be mixed with $LiMnO_2$ to form $LiNi_{1-x}Mn_xO_2$.[6] However, the maximum value of X is 0.5 (Figure 2.6). Also it is well known that the substitution of Co is an increased ordering of Ni in the structure and that of Mn provide the stability of structure.[7] Layered binary or ternary $Li[Ni_{1-x-y}Co_xMn_y]O_2$ has been considered to be a promising cathode materials because the thermal stability, capacity and cycling performance can be controlled by changing composition. Among many compositions, $LiNi_{0.5}Mn_{0.5}O_2$ and $LiNi_{1/3}Co_{1/3}Mn_{1/3}O_2$ are the representative materials. The oxidation states of Ni, Co and Mn are divalence, trivalence and tetravalence, respectively. In these materials, Mn4+ is inactive species resulting in contributing to the stability of the overall layered structure. The initial capacities of both material are similar to that of $LiCoO_2$. Also these materials show excellent cycleability due to no phase transformation in the domain of $0<x<80$ ($Li_{1-x}MO_2$), high safety and low cost.

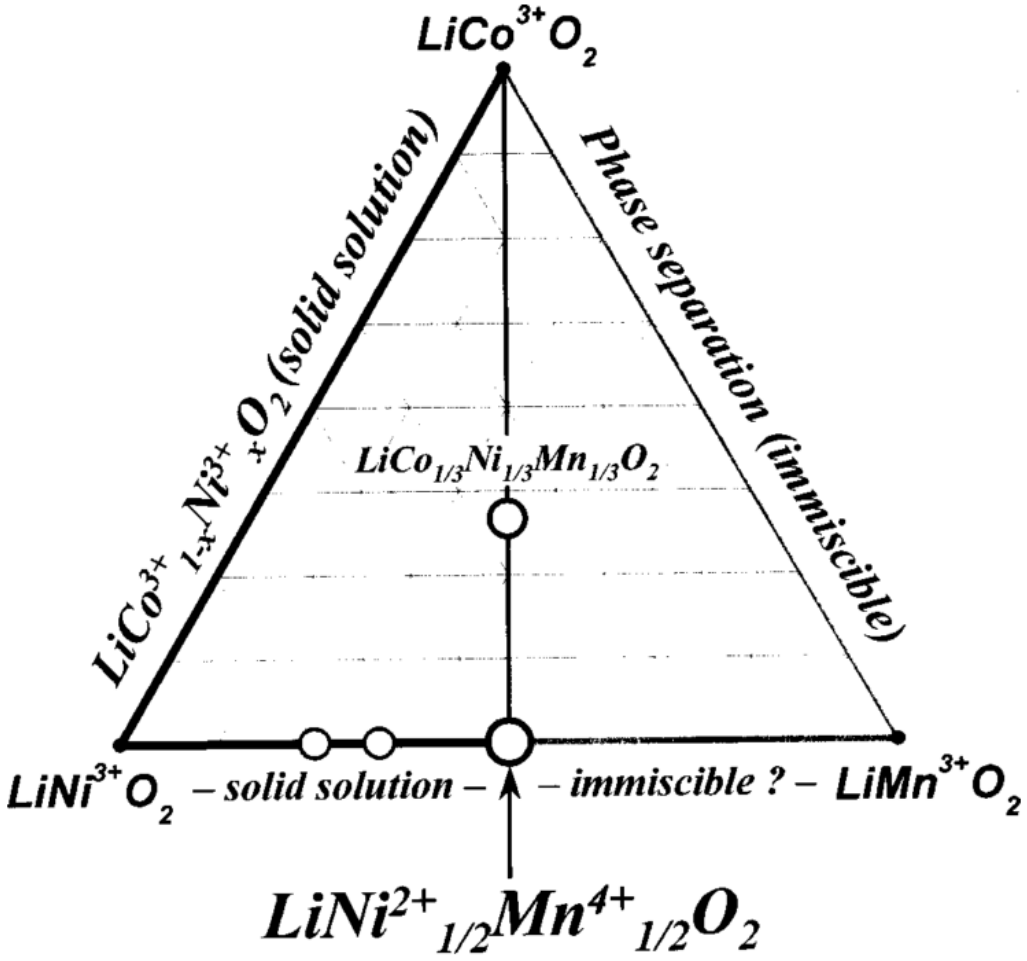

Figure 2.6. Phase triangle of $LiCoO_2$-$LiNiO_2$-$LiMnO_2$.[6]

2. 2. Li-rich Layered Cathode Materials: xLi2MnO3-(1-x)LiMO2 (M=Ni, Co, Fe, Cr, Mn and etc.)

Li-rich layered materials have attracted a lot of interest because of their higher specific capacity (> 240 mAh g^{-1} between 2.0 and 4.6V) and lower cost. Therefore it is considered as a promising candidate cathode materials of batteries for EVs. These materials can be represented in two-component notation, xLi_2MnO_3-(1-x)$LiMO_2$. During the first charge, electrochemical extraction of lithium ions from xLi_2MnO_3-(1-x)$LiMO_2$ lattices occurs in two steps.

$LiMO_2 \rightarrow MO_2 + Li^+ + e^-$, ~4.45V (1)

$Li_2MnO_3 \rightarrow MnO_2 + 2Li^+ + 0.5O_2 + 2e^-$, 4.45V~ (2)

The high cut-off nature can result in simultaneous reaction of lithium extraction and oxygen release at the particle surface. This irreversibility bring low coulombic efficiency at 1st cycle. [8] The released oxygen is reduced at the electrode surface in the discharge process, which results in the deposition on the electrode surface leading to the formation of byproducts such as Li_2CO_3.[9] (Figure 2.7) These byproducts cause reversible capacity declines. Also the highly oxidizing nature produces many side reactions between the surface of active materials and electrolyte. The undesired side reactions form thick solid electrolyte interface (SEI) layer, which hinders lithium diffusion and electron conduction. When cycling is carried out at elevated temperature, transition metal dissolution appears resulting in the loss of weight for active material. Consequently, the surface side reactions cause crucial capacity decay.

As the biggest issue of Li-rich layered cathode materials is the voltage decay during cycling. The energy density (Wh) is defined with multiplication of working voltage (V) and capacity (Ah). The decreasing working voltage results in energy decline. When lithium ion are extracted in the charge process, the transition metal ions are migrated from transition metal layer to lithium layer due to instability caused by vacancies of lithium layers. Consequently, electrochemically inactive rock-salt NiO and spinel-like phase are formed.[10]

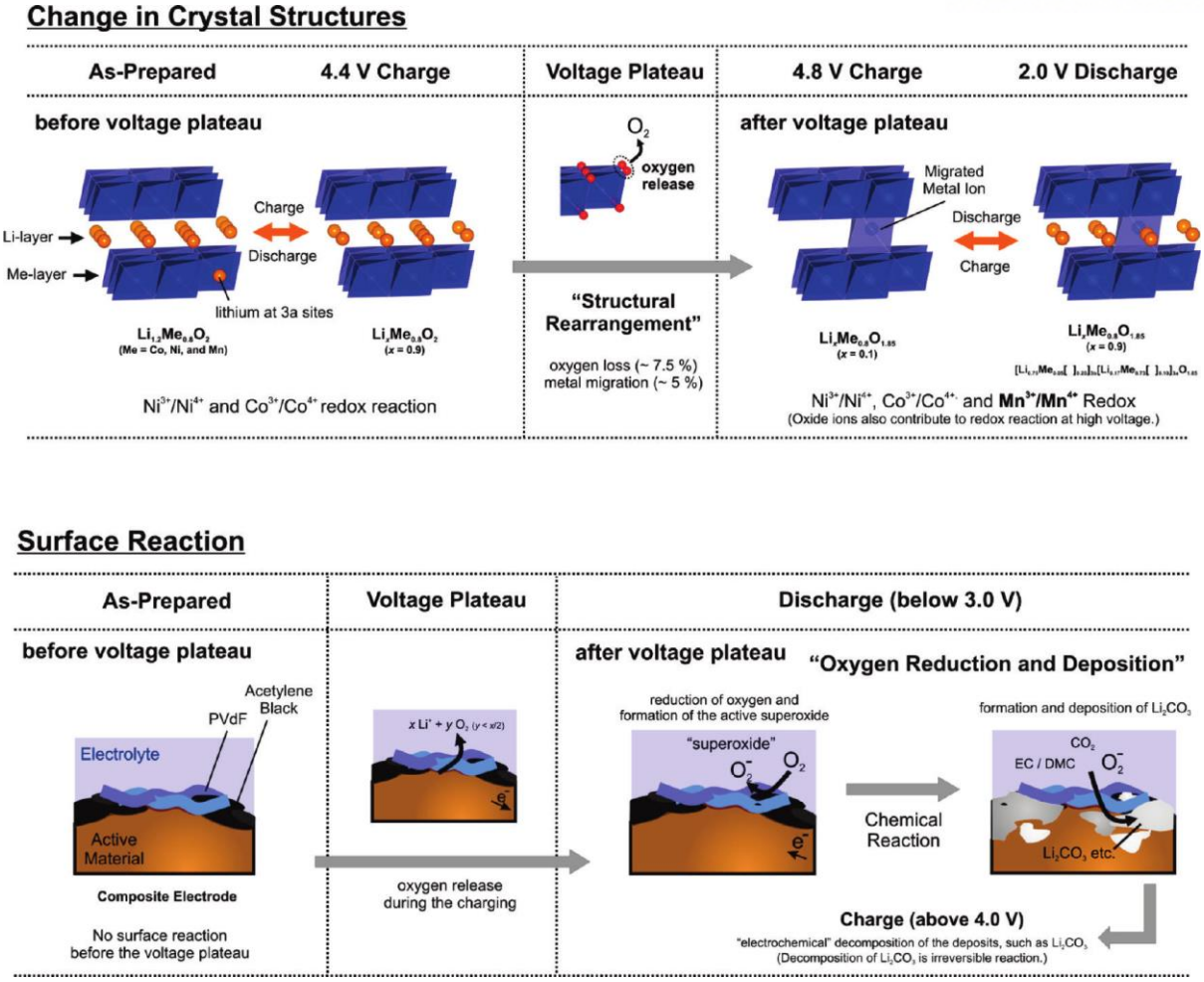

Figure 2.7. Schemes of the proposed reaction mechanisms in the $Li_xNi_{0.13}Co_{0.13}Mn_{0.54}O_{2-\delta}$ composite electrodes consisting of the active material, acetylene black, and PVdF.[9]

2. 3. Spinel Cathode Materials

The spinel cathode material has been considered as one of the most promising cathode materials to be used for EVs due to its advantages of low cost, safety and high power properties. The spinel cathode material has cubic spinel structure with space group of Fd-3m and oxygen atoms are stacked by cubic closed packing (CCP) (Figure 2.8).[11] The unit cell of spinel structure consists of eighth AB_2X_4 units that totally have 64 tetrahedral sites and 32 octahedral sites. Li ions are occupied into 1/8 of the tetrahedral sites (8a sites). The Mn ions are located into 1/2 of the octahedral sites, which forms a three-dimensional network of edge-sharing MnO6-octahedra (16d sites). The remained sites exist as a vacancies.

The lithium sites (8a) and vacant sites (16c) in M_2O_4 form diamond-like 3D lithium diffusion channel (Figure 2.9).[12] In charge and discharge process, lithium ions are diffused along 8a→16c→8a→16c→ three-dimensionally, which offers fast diffusion pathway leading to high power properties. Therefore, the spinel cathode materials are attractive for high power applications such as hybrid electric vehicles (HEVs) and power tools.

The spinel $LiMn_2O_4$ shows three distinctive steps in the shape of discharge curve, region I and II about 4V versus Li/Li^+ and region III about 3V versus Li/Li^+ (Figure 2.10).[13] The reaction related to region I and II is reaction at 4V below and region III is reaction at 3V below;

$Mn_2O_4 + Li^+ + e^- \rightarrow LiMn_2O_4$ (Reaction at 4V)

$LiMn_2O_4 + Li_+ e^- \rightarrow Li_2Mn_2O_4$ (Reaction at 3V)

The reason why the two-plateau voltage behavior is shown is ascribed to rearrangement of lithium ion in tetrahedral sites. In region II, the discharge voltage decreases continuously between 3.7 and 4.0V, which is consistent with reaction without changing crystal structure of cubic leading to small changes of lattice parameter. In the case of region III, during the lithium insertion reaction (Discharge) is accompanied with phase transition, which is believed that lithium insertion into octahedral 16c sites occurs at around 3V by two phase reaction involving the cubic and tetragonal spinel. The additional lithium insertion causes a severe structural changes due to Jahn-teller distortion (Figure 2.11).[14] When $LiMn_2O_4$ is changed to $Li_2Mn_2O_4$ by lithium insertion reaction, t_{2g} is separated to d_{xy}, d_{yz} and d_{xy}, and e_g is separated to d_x^2-$_y^2$ and d_z^2. Therefore, the octahedral MnO_6 lengthen along c-axis by 12% and shorten along a and b-axis by 3%. Finally the tetragonal phase transition is accompanied by a 16% increase in c/a ratio and 6.5% total volume expansion. These repetitive changes affect the contact with conductive agent leading to weaken electrical network for electrode. Thus, only 4V region is electrochemically available for battery cycling.

Mn dissolution is main problem of capacity fading at elevated temperatures (>50 ^{o}C) (Figure 2.12). [15] Mn^{3+} in spinel $LiMn_2O_4$ is separated by disproportionate reaction.

$2\ Mn^{3+}\ (Solid) \rightarrow Mn^{4+}\ (Solid) + Mn^{2+}\ (Soluble)$

The MnO (Mn^{2+}) in $LiMn_2O_4$ is dissolved by hydrogen fluoride (HF). It is known that small amount of water (H_2O) produces HF by reacting $LiPF_6$.

$LIPF_6 + H_2O \rightarrow LiF + PO_3 + 2HF$

Also, impurity material such as insulator MnF_2 is formed by HF.

$2LiMn_2O_4 + 4H^+ + 4F^- \rightarrow 3MnO_2 + MnF_2 + 2LiF + 2H_2O$

The dissolved Mn^{2+} is migrated to anode side and reduced on the graphite surface leading severe capacity degradation of full cell.

As a factor of capacity fading for spinel $LiMn_2O_4$, oxygen deficiency was proposed.[16] Yoshio and Xia proposed the relation of cycle performance and oxygen deficiency. [17] Also Kanno reported that some interstitial oxygen atom is occupied into vacant 8b site instead of original site of 32e, which results in impeding lithium ion diffusion.[18] The presence of oxygen deficiency can be easily confirmed with extra plateau at 3.2V and 4.5V, represented by z value in $LiMn_2O_{4-z}$. The z value is related to the capacity at 3.2V and 4.5V. The amount of value z can be confirmed by calculating the capacity of 12z mol Mn as following equation;

Assume (a) the molar ratio of $Mn^{3+}/Mn^{4+}=1$

(b) the capacity of 1mol Mn^{3+} in $LiMn_2O_4$ = 148 mAh g^{-1}

C3.2V (capacity at 3.2V) = 148 x 12z x 0.5 x.0.5

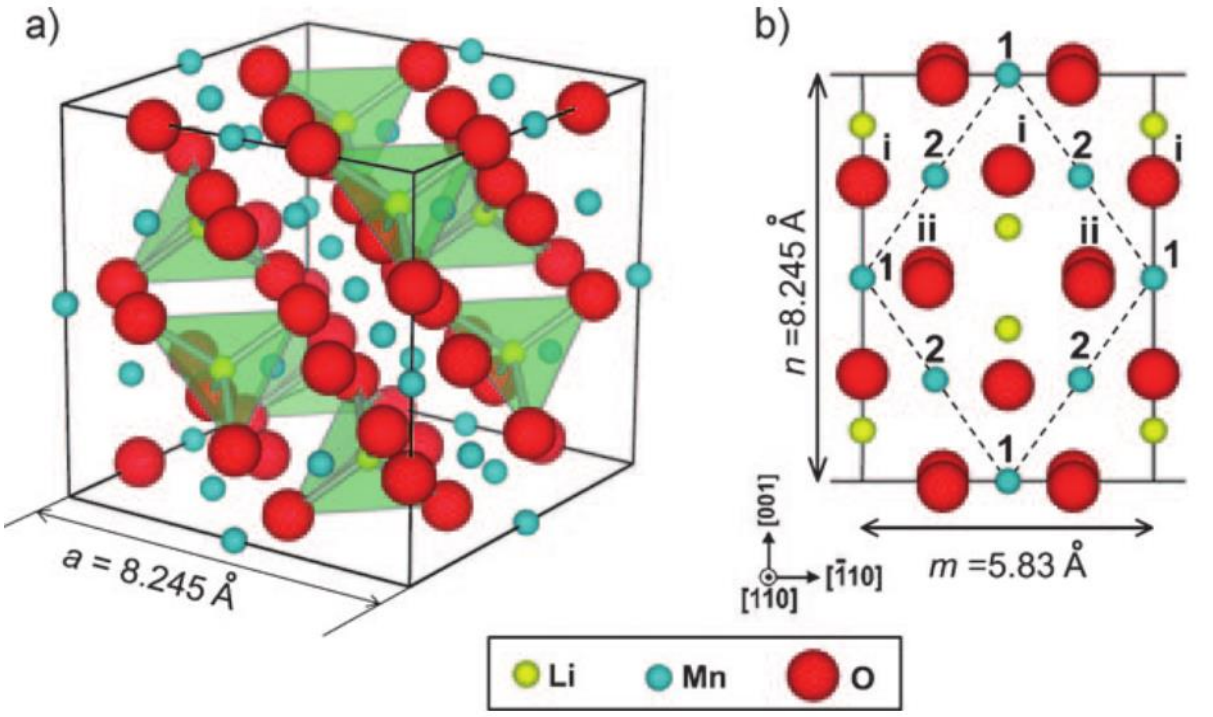

Figure 2.8. a) The unit cell structure of spinel $LiMn_2O_4$. B) Projection along the [110] zone axis showing separate Li, O, and Mn columns. Mn-1 columns has twice higher atomic density than Mn-2 columns. [11]

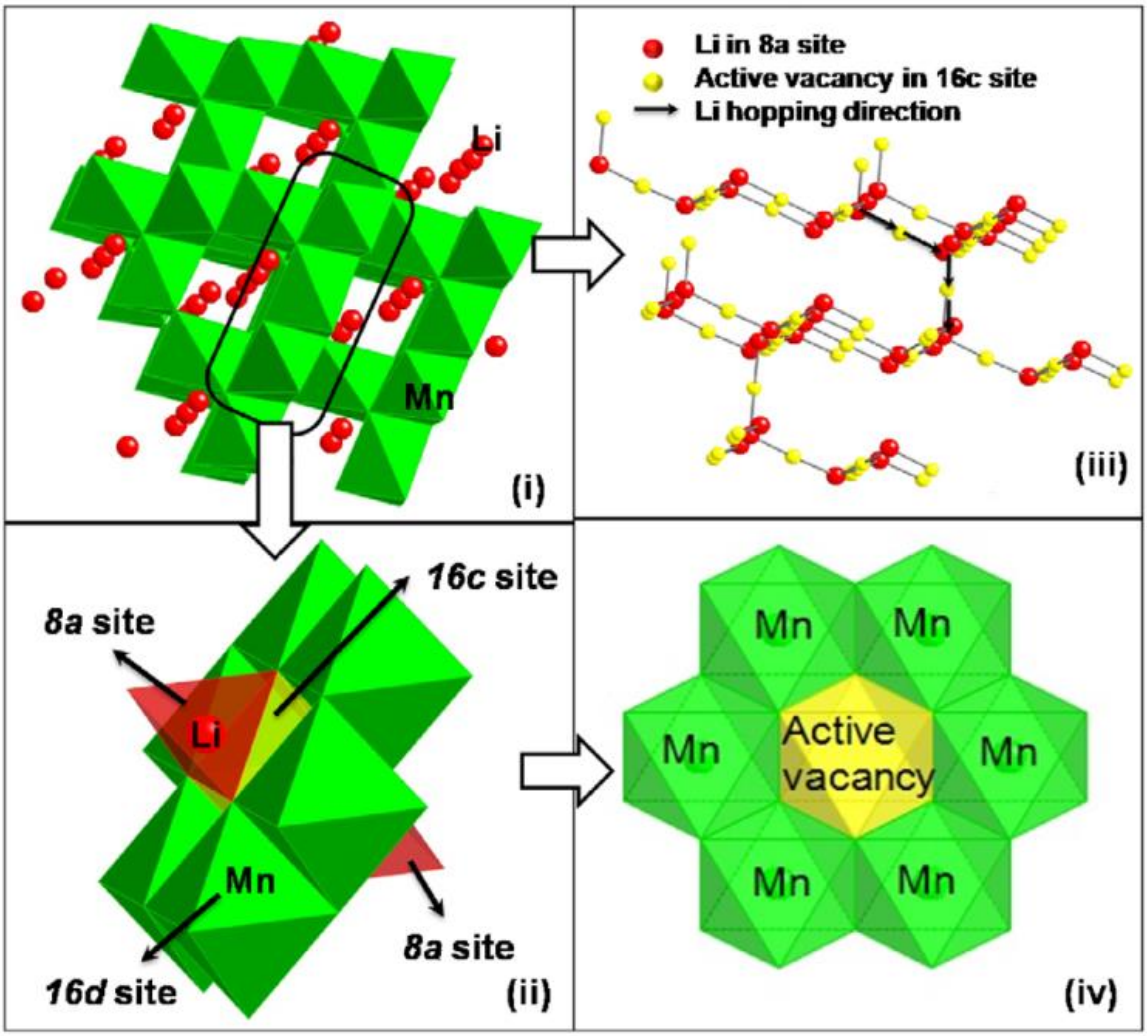

Figure 2.9. Three-dimensional lithium diffusion pathway in spinel cathode material.[12]

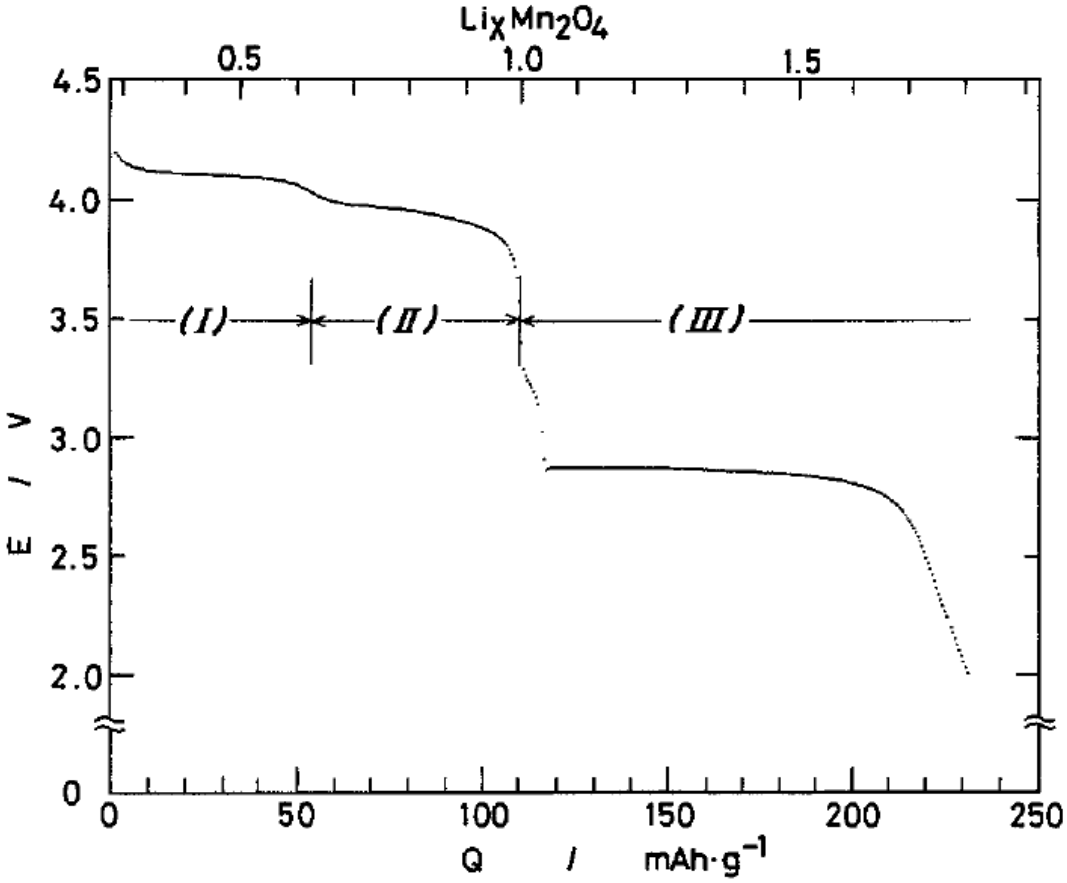

Figure 2.10. Typical voltage profile of spinel $LiMn_2O_4$. (I) phase transition from cubic λ-Mn_2O_4 to $Li_{0.5}Mn_2O_4$. (II) from $Li_{0.5}Mn_2O_4$ to $LiMn_2O_4$, (III) from cubic $LiMn_2O_4$ to tetragonal $Li_2Mn_2O_4$.[13]

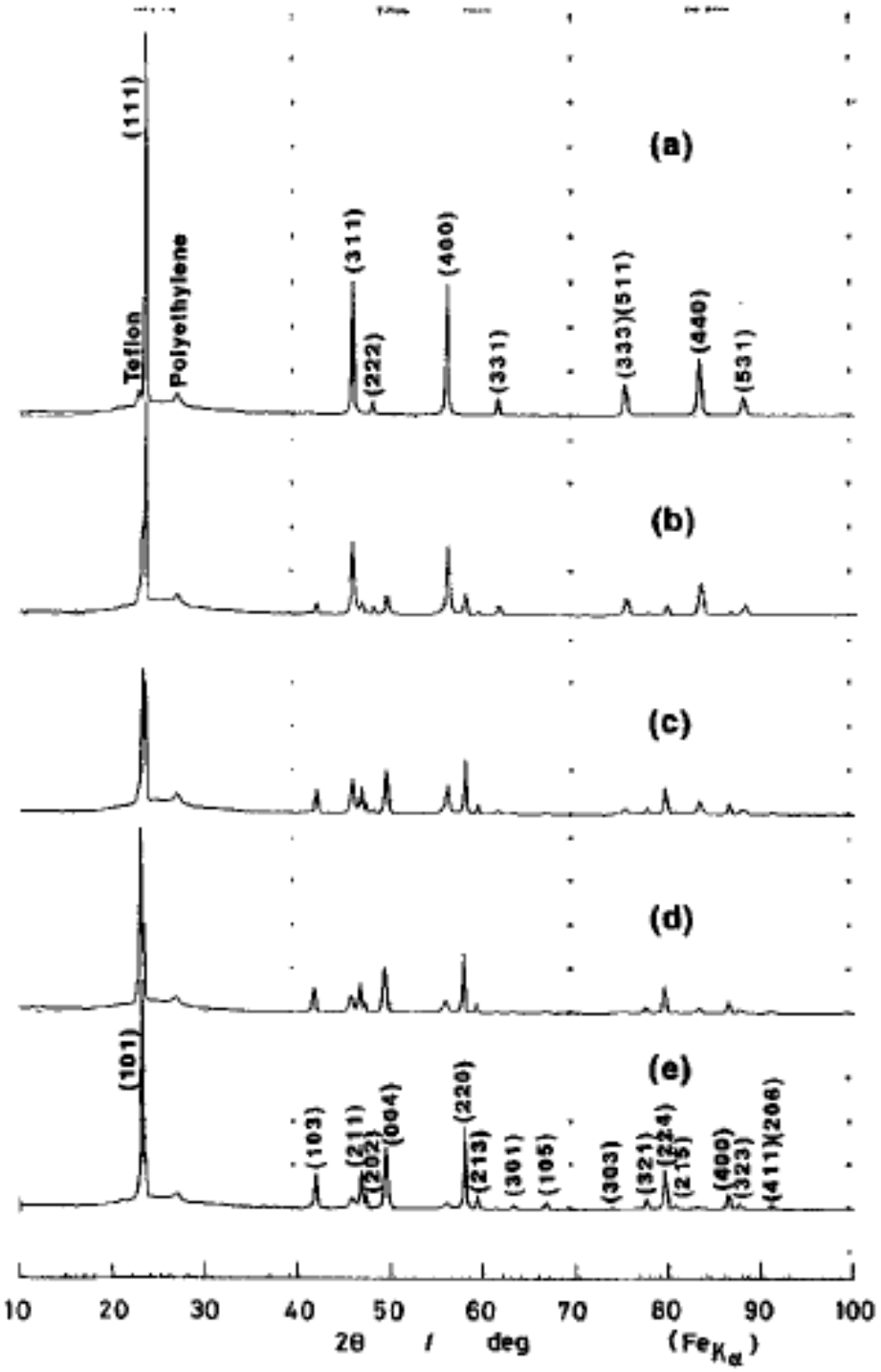

Figure 2.11. X-ray diffraction pattern changes during the reduction of $Li_xMn_2O_4$ in the region III in Figure 2.10.[13]

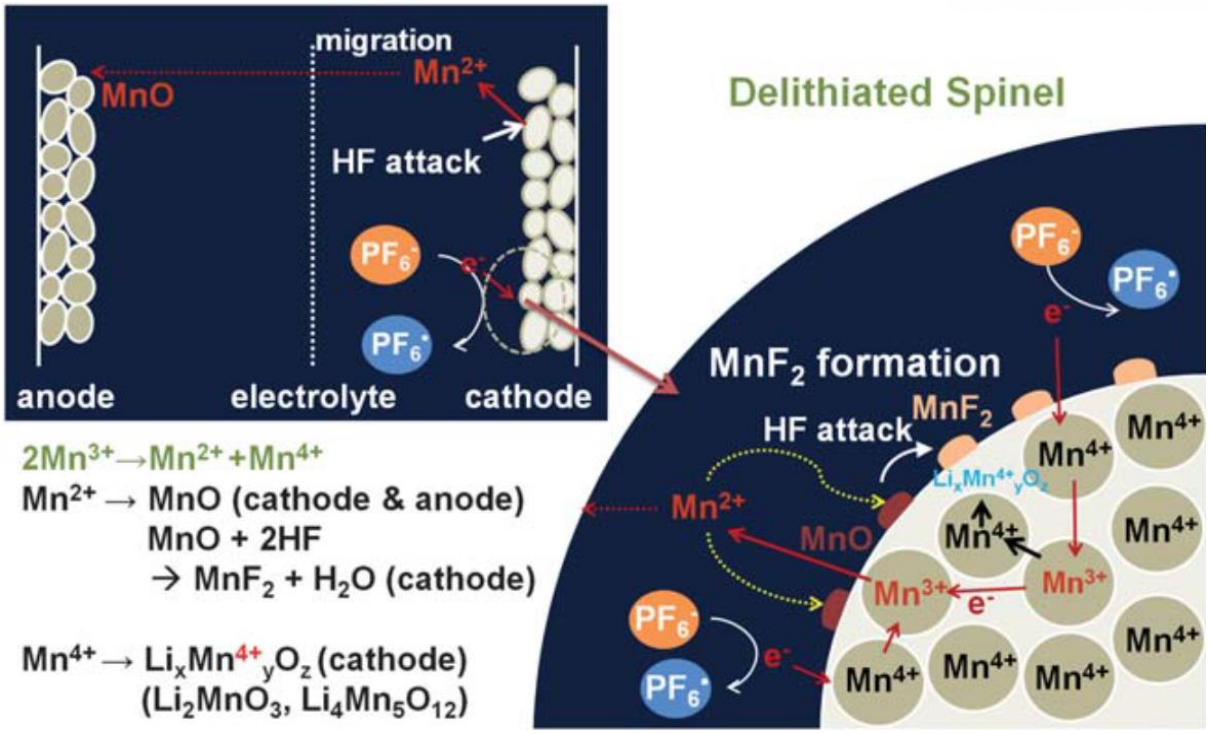

Figure 2.12 Mechanism of Mn^{3+} dissolution.[15]

3. Experiment

3. 1. Simultaneous Surface Modification Method for $0.4Li_2MnO_3$-$0.6LiNi_{1/3}Co_{1/3}Mn_{1/3}O_2$ Cathode Material for Lithium Ion Batteries: Acid treatment and $LiCoPO_4$ coating

3. 1. 1. Introduction

Recently, Lithium ion batteries (LIBs) are getting attention as the most promising energy storage system for electric vehicles (EVs) as well as small portable devices due to many advantages such as low self-discharge rate, high energy density and long cycle life. The EV equipped small-sized LIBs and motors which is called hybrid electric vehicles (HEVs) achieved better fuel economy by using mainly spinel $LiMn_{2-x}M_xO_4$ (M = Li, Al, Mg, Co, etc.) as a cathode material to fulfill HEV's demanding power and durability requirements. However, it can run very short driving range in EV mode due to small-sized LIBs composed of mainly spinel cathode materials with low energy density.[19]

As quickly increased the needs for higher-mileage EVs, the researchers have extensively and intensively investigated many possible cathode materials with higher energy density than spinel cathode materials such as Li-rich layered materials Li_2MnO_3-$LiMO_2$ (M=Ni, Co, Mn, Cr, Fe, etc.) [20] and Ni-rich layered materials $LiNi_{1-x}M_xO_2$ (1-x > 0.6; M= Co, Mn, Al, etc.)[21]. Among them, the Li-rich layered materials have attracted a lot of interest because of their higher specific capacity (> 240 mAh g^{-1} between 2.0 and 4.6V) and lower cost. However, it also has many drawbacks such as low coulombic efficiency at 1st cycle, voltage decay with cycling, intrinsically poor rate capability, and irreversible side reactions with electrolyte due to high cut-off voltage, especially at elevated temperatures (> 60 °C).[22] In order to overcome such problems, many solutions have been proposed and studied. Surface coating is frequently investigated for the improvement of electrochemical performance by using the inert ceramics such as metal oxides, fluorides and phosphates (Figure 3.1.1a).[8, 20a, 23] These coating materials act as a protective layer against the present acidic electrolyte resulting in the diminishment of side reactions on the surface. Another approach to overcome the drawbacks is an acid treatment for the chemical activation, which is intended to improve the initial efficiency.[24] In this process, lithium ions are extracted

from the lattice, which results from H^+/Li^+ exchange reaction. It is believed that the extracted lithium ions can be converted to lithium impurities such as Li_2CO_3 and LiOH, which causes the gas evolution at 1st charge, unless fully removed (Figure 3.1.1b and 3.1.2). Recently, our group proposed RGO-coated Li-rich material; GO was reduced by hydrazine treatment, and material with submicron-sized flake-shaped primary particles.[10b, 25] Both studies showed significant improvements of performances. However, there is no investigation at elevated temperature, even though the cell evaluations at the elevated temperature (> 60 ºC) are very critical factor because lithium ion batteries are usually packed in a closed space causing heat accumulation. Also the safety issues should have been handled. Other groups reported many investigations of surface coating and acid treatment on the Li-rich cathode materials to enhance their electrochemical and thermal weakness.[8, 20a, 23-24] For instance, Y. Su. et al. reported spinel membrane-encapsulated Li-rich material.[26] The cells were performed between 2.0 and 4.8 V. It showed the improved electrochemical performances such as rate capability, coulombic efficiency, cycleability and so on, but no investigation of cycling performance at elevated temperature (> 60 ºC) mentioned. Also PNNL group found a possible origin of the voltage decay was related to uneven distribution of Ni elements in the cathode and a way of minimizing the voltage decay at room temperature via hydrothermal method, of which one led to uniform distribution of Ni elements. Set aside the inherent voltage decay during cycle originated from spinel-like phase transition, other critical considering test criteria, such as, gas evolution from the Li impurities from the cathode surface due to acid treatment, rate capability, 1st coulombic efficiency, and cycling performance at elevated temperature, and thermal instability have not been tried to solve at the same time. Therefore, it is necessary that the efficient and effective methods, which can carry out the surface coating and acid treatment for chemical activation simultaneously, should be developed to improve such drawbacks. Also the candidate of coating material should react with residual impurities to the eliminate side reactions.[27]

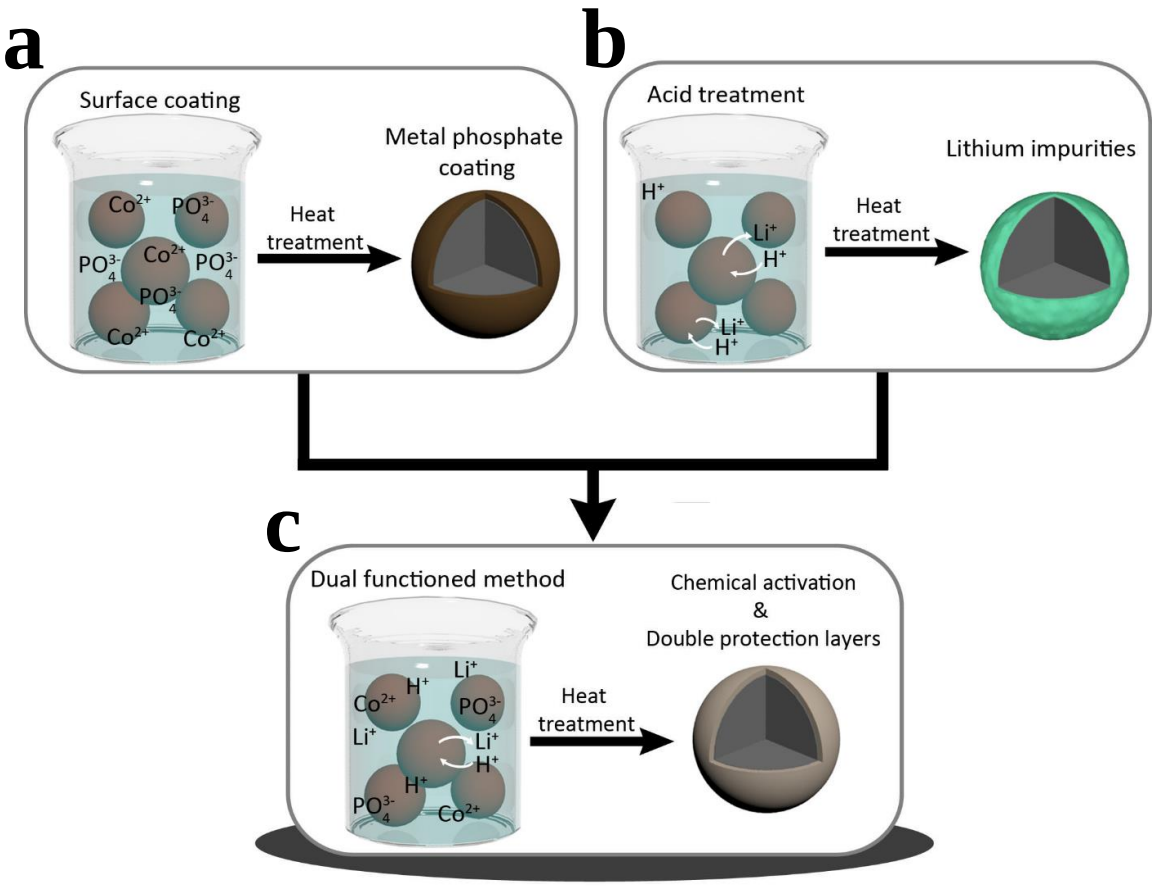

Figure 3.1.1. Schematic view of fabrication processes and their final results of (a) surface coating, (b) acid treatment, and (c) dual functioned method.

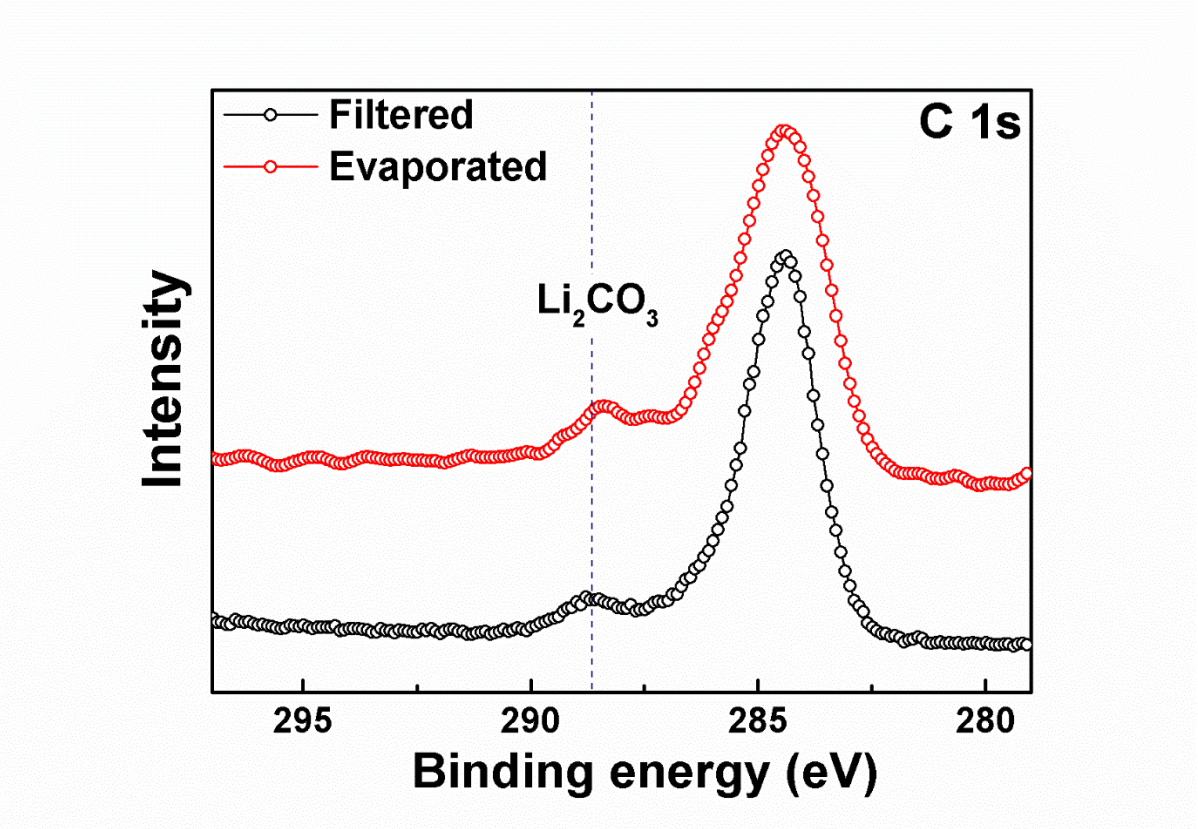

Figure 3.1.2. The 1 g of bare power was immerged into 20 ml of 0.25M acetic acid solution, and then the mixture was thoroughly stirred for 1h. The black line is the C 1s XPS spectra of the powder filtered after mixing and the red one is the result of the sample evaporated at 110 ^{o}C until water removal. The result powders were heated at 600 ^{o}C for 3h. All spectra were calibrated to a peak arising from carbon at 284.2 eV.

Herein, we reported the $LiCoPO_4$ coated $0.4Li_2MnO_3$-$0.6LiNi_{1/3}Co_{1/3}Mn_{1/3}O_2$ synthesized by the efficient dual-functioned coating method (Figure 3.1.1c). The lithium ions in coating material $LiCoPO_4$ originated from the host material. These were extracted when stirred in acidic solution with cobalt and phosphate ions. During heating process, these ions were consumed to form $LiCoPO_4$ on the surface of host particles. Also, the structure, where lithium ions were extracted, was recrystallized to form the spinel surface layers. The double protection layers on the surface, Ni and Co doped spinel and $LiCoPO_4$, effectively suppressed the side reactions leading to the improved electrochemical performances relative to the bare $0.4Li_2MnO_3$-$0.6LiNi_{1/3}Co_{1/3}Mn_{1/3}O_2$. More importantly, the coated cathode demonstrated far less heat evolution at 4.6V, compared to the bare counterpart.

3.1.2 Experimental Section

Synthetic method. To begin, $Ni_{0.2}Co_{0.2}Mn_{0.6}(OH)_2$ powder was synthesized via co-precipitation method. Stoichiometric amounts of $NiSO_4 \cdot 6H_2O$, $CoSO_4 \cdot 6H_2O$ and $MnSO_4 \cdot 5H_2O$ were used as the starting materials. An aqueous solution (Ni:Co:Mn=0.2:0.2:0.6 in molar ratio) at a concentration of 2.0 mol L^{-1} was pumped into a continuously stirred tank reactor (CSTR, 4L) under nitrogen atmosphere. The pH was adjusted to 10.5 with NaOH solution of 4.0 mol L^{-1} and desired amount of NH_4OH solution as a chelating agent was also seperatly fed into the reactor. The obtained powder were filtered and washed many times with distilled water, and then dried at 110 ^oC for 12 h. The dried powders was thoroughly mixed with LiOH with a molar ratio of 1:1.44 and calcined at 900 ^oC for 10 h to obtain $0.4Li_2MnO_3$-$0.6LiNi_{1/3}Co_{1/3}Mn_{1/3}O_2$ (bare). To prepare the coated sample, the bare powder was immersed into the acidic solution of $Co(NO_3)_2 \cdot 6H_2O$ and H_3PO_4 (85 wt% in H_2O) for the chemical activation. The mixture was stirred vigorously at 150 ^oC until water removal, and then the result powder was heated at 600 ^oC for 3 h.

Characterizations. The crystal structure was confirmed by powder X-ray diffractometer (XRD, D/Max-2200 V, Rigaku) using Cu Ka radiation. The morphologies of prepared samples were examined using scanning electron microscopy (SEM, S-4800, HITACHI). The samples for transmission electron mictoscopy analysis were prepared by focused ion beam (FIB, Quanta 3D FEG, FEI). To analyze a struture with an atomic scale, the high resolution-transmission electron mictoscopy (HR-TEM, JEM-2100F, JEOL) operation at 200kV was used. For DSC analysis, the CR2032 coin-type cells were fully charged at 4.6 V and opened carefully in a dry-room. After the current collectors were washed with dimethyl carbonate (DMC) and dried, the sample and 30 wt% electrolyte were sealed inside stainless steel high-pressure capsules to prevent leakage of the pressurized solvents. The DSC curves were measured from 50 ^oC to 350 °C at a scan rate of 5 °C min^{-1}.

Electrochemical characterization. The cathode electrodes were fabricated by blending the prepared powders (85 wt%), Super P carbon black (5 wt%), and polyvinylidene fluoride (10 wt%). Galvanostatic charge and discharge cycling was carried out using CR2032 coin-type cell, which consists of a cathode electrode and a lithium metal anode seperated by the porous polypropylene film, which were assembled in an argon-filled glove box. 1.15 M $LiPF_6$ in mixture of ethylene carbonate (EC) and ethyl methyl carbonate (EMC) in 3:7 volume ratio (PANAX ETEC Co. Ltd., Korea). All electrochemical tests were performed on WBCS-3000 (WonATech Co.). The galvanostatic charge-discharge tests were conducted in a voltage range of 4.6 to 2.0 V vs. Li/Li^+. The active material loading was 4 mg cm^{-2}. Electrochemical impedance spectroscopy (EIS) was performed from 0.02 to 250 kHZ frequency range using electrochemical interface system (IVIUM) on coin-type half cells at 4.6 V.

3.1.3 Results and Discussion

In order to confirm the crystal structure of the prepared samples, the X-ray powder diffraction (XRD) measurement was carried out and its results are shown in Figure 3.1.3. The XRD patterns of the bare $0.4Li_2MnO_3$-$0.6LiNi_{1/3}Co_{1/3}Mn_{1/3}O_2$ (denoted as bare) indicated the typical Li_2MnO_3-$LiMO_2$ composite phases.[20a, 24a] Weak super-lattice reflection peaks appeared between 20° and 25°. The 2 wt% $LiCoPO_4$ coated sample (denoted as 2LCP) has the similar peaks with bare and almost indiscernible impurity peaks are founded. The peaks intensities of this impurity were raised when the coating amount increased to 5 wt% (denoted as 5LCP). The impurity is in good agreement with olivine $LiCoPO_4$ of space group *Pnma*. From these results, it is reasonable to infer that the lithium ions were extracted through H^+/Li^+ exchange reaction when stirred at acidic solution, and $LiCoPO_4$ was successfully formed with the extracted lithium ions and the introduced cobalt and phosphate ions during further heating process. The morphologies of the bare and 2LCP powders were confirmed by the scanning electron microscopy (SEM). As can be seen in Figure 3.1.4a and b, no significant change of morphology can be observed after coating. Also the evenly distributed phosphorous ions demonstrated that the $LiCoPO_4$ was well coated on the surface of the bare according to the energy dispersed X-ray (EDX) analysis (Figure 3.1.4c-f). The X-ray photoelectron spectroscopy (XPS) profile for C 1s showed no carbon peak of Li_2CO_3, which indicates that the extracted lithium ions were well consumed to form $LiCoPO_4$ on the surface (Figure 3.1.5).

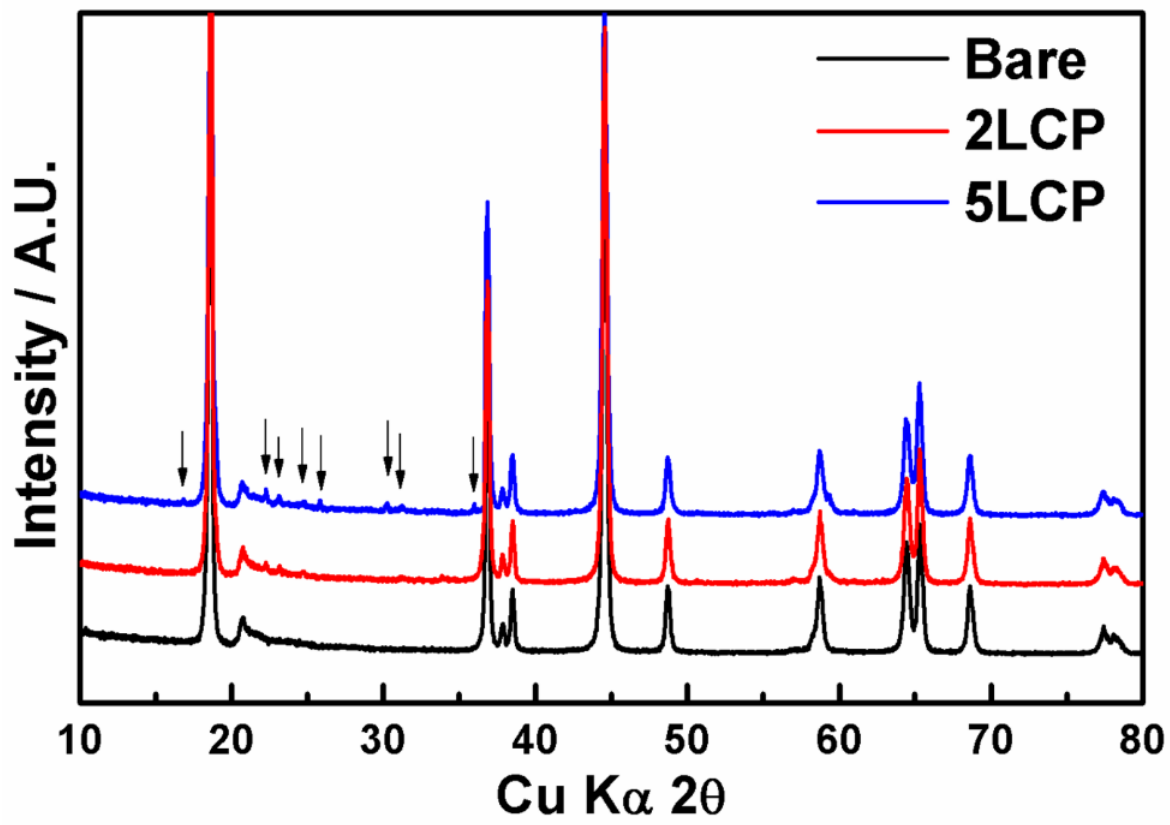

Figure 3.1.3. Power XRD patterns of bare and coated samples. The arrows (↓) indicate peaks of the $LiCoPO_4$ phase.

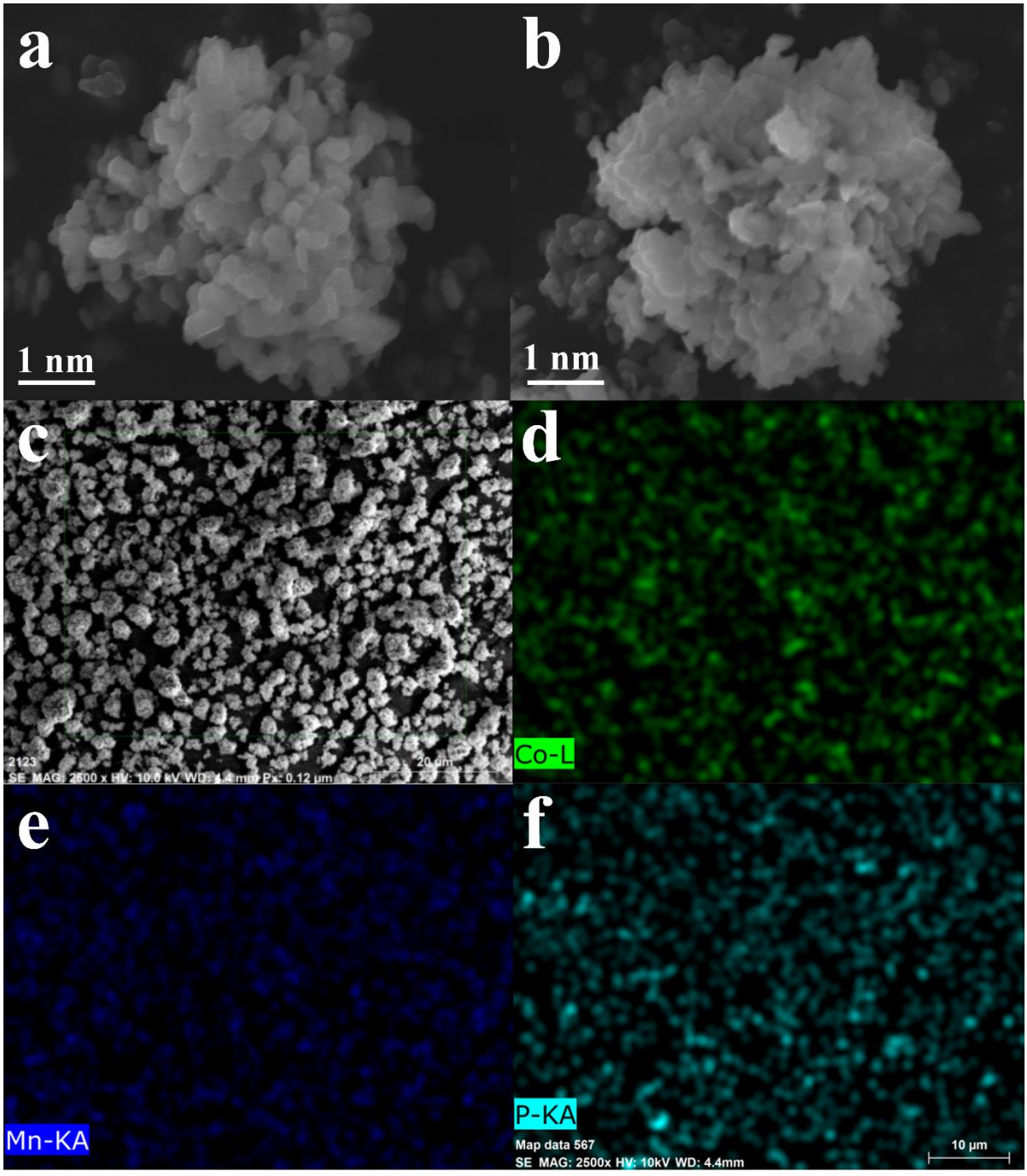

Figure 3.1.4. SEM images of (a) Bare, (b) 2LCP, (c) low magnified image of (b), Energy dispersed X-ray analysis of each element (d) Co, (e) Mn, and (f) P.

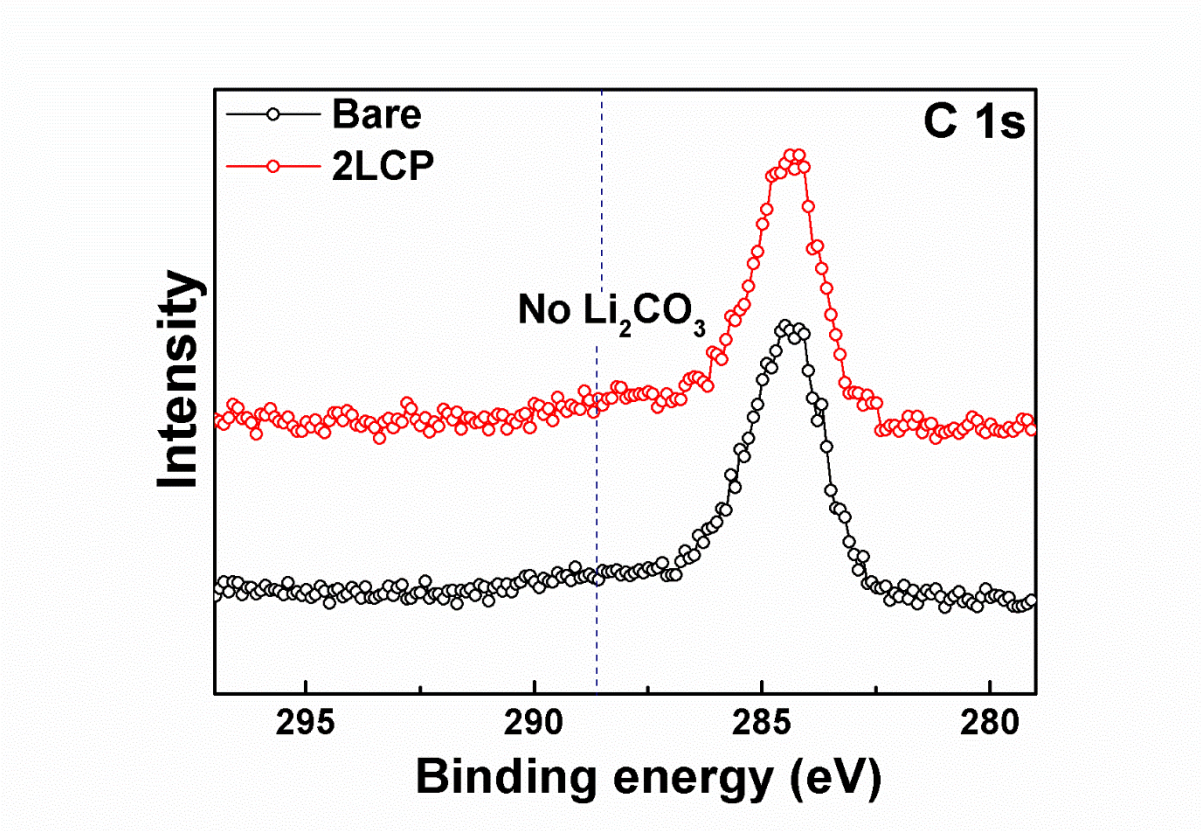

Figure 3.1.5. C 1s XPS spectra of bare and 2LCP powders.

To analyze the microstructures of samples with an atomic scale, the measurement of the scanning transmission electron microscopy (STEM) was carried out. Figure 3.1.6a and c show high-angle annular dark-field (HAADF) STEM images of the bare and 2LCP that are cross-sectioned, respectively. No coating layers are observed on the surface of the bare particle (Figure 3.1.6a). However, in case of the coated sample, the rough coating layers can be found on the host material, which looks like amorphous phase (Figure 3.1.6c). It is revealed that the layered structure (*R-3m*) are based on the cubic close packed (ccp) oxygen arrangement, while the olivine structure (*Pnma*) has the hexagonal close packing (hcp) array of the oxygen ions. Also the transition metal and lithium ions sites are dependent on the oxygen framework. Therefore, when the zone axis is focused on the host layered material, the olivine coating material looks like amorphous phase and seems to be unclear due to the different oxygen array. The atomic distribution of this coating layer was confirmed by the EDX analysis (Figure 3.1.6e-h). As can be seen, the cobalt and phosphorus atoms were evenly distributed on the host material. From EDX results and XRD patterns, it is concluded that olivine $LiCoPO_4$ coating layer was successfully formed on the surface. The coating method of this study accompanied with the acid treatment (chemical activation) leading to structural changes. Figure 3.1.6b and d indicate the magnified image of Figure 3.1.6a (bare) and c (2LCP) respectively. The crystal structure of bare corresponds to the layered structure (*R-3m*) when the viewing direction is $[010]_{trigonal}$ and thin NiO layer on the outermost surface was observed. After the surface modification, interestingly, the surface structure of 2LCP was obviously changed to spinel (inner) and spinel-like phase (outer) (Figure 3.1.6d) [11a, 28]; the spinel phase has a diamond configuration with eight Mn columns (Figure 3.1.6j) along the $[110]_{cubic}$ zone axis and the spinel-like has weak contrast in the center of the Mn diamond. It was reported that the structure of Li-rich materials is continuously changed from layered to spinel structure during the electrochemical cycling and the spinel-like phase is considered as a medium state between layered and spinel.[10b] When the lithium ions are extracted, the transition metal ions are migrated to the empty lithium sites which lead to the formation of spinel phase, and ultimately the rock salt NiO phase appeared. In this study, the spinel phase is clearly observed. The reason is believed that when the bare materials were immersed in the acidic solution where the coating precursors were dissolved, the lithium ions were extracted from the lattice at the surface and the lithium deficient phase was formed. Accordingly, after the heat treatment, the structures of the surface were transformed to thermodynamically more stable spinel phase.

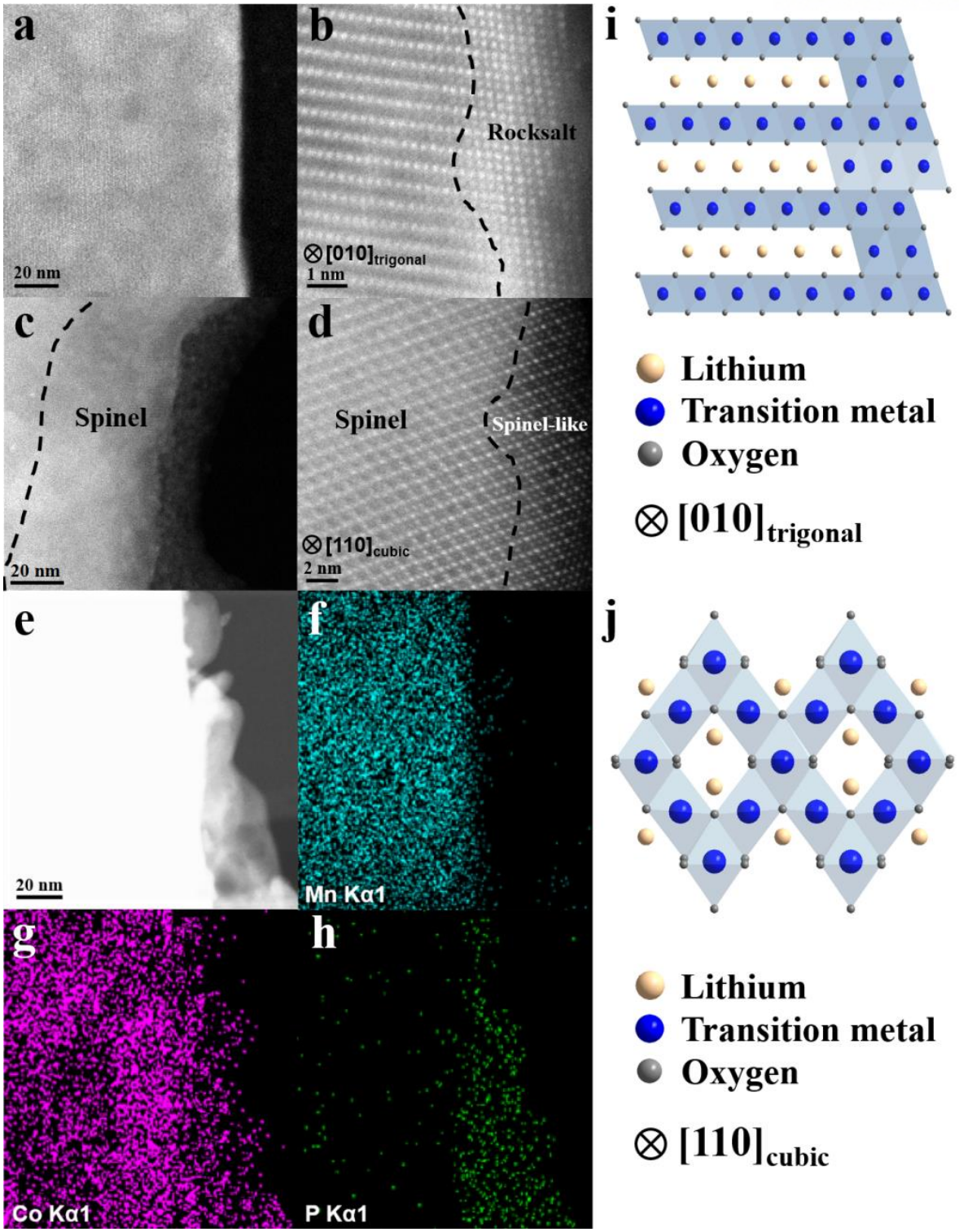

Figure 3.1.6. (a) STEM image of bare, (b) magnified image of (a), (c) STEM image of 2LCP, (d) magnified image of (c), (e-h) EDX mapping results of 2LCP, structural schematic diagrams of (i) layered structure with cation-disorder surface and (j) spinel structure.

The atomic distribution of bare and 2LCP samples was confirmed by the EDX analysis (Figure 3.1.7). In the case of the bare, the atomic ratio of Ni, Co, and Mn is approximately 20, 20 and 60 %, respectively, as we synthesized (Figure 3.1.7a and d). The outermost surface showed slightly higher Ni composition due to the small amount of cation disorder (NiO). However, the transition metal distribution of surface is fully changed after coating. As can be seen in Figure 3.1.7b and e, the concentration of Ni and Mn are deficient, while that of Co is rich compared to the bare. However, in the case of the inner part, the content of Mn is steeply increased, while that of Co is decreased (Figure 3.1.7c and f). The composition of region 2 in Figure 3.1.7c and f is almost similar to that of the bare. Consequently, it is reasonable to deduce that, at heating process, the Co ions preferentially moved to empty lithium sites at the surface region, which resulted in the formation of spinel structure at inner surface and spinel-like phase at outer surface.

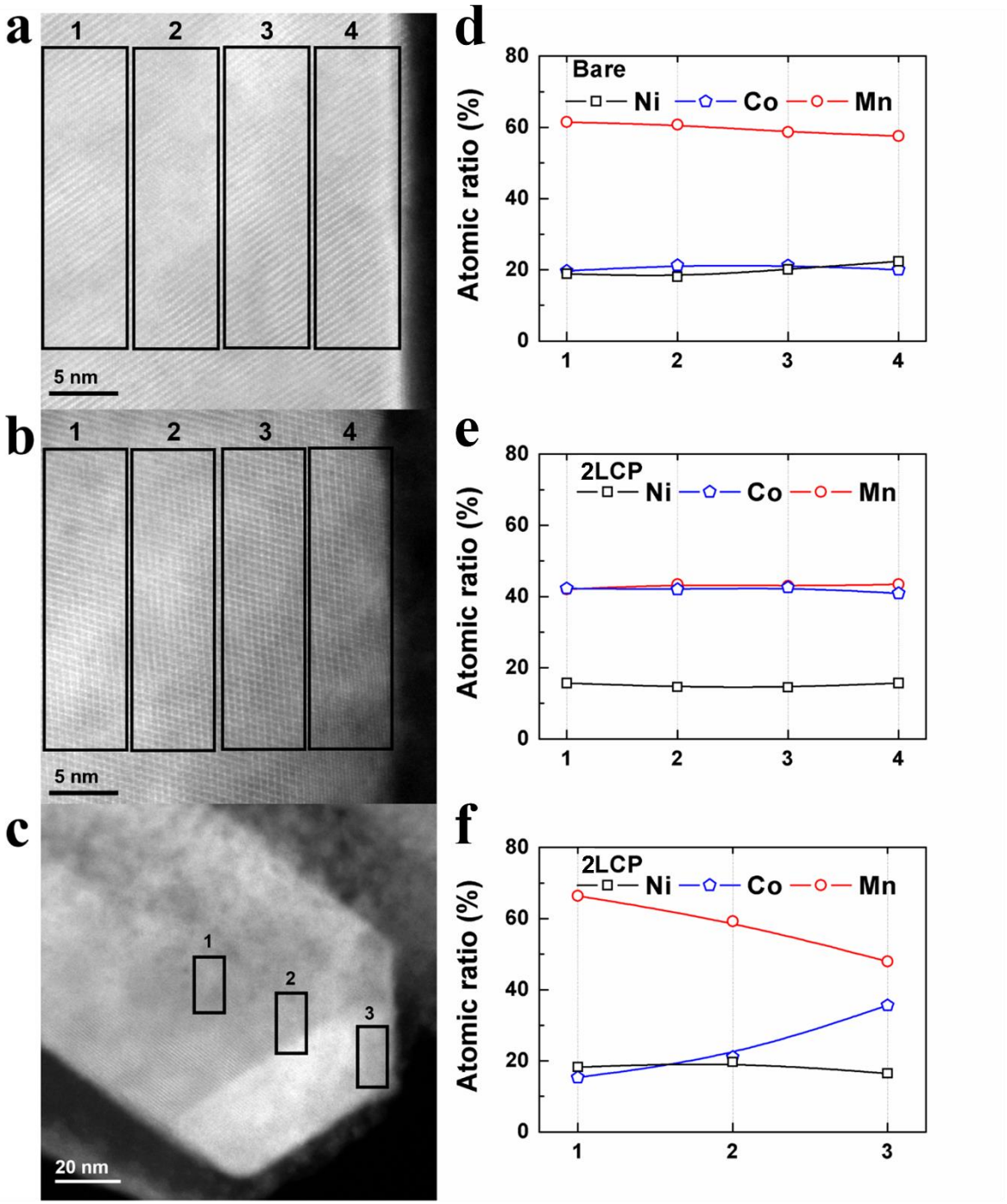

Figure 3.1.7. EDX composition analysis of (a) bare, (b) 2LCP, and (c) low-magnified image of (b), (e-h) EDX mapping results.

Figure 3.1.8a exhibits the initial charge and discharge curves of the bare and 2LCP electrodes between 2.0 and 4.6 V at 0.1 C rate (20 mA g^{-1}) at 24 ºC. The bare electrode delivered a relatively higher charge capacity of 280 mAh g^{-1}, while the 2LCP electrode showed lower charge capacity of 270 mAh g^{-1}. The reason is believed that the lithium ions are extracted from the lattice of Li_2MnO_3 during coating process leading to the decreased charge capacity above 4.4 V region.[20a, 24a, 29] The discharge capacity slightly decreased, which could be due to the reduced portion of active materials. As a result, the coulombic efficiency was improved after the surface modification. Also the unknown plateaus near 2.55 V were found at the 2LCP electrode. This is regarded as the spinel 2.8V plateau based on STEM analysis. However, there is no investigation in this study why it showed the lower potential than that in other reports.[20a, 30] Figure 3.1.8b shows the capacity retentions of the bare and 2LCP electrodes as a function of various C rates from 0.5 C (100 mA g^{-1}) to 12 C (2400 mA g^{-1}) at 24 ºC. The charge rate was fixed at 0.5 C rate. It is obvious that the rate capability of the 2LCP electrode was higher than that of the bare. For an example, the discharge capacity retention of the 2LCP electrode at 12 C was 62.0% (135 mAh g^{-1}) of its discharge capacity at 0.5 C rate, while that of the bare electrode delivered 49.2% (107 mAh g^{-1}). The improved rate capability can be explained by higher lithium diffusion coefficients (D_{Li^+}), which were determined by warburg impedance in the low frequency region (Figure 3.1.9). The D_{Li^+} of 2LCP is 6.92 cm^2 S^{-1}, while that of bare is 1.02 cm^2 S^{-1}. Also the reduced total impedance affected the properties of fast charge and discharge (Figure 3.1.9). The improved D_{Li^+} and reduced resistance are related to the presence of spinel phase on the surface of Li-rich materials. It gives rise to the enhanced electrochemical performances because the 3D structure of spinel provides more facile pathway of lithium ions.[26, 31] Figure 3.1.9c shows exhibits the continuous cycling results of the bare and 2LCP electrodes at 24 ºC, and the charge and discharge current densities were maintained at 1 C rate (200 mA g^{-1}). The capacity retention and working voltages of 2LCP were slightly improved compared to that of bare at 24 ºC (Figure 3.1.9c, d and Figure 3.1.10). These trends of cycling performances were fully changed when the evaluations were carried out at the accelerated test condition (60 ºC). As can be seen in Figure 3.1.9e, f and Figure 3.1.11, the difference of cycling and working voltage retentions between the bare and 2LCP electrodes at 60 ºC became bigger than at 24 ºC due to higher reactivity between the surface of the electrode materials and the acidic electrolyte. The bare electrode showed the dramatic capacity fading due to the dissolution of transition metal and the increased surface resistance resulting from the

byproducts on the surface, while the 2LCP electrode exhibited the much improved cycling performance (Figure 3.1.12). It is well known that the mechanisms of voltage decay in Li-rich layered materials come from the structural change in bulk and the side reaction on surface resulted in large polarization. It was reported that the spinel phase at surface reduced voltage decay in previous papers[20a, 26]. In our result, the artificially induced spinel structure might partly prevent transition metal migration to lithium layers because half of lithium slabs were already occupied by cations to form spinel structure, which led to the alleviated voltage decay at both of 24 ºC and 60 ºC. Also the double protection layers, Ni and Co doped spinel and $LiCoPO_4$ structures, effectively reduced the side reactions on the surface. This result is in good agreement with the electrochemical impedance spectroscopy (EIS) results. Figure 5 shows typical Nyquist plots of the bare and 2LCP samples after every 25 cycles at 60 ºC. Even though it was very difficult to deconvolute each of the surface film (R_{sf}) and charge-transfer resistance (R_{ct}) values from the overlapped semicircles in this study, it is definite that the total impedance of the bare electrode dramatically increased more than that of the 2LCP electrode with increasing cycle numbers. From this, it can be certain that harsher side reactions occurred on the surface of the bare electrode, which leads to worse cycling performance and severer voltage decay.

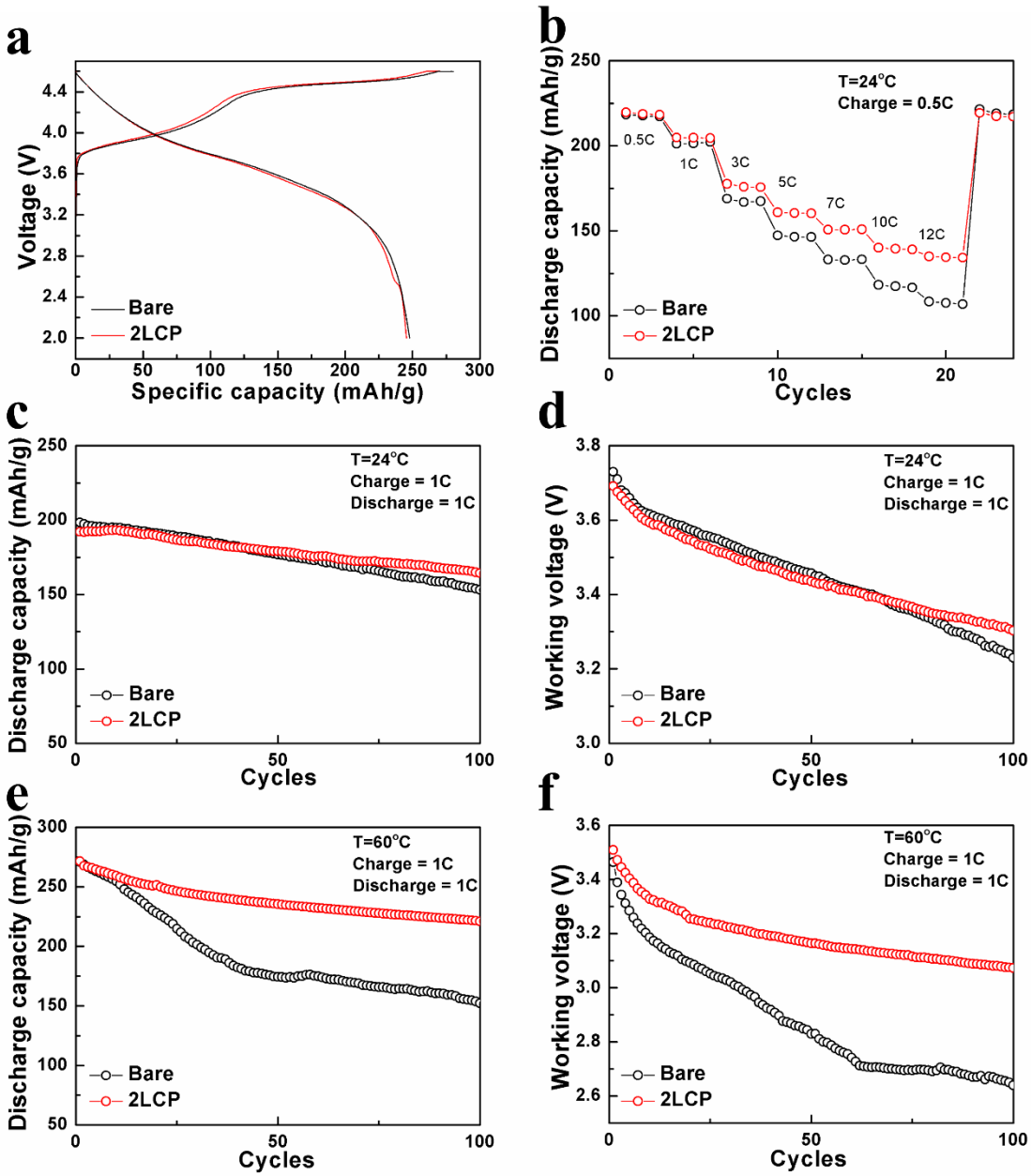

Figure 3.1.8. (a) First charge-discharge curves, (b) discharge capacity retention as a function of various C rates from 0.5 C to 12 C. (c) continuous cycling results at 24 ºC and (d) its working voltages, (e) continuous cycling results at 60 ºC and (f) its working voltage.

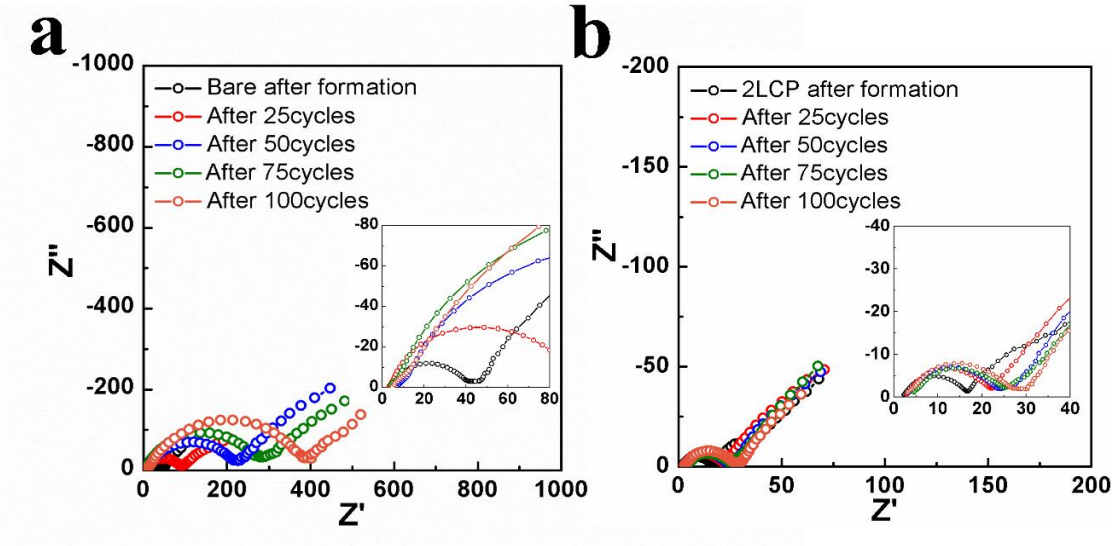

Figure 3.1.9. Nyquist plot for (a) bare, and (b) 2LCP with respect to cycle numbers: 1st, 25th, 50th, 75th, 100th cycles.

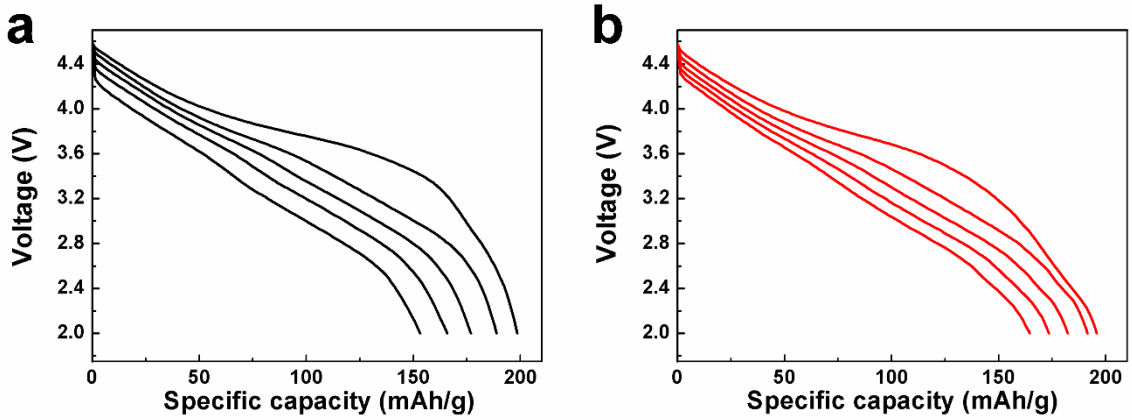

Figure 3.1.10. Charge and discharge profiles of a) bare and b) 2LCP at 24 °C after 1st, 25th, 50th, 75th, 100th cycles.

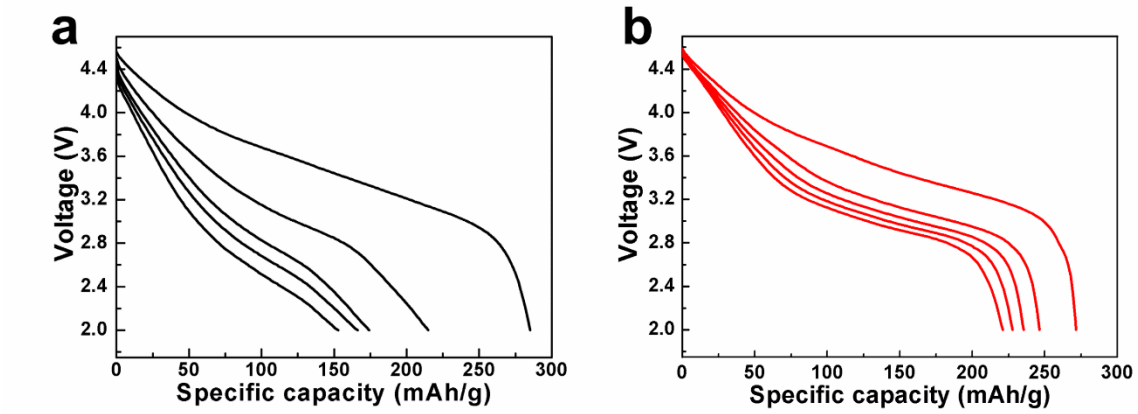

Figure 3.1.11. Charge and discharge profiles of a) bare and b) 2LCP at 60 °C after 1st, 25th, 50th, 75th, 100th cycles.

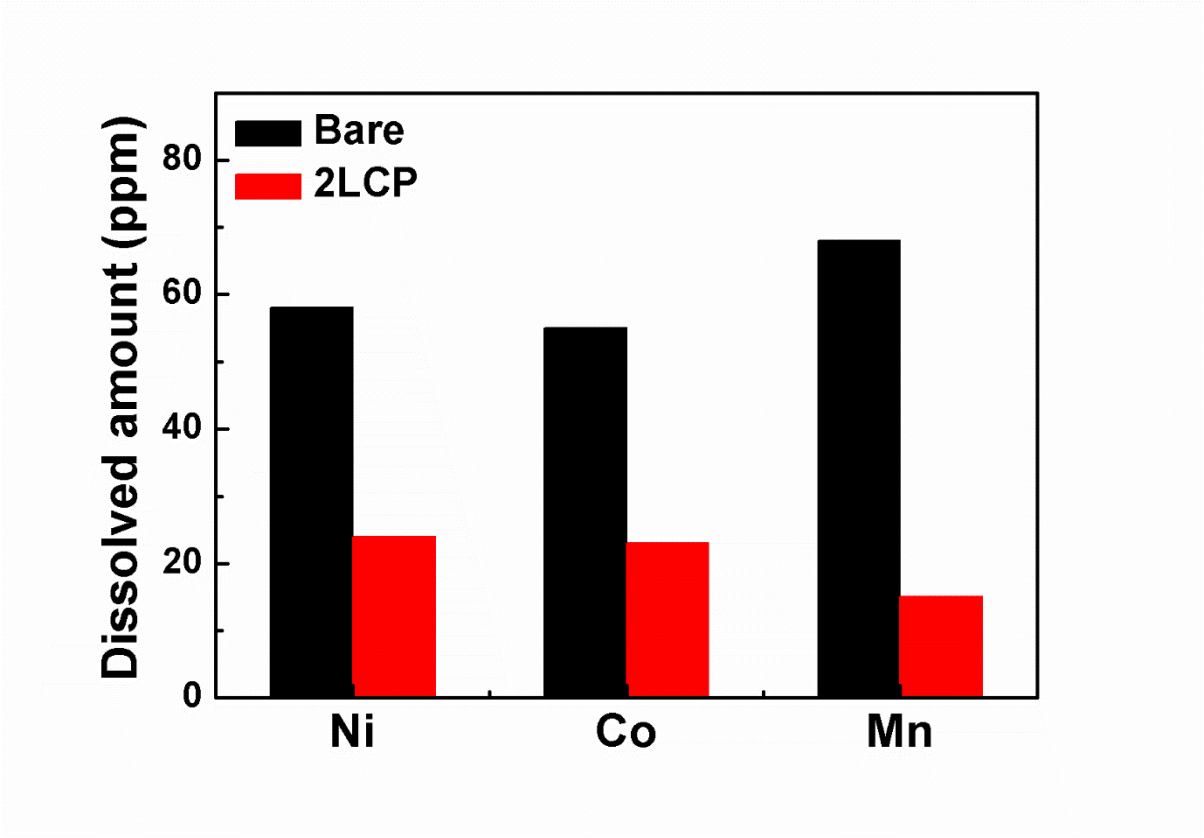

Figure 3.1.12. Transition metals dissolution for electrolyte of the fully charged (4.6V) bare and 2LCP electrodes during 2 weeks at 60 ºC.

The safety issues of cathode materials should be considered for commercialization because it directly affects a battery safety. To evaluate the thermal stability, differential scanning calorimetry (DSC) analysis were carried out. Figure 3.1.13a shows the DSC measurement results of the bare and 2LCP electrodes charged to 4.6 V in the presence of the electrolyte. The main peak of 2LCP at 259 ^{o}C is higher than that of bare at 240 ^{o}C. Moreover, the 2LCP electrode generated significantly lower heat of 398 J g^{-1} than bare electrode (985 J g^{-1}). The improved thermal property is ascribed to the double protection of cation-doped spinel and $LiCoPO_4$ layers, which have a relatively good thermal stability because those materials are not fully delithiated when charged to 4.6V,[32] which causes less structural instability. These stable layers protected the cathode surface from being exposed directly to a highly active electrolyte, thus reducing the exothermic reaction. The measured powders were collected and their structures were characterized by XRD (Figure 3.1.13b). After the DSC analyses up to 350 ^{o}C, the structure of delithiated materials were significantly destroyed. In the case of bare sample, MnF_2 and LiF peaks were observed. In contrast, the patterns of 2LCP sample showed much smaller the peaks intensity of those impurities than bare. When the oxygen released during DSC measurements, Li and Mn ions, which were extricated from oxygen framework, reacted with F ions from lithium salt ($LiPF_6$), which resulted in the formation of MnF_2 and LiF. These results revealed that the double protection layers effectively reduced contact area between the surface of 2LCP and electrolyte, which contributed to the cycling and thermal stability.

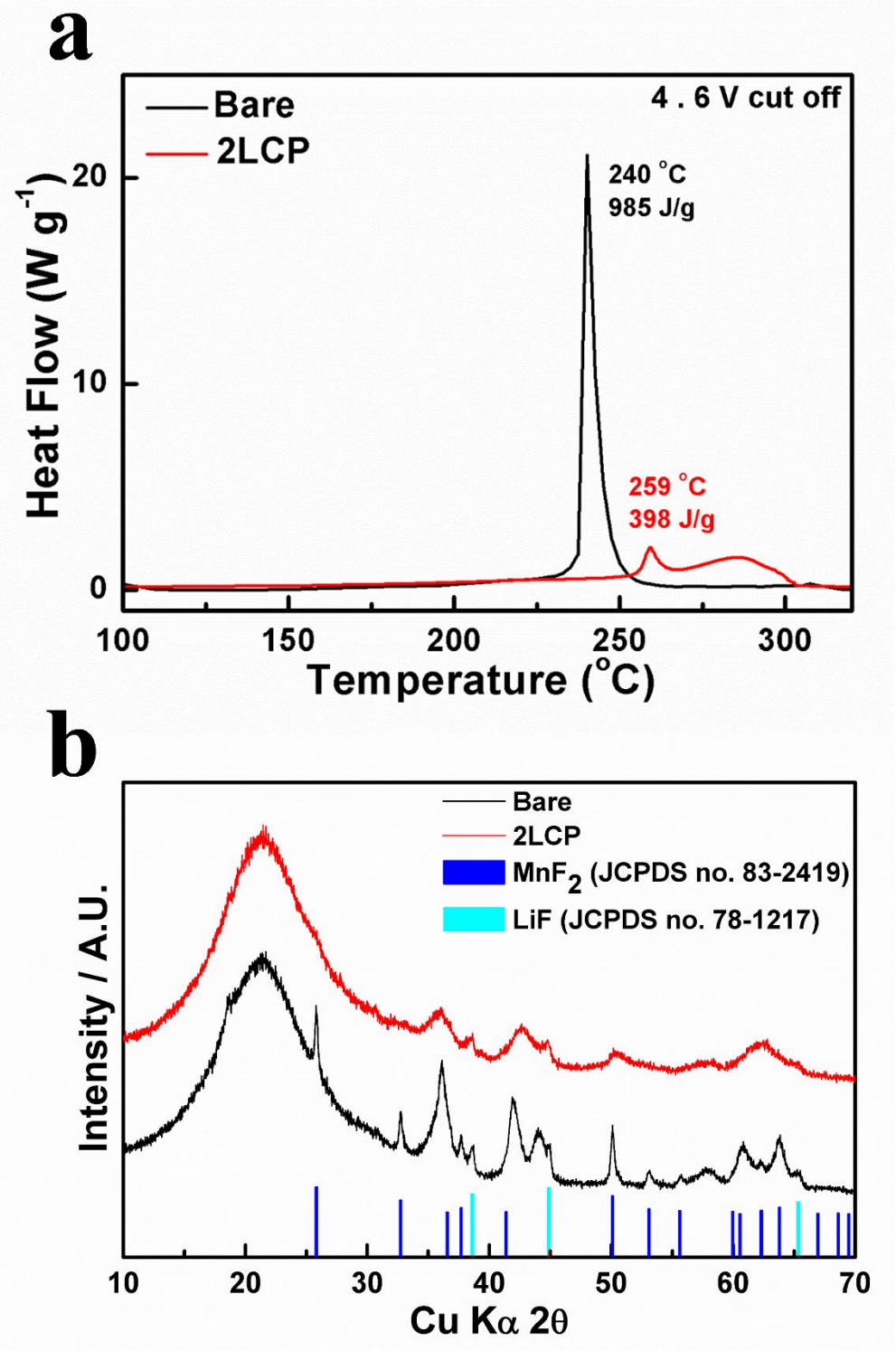

Figure 3.1.13. (a) DSC of bare and 2LCP at 4.6 V, (b) *Ex*-situ XRD patterns of samples; powders after DSC measurement from 50 ºC to 350 ºC.

3.1.4 Conclusions

In summary, we successfully synthesized $LiCoPO_4$ coated $0.4Li_{2-x}MnO_3$-$0.6LiNi_{1/3}Co_{1/3}Mn_{1/3}O_2$ material by using the dual functioned coating method without formation of lithium impurities. The chemical activation and surface coating with $LiCoPO_4$ were carried out simultaneously. The spinel structure with higher Co and lower Mn content than inner part was observed on the surface of host particles, and the concentration of Co was gradually reduced to inward direction, which was identified via STEM and EDX analyses. The presence of spinel on the surface provided the facile pathway of lithium, which led to the superior rate capability. The double protective layers, $LiCoPO_4$ and cation-doped spinel, not only effectively suppressed the side reactions resulting in the improved cycling performances, especially at 60 ^oC, but also protected the highly oxidized cathode materials from direct contact with the electrolyte leading to the superior thermal stability. In addition, the spinel structure on the surface might hinder transition metal ions from migrating to lithium layers. Consequently, the simultaneous surface modification method of the chemical activation and surface coating is the simple and efficient strategy to enhance the electrochemical and thermal properties. We believe that this concept could contribute the progress of industry as well as research area. Since the voltage decay originates from change of bulk structure as well as surface structure during cycling, fundamental researches on bulk structure is necessary to completely prevent voltage decay.

3. 2. High Performance $LiMn_2O_4$ Cathode Materials Grown with Epitaxial Layered Nanostructure for Li-ion Batteries

3. 2. 1. Introduction

Lithium ion batteries achieved a great success as an energy source for small portable electronic devices such as cell phones and lab-top computers. Now, interest of people moves to electric vehicles (EVs) that equip an engine operated by lithium ion batteries instead of gasoline. The commercialization of lithium ion batteries for the electric vehicles (EVs) requires a cathode material with high energy and power, high thermal stability, low cost, and other criteria such as excellent cycle life and low ion and electronic transport resistance. To meet the above requirement, many research groups have extensively and intensively investigated many possible cathode materials such as $LiCoO_2$, $LiNi_{1-x-y}Co_xMn_yO_2$, $LiMn_2O_4$, and $LiFePO_4$ for the applications in EVs' batteries. Among many cathode candidates, the $LiMn_2O_4$ has been considered as one of the most promising cathode material to be used for EVs due to its advantages of low cost, abundance, environmental affinity, and low safety hazard, which are the key factors for a large scale EV battery. [19a, 19b, 33] However, it still suffers from a fast capacity fading at 60 ^oC because the manganese on the surface of the $LiMn_2O_4$ dissolves in the liquid electrolyte solution containing acidic species.[34] To solve this problem, many researchers have attempted to have the $LiMn_2O_4$ surface coated by inorganic materials such as Al_2O_3, $AlPO_4$, AlF_3, ZrO_2 and SiO_2.[35] The coating materials acted as a protective layer that prevents the host $LiMn_2O_4$ from being exposed directly to the electrolyte. However, the coating layer also acted as a resistance layer when its thickness is too large, which results in deteriorating electrochemical performance. For this reason, the electrochemically and electrically active materials have been considered as potential coating candidates for the $LiMn_2O_4$ cathode.

Recently, our group found that the electrically conductive carbon coated on the surface of the $LiMn_2O_4$ is very effective for improving its electrochemical performances and stability at the room temperature. However, when the carbon coated $LiMn_2O_4$ was tested at the high temperature of 60 ^oC under the same experimental condition, its electrochemical performances deteriorated rapidly.[36] Other groups reported that surface coating with electrochemically active materials such as $LiNi_{0.5}Mn_{1.5}O_4$, $LiCoO_2$, $Li_4Ti_5O_{12}$, and $LiNi_{0.05}Mn_{1.95}O_4$ are also effective ways to improve the electrochemical performances of the $LiMn_2O_4$ at the room temperature. [35a, 37] However, those attempts have not been

well successful at the elevated temperature. For example, $Li_4Ti_5O_{12}$-coated $LiMn_2O_4$ exhibited a discharge capacity of ~90 mAh g^{-1} and retained less than 80% of its initial capacity at 55 ºC after 40 cycles. [35a]

Therefore, it has been requested to find a new strategy of designing the optimized coating layer for the $LiMn_2O_4$ cathode that can be operated in harsh and high temperature EV environments. In addition to morphology, thickness, and electronic and electrochemical properties, the coating layer needs to satisfy an additional requirement such as a chemical affinity between a host material and a surface layer. This condition may provide a better sustainable coating layer on its host cathode material without forming any crystal defect so that it can be operated in a harsh environment for a longer time. For this reason, the Mn rich layered phase has been considered as the one of the potential coating candidates for the $LiMn_2O_4$ cathode. The Mn rich layered phase that consists of Mn^{4+} such as $LiNi_{0.5}Mn_{0.5}O_2$ [21a, 38] was additionally considered to eliminate the possibility of the Mn^{2+} dissolution in electrolyte.

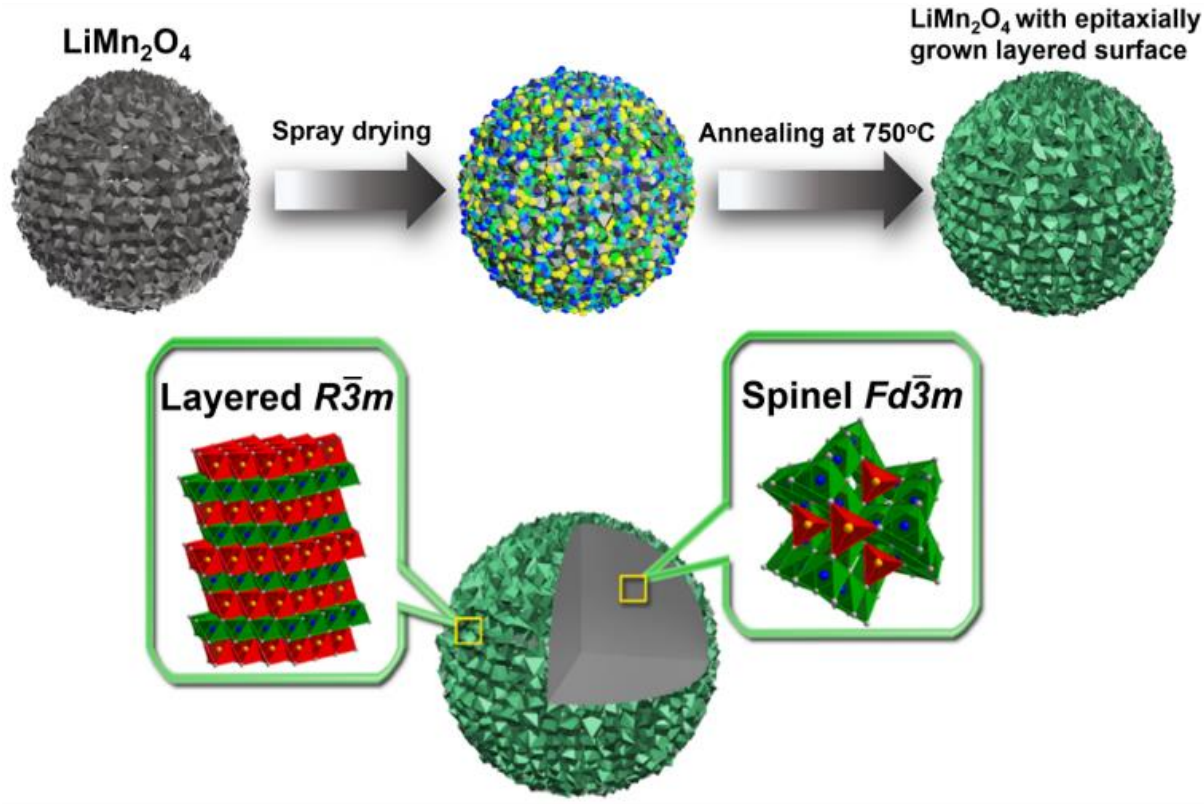

Figure 3.2.1. Schematic view of fabrication process and a spinel particle surrounded by layered phase surface.

After many experimental trials and errors, herein, we reported a new class of the hetero-structured spinel cathode. This material was synthesized via the simple method of spray drying coating solution and further heat treatment (Figure 3.2.1). The Mn rich layered phase (< 10 nm thick) was epitaxially grown on the surface of the spinel $LiMn_2O_4$ host cathode without forming any defect. To the best of our knowledge, this unique structure is first reported and shown with an atomic scale. The developed material showed excellent electrochemical performances at various temperature range relative to the spinel $LiMn_2O_4$.

3. 2. 2. Experimental

Synthesis. Bare $LiMn_2O_4$ powder was synthesized via a typical solid-state reaction. Mn_3O_4 and Li_2CO_3 were mixed based on the desired amount of stoichiometric $LiMn_2O_4$, then calcined at 770 °C for 17hr in a box furnace under a flow of oxygen gas. One percent of excess lithium in molar ratio was used due to the volatilization of lithium at high temperature. After calcination, $LiMn_2O_4$ powder was thoroughly mixed and heated additionally at 750 °C for 3h to eliminate the heat treatment effect on its electrochemical performances[39] and this sample was used for the BLMO. The no addition-heated $LiMn_2O_4$ samples were coated by 5 wt% of layered $LiNi_{0.5}Mn_{0.5}O_2$ via a spray drying process. The coating via spray drying process has an advantage of uniformly covering particle but it is difficult to get uniform thickness due to rough particle surface. A desired amount of $Li(CH_3COO)\cdot 2H_2O$, $Ni(CH_3COO)_2\cdot 4H_2O$ and $Mn(CH_3COO)_2\cdot 4H_2O$ were dissolved in distilled water at 80 °C and the as-prepared $LiMn_2O_4$ powder was slowly immerged to coating solution under stirring. After stirring for 15min, the solution with $LiMn_2O_4$ powder was spray-dried at 200 °C. In order to obtain the hetero-structure $LiMn_2O_4$ coated by layered phase, the dried powder was heated in box furnace at 750 °C for 3h under oxygen atmosphere.

Characterization. The crystalline phase was analyzed by powder X-ray diffractometer (XRD, D/MAX-2200V, Rigaku) using Cu Ka radiation. The morphology of prepared powders was examined using scanning electron microscopy (SEM, S-4800, HITACHI). Transmission electron microscopy sample was prepared by focused ion beam (FIB, Quanta 3D FEG, FEI). The high resolution-transmission electron microscopy (HR-TEM, JEM-2100F, JEOL) operating at 200 kV was used for analyzing a microstructure with an atomic scale.

Electrochemical test. Galvanostatic charge and discharge cycling was carried out using CR2016 coin-type, which consists of a cathode and a lithium metal anode separated by the porous polypropylene film. The cathode electrodes were fabricated by blending the prepared powders (95 wt%), Super P carbon black (2.5 wt%) and polyvinylidene fluoride (2.5 wt%) in *N*-methyl-2-pyrrolidone. The slurry was applied on Al foil and dried in an oven at 110 °C for 20min. The dried electrode was roll-pressed. The cells were assembled in a glove box filled with dried argon gas. The electrolyte solution was 1.1 M $LiPF_6$ in mixture of ethylene carbonate (EC) and diethyl carbonate (DEC) in 1 : 1 volume ratio (PANAX ETEC CO. Ltd., Korea). For the test at low temperature, the coin type cells were charged to 4.3 V at 0.1 C rate, kept 4.3 V until when the current decreased to 0.05 C rate (6.5 mA g^{-1}), and then discharged to 3.0 V at the constant current of 0.1 C. For the GITT measurement, the cells were galvanostatically charged and discharged in two cycles at 0.1 C rate between 3.0 and 4.3 V at 24 °C. The GITT was employed at a constant current pulse of 13 mA g^{-1} (=0.1C rate) for 40 min, and then an open-circuit

stands for 60 min to relax the cell voltage to the steady state. Electrochemical impedance spectroscopy (EIS) was performed from 0.02 to 250 kHZ frequency range using electrochemical interface system (IVIUM) on coin-type half cells at SOC 90%.

3. 2. .3 Results and Discussion

The XRD patterns of the bare $LiMn_2O_4$ (denoted as BLMO) and the epitaxially grown layer coated $LiMn_2O_4$ (denoted as EGLMO) powders exhibited a well-defined cubic spinel phase of space group $Fd\bar{3}m$ without impurity peaks (Figure 3.2.2). The XRD peaks of the layered surface phase were not able to be observed because of the similarity of XRD patterns between the layered surface and spinel host structure as well as the small content of the layered phase (5 wt%). It could be possible for a small amount of Li and Ni atoms of the layered phase to diffuse into the host spinel particle during annealing at 750 ^{o}C. This speculation can be explained that the lattice parameter of BLMO (8.233 Å) was slightly changed to that of EGLMO (8.229 Å) after coating due to the decrease in quantity of the larger Mn^{3+}.[40]

The surface morphologies of three samples, BLMO, BLMO covered by coating precursor (right after spray drying), and EGLMO, were confirmed by SEM (Figure 3.2.3a, b and c). The surface morphology of the BLMO was spherical and dense with secondary particle size of approximately 15 μm in diameter. Just after spray drying, the dried coating precursor (Li:Ni:Mn = 1:0.5:0.5) was well covered on the surface of the BLMO. After heating at 750 ^{o}C, the morphology of the EGLMO was similar to that of the BLMO, where nickel elements were observed to be evenly distributed according to the energy dispersed X-ray analysis (Figure 3.2.3d, e and f). An average particle size (D50) and tap density of EGLMO were ~ 15 μm and 2.3g/cc, respectively.

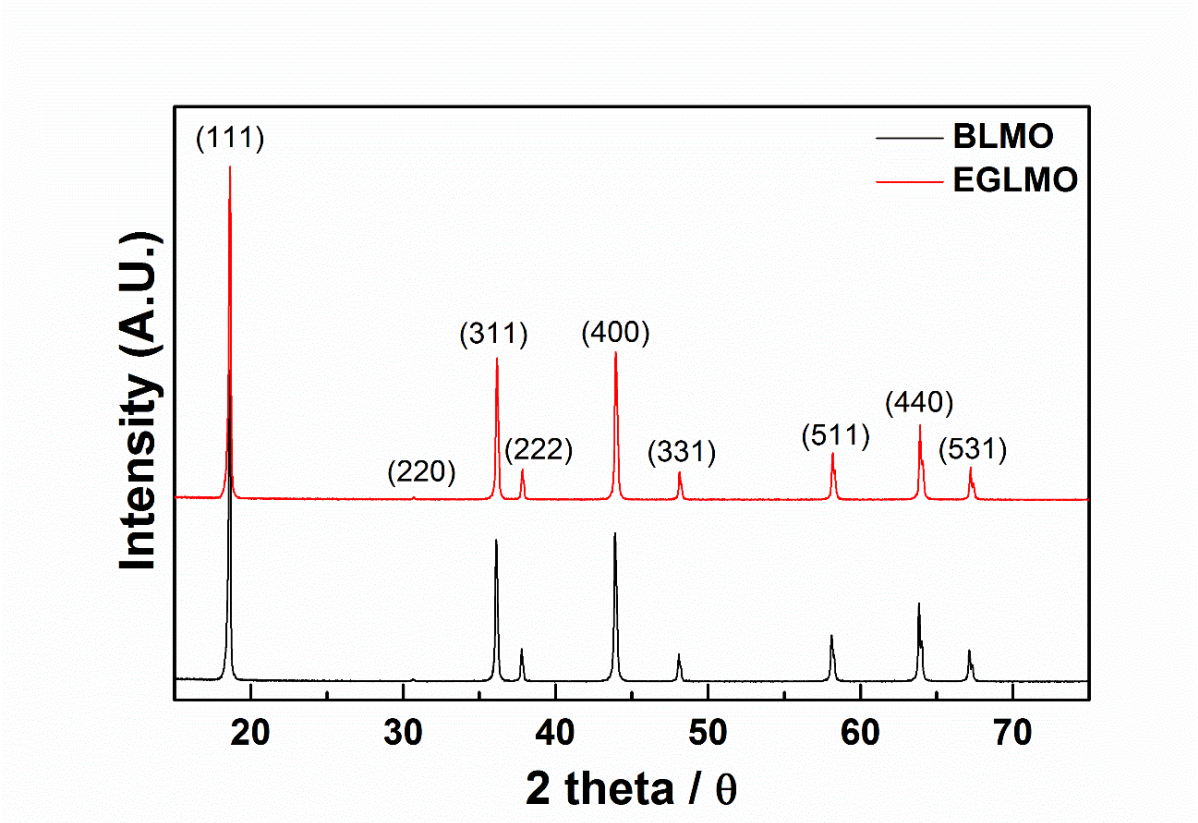

Figure 3.2.2. Power XRD patterns of BLMO (Bare $LiMn_2O_4$) and EGLMO (epitaxially grown layer coated $LiMn_2O_4$).

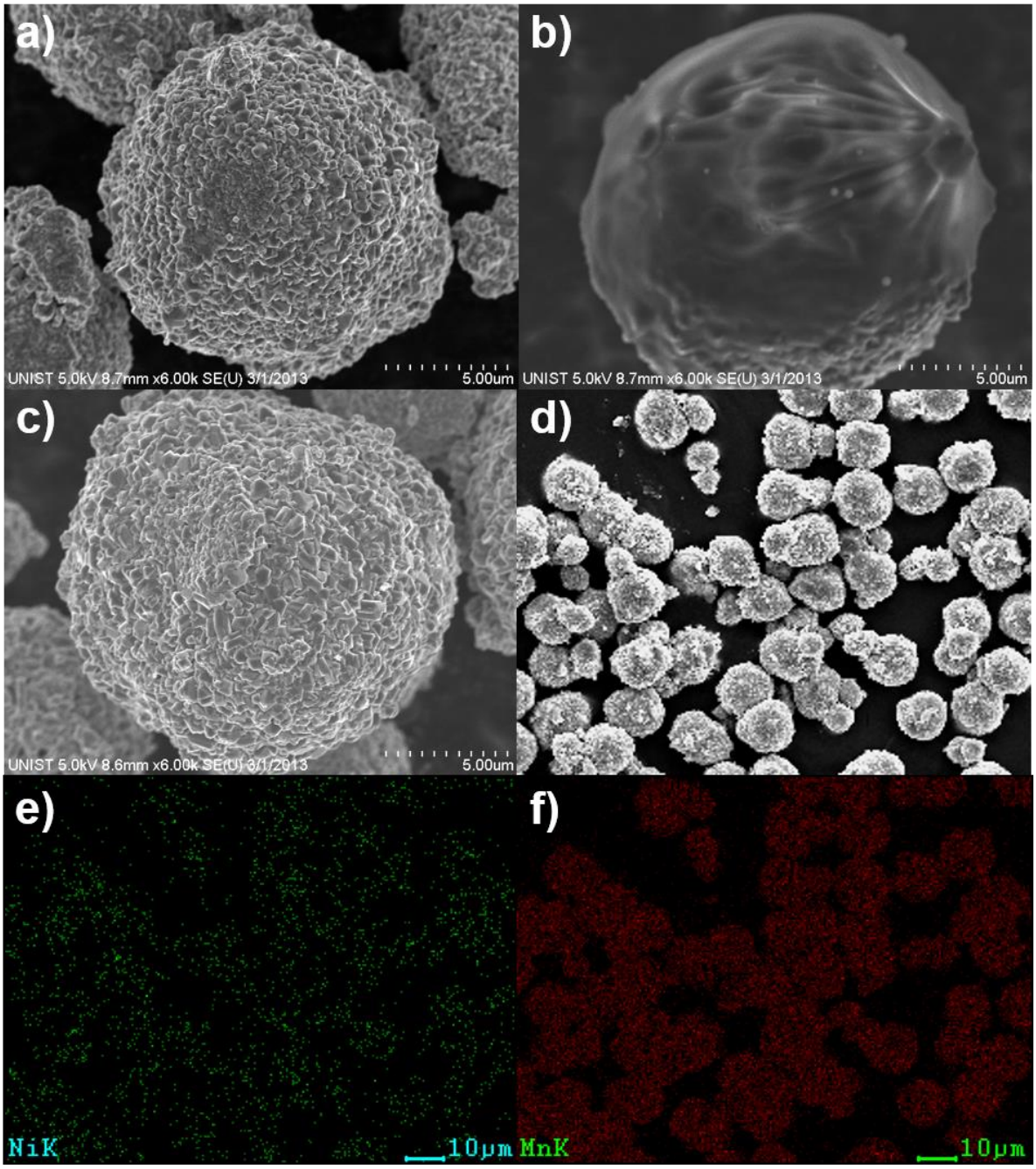

Figure 3.2.3. SEM images of a) BLMO, b) BLMO covered by coating precursor (right after spray drying), c) EGLMO and d) low magnified image of the EGLMO. Energy dispersed X-ray analysis of each element e) Ni and f) Mn.

To analyze microstructures of the samples with an atomic scale, the measurement of the high-resolution scanning transmission electron microscopy (STEM) was performed. Figure 3.2.4a shows high-angle annular dark-field (HAADF) STEM image of the EGLMO particles that are cross-sectioned. The selected area (red square) in Figure 3.2.4a is magnified in Figure 3.2.4b. It is obviously observed in the STEM image of Figure 3.2.4b that the structure of the region B (surface layer) is different from that of the region A (host). They are directly connected each other without forming any defect. This is called the epitaxial layer that indicates the deposited overlayer on the surface of the host material along with the same lattice orientation.[41] In order to form this unique structure, the coating material with a < 10nm thickness must have a same oxygen framework with respect to the host spinel crystal structure. The cubic spinel and hexagonal layered phase are based on the cubic close packing (CCP) array of the oxygen ions[42], where the transition metal ions of both phases are located in octahedral sites. Based on the chemical and structural affinities between the host and coating materials, the hexagonal layered phase can be epitaxially formed on the surface of the bulk spinel phase, which results in the formation of the hetero-structure. Figure 3.2.4c is a fourier filtered image of the region A and its structural schematic diagram is shown in Figure 3.2.4e. These figures indicates a typical cubic spinel phase ($Fd\bar{3}m$) along the $[110]_{cubic}$ zone axis.[42] The manganese atoms are arranged like a diamond shape with Mn columns showing two different contrasts. The brighter Mn columns in Figure 3.2.4c have twice higher atomic density than that of the less bright Mn columns along the $[110]_{cubic}$ direction. Surely, no contrast from Li sites can be confirmed because Li is a light element. Figure 3.2.4d (Region B in Figure 3.2.4b) corresponds the layered structure ($R\bar{3}m$) along the $[2\bar{2}1]_{hexagonal}$ zone axis, and its structural diagram is shown in Figure 3.2.4f. In contrast to the host structure (Figure 3.2.4e), there is no empty site in the structure of the surface phase (Figure 3.2.4f), which means the column consists of only invisible atoms such as Li when viewing direction is the $[2\bar{2}1]_{hexagonal}$. Also all columns have same contrast due to same density of transition metal atoms (Ni or Mn) along the viewing direction. The epitaxial relationships between the host spinel and the surface layered phase determined from the STEM images (Figure 3.2.5) are $(2\bar{2}2)_{spinel}//(10\bar{2})_{layered}$ and $(\bar{2}22)_{spinel}//(012)_{layered}$. As can be seen, the *d* spacing values of the host (2.37Å) and surface (2.36Å) lattice are well matched each other. Based upon the TEM results, we confirmed that the surface of the EGLMO was not a spinel phase but a layered phase as we designed. Furthermore, the HAADF STEM image (Figure 3.2.6) that was taken from another region of the primary particle at the surface supports the existence of the layered phase even at inner surface.

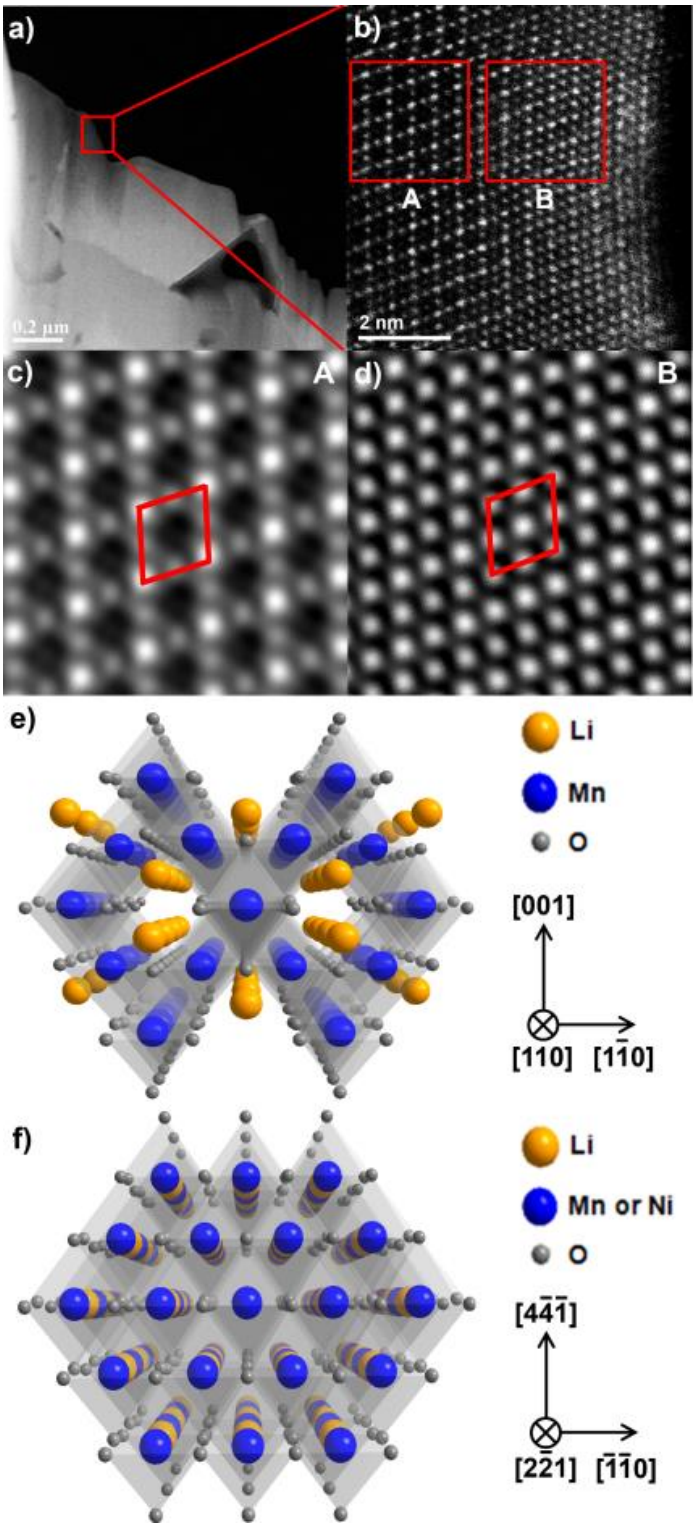

Figure 3.2.4. a) HAADF STEM images of surface of cross sectioned particle of EGLMO. b) Magnified images of a). c and d) Fourier filtered images of region A and B, respectively, in b). e and f) Structural schematic diagrams of c and d)

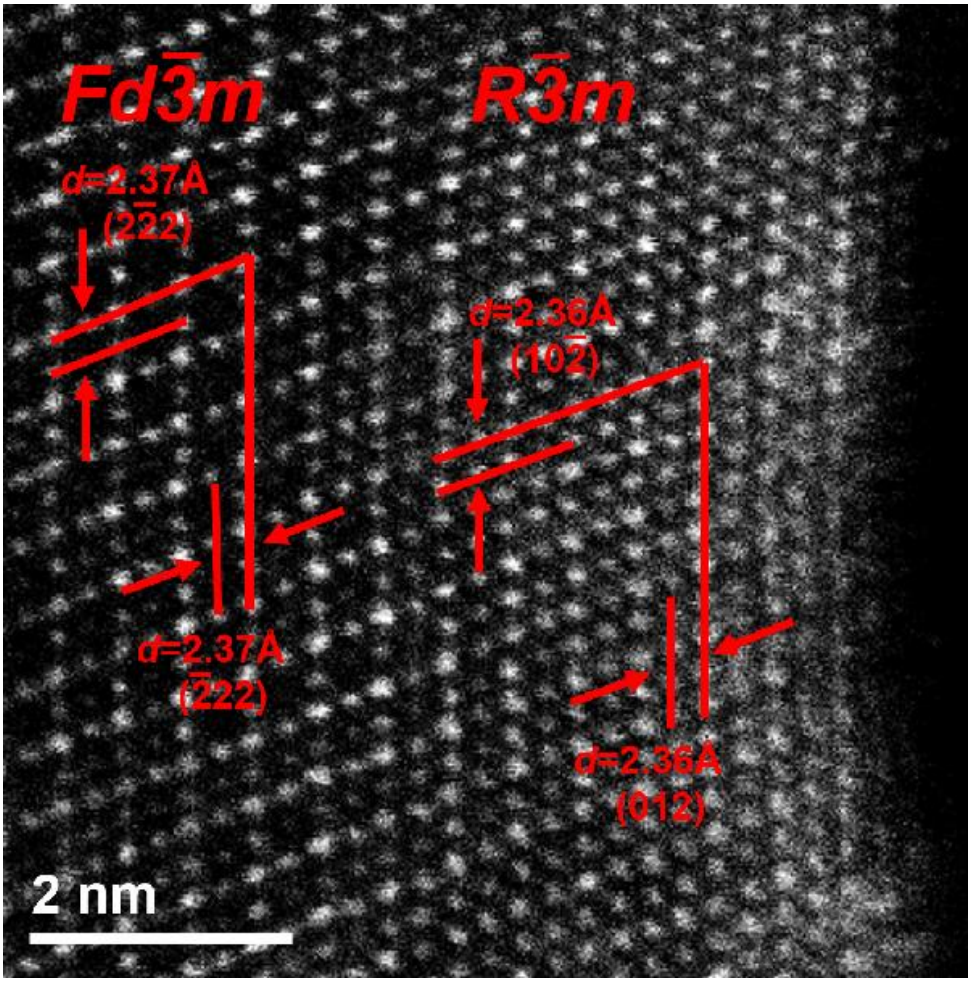

Figure 3.2.5. HAADF STEM image of surface of cross sectioned particle of EGLMO.

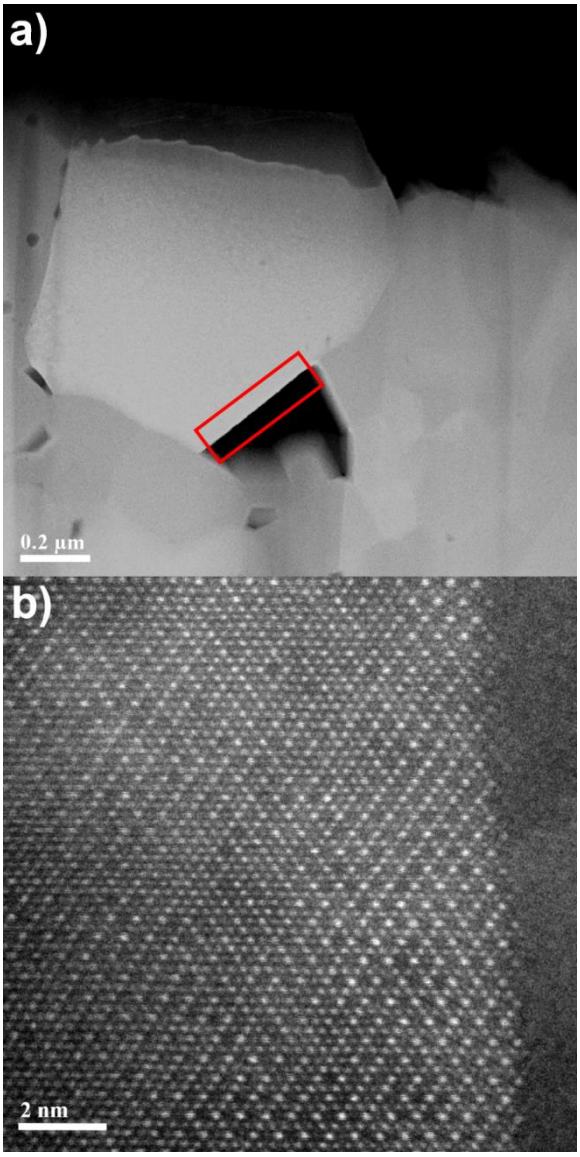

Figure 3.2.6. HAADF STEM images of a) surface of cross sectioned particle of EGLMO. b) magnified image of selected area in a).

To understand the formation mechanism of the epitaxial layer, the BLMO covered by the dried coating precursor heated at 600 ºC for 10 min was prepared and analyzed by using the STEM (Figure 3.2.7). As shown in the images of the surface in the sample, three types of structure could be found, and it was already confirmed that the region A and B indicated layered phase and spinel phase respectively. The region C indicates M_3O_4 (M=Ni, Mn) with space group *I*41/*amd* along the $[100]_{tetragonal}$ zone axis and its structural diagram is shown in Figure 3.2.7c. It also has CCP oxygen array[11a, 43], and is epitaxially connected to region B. Figure 3.2.7b shows the distribution of Ni and Mn atoms by EDX mapping in the crystalline regions B and C of the layered and M_3O_4 (M=Ni, Mn) phases, and amorphous region of outside of crystalline region. It was confirmed that Ni atoms were distributed on two regions as well as the amorphous surface region. Accordingly, M_3O_4 (M=Ni, Mn) was epitaxially formed on the surface of BLMO at first, and then Li ions diffused to M_3O_4, leading to the formation of the layered phase. These processes were repeated continuously until all Ni and Mn atoms were used entirely.

There may be controversy over the same column projection of layered structure and rock salt NiO. In order to confirm this, the intensity profile of Z-contrast was measured (Figure 3.2.8a and b). As mentioned above, brighter Mn columns (Mn_α) have twice higher atomic density than less bright (Mn_β) columns when viewing direction is [110] (Figure 3.2.8c). The atomic density of Mn_β is as same as that of layered structure along the $[2\bar{2}1]$ zone axis (Figure 3.2.8d). Also that of Mn_α is equal to that of rock salt NiO (Figure 3.2.8e). As can be seen in Figurexx, the intensity of Mn_β is similar with that of layered region, which is the strong evidence that layered phase was successfully formed on the surface of spinel cathode material, not NiO phase.

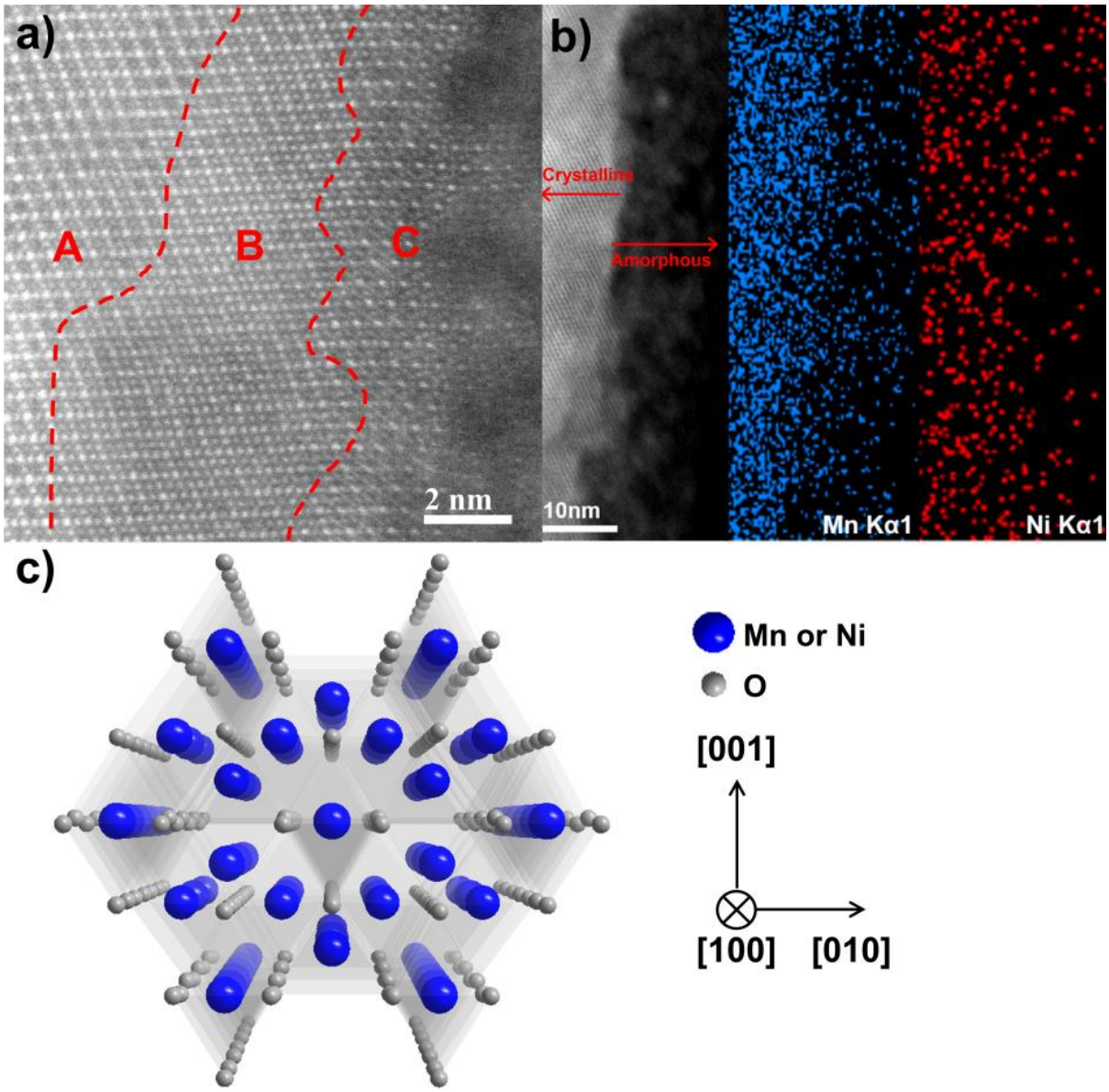

Figure 3.2.7. a) HAADF STEM image of a primary particle at the surface of a sample prepared by heating at 600 ºC for 10 min and quenching. b) EDX mapping of manganese (blue) and nickel (red) of region B and C in a). c) Structural schematic diagram of region C

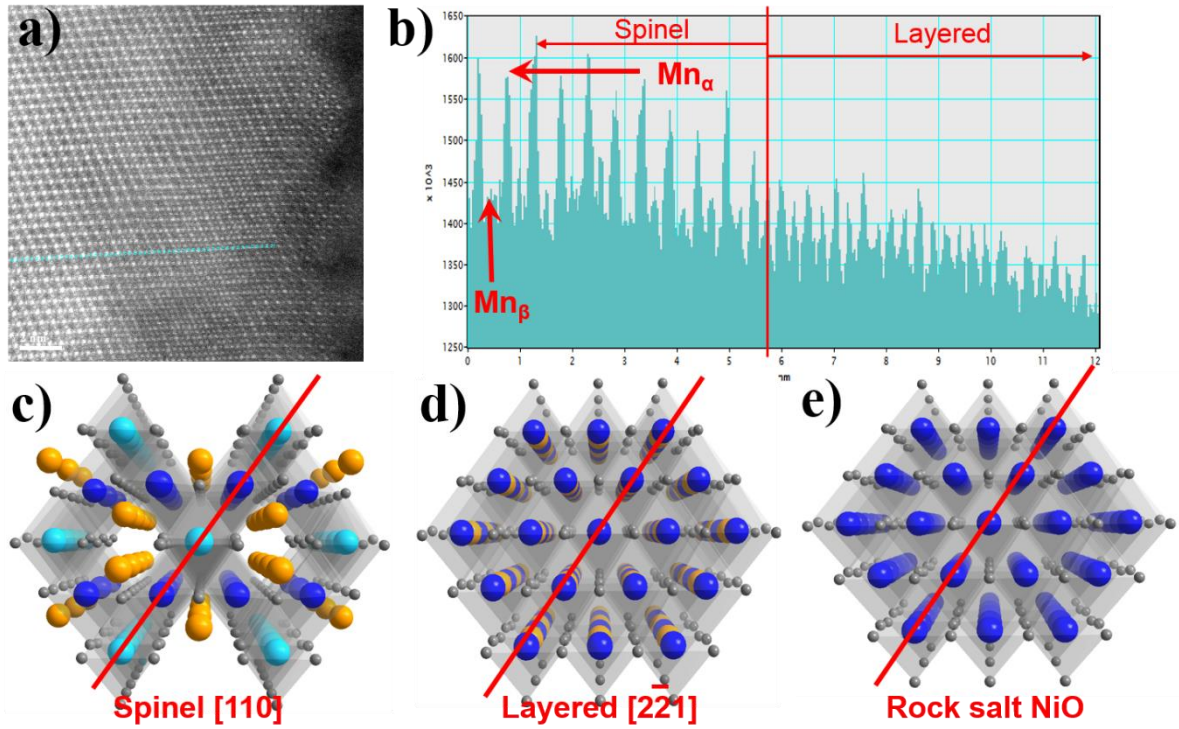

Figure 3.2.8. a) HAADF STEM image of a primary particle at the surface of a sample prepared by heating at 600 ºC for 10min and quenching. b) Intensity profile along blue line in a). c) Structural schematic diagram of spinel, d) layered and e) rock salt NiO phase

It should be noted that the experimental preparation of our electrodes was optimized to meet the need of industry that uses relatively high loading level of the active material (9.0~9.2 mg cm^{-2}) and a small content of conductive agent (2.5 wt%). Figure 3.2.9a exhibits the first charge and discharge curves of the BLMO and EGLMO electrode, respectively, between 3.0 and 4.3 V at 0.1 C rate (=13 mA g^{-1}) at 24 °C. The BLMO electrode delivered a relatively high discharge capacity of 131 mAh g^{-1} with the coulombic efficiency of 99% while the EGLMO showed a slightly lower capacity of 123 mAh g^{-1} with the coulombic efficiency of 100%. During the heating process, a small amount of Li and Ni in the surface layer was diffused into the host $LiMn_2O_4$, which led to the decrease in quantity of the Mn^{3+}.[40] This could be the major cause for the decrease in the EGLMO's initial discharge capacity. Also the decreased initial irreversible capacity of the EGLMO (Figure 3.2.9a) was due to the suppression of a solid electrolyte interphase (SEI) formation by the stable surface.[44] Figure 3.2.9b exhibits the continuous cycling results of the BLMO and EGLMO, respectively, at 60 °C, and the discharge current density were maintained at 1C. The structural stability of the spinel cathode is directly related to the dissolution of Mn^{2+} ions into the electrolyte at elevated temperatures, and especially the temperature of 60 °C has been widely regarded as the most critical temperature in the industries[23]. In addition, since reduction of Mn^{2+} ions has influences on the anode electrode regardless of using metallic lithium or graphite [34c, 37a, 37b, 40b, 45], it is very important to stabilize the surface structure of the spinel. After 100cycles, the discharge capacity of the EGLMO retained approximately 85% of its initial capacity, while the BLMO showed the poor capacity retention of 56% at 60 °C. Also the discharge working voltage of the BLMO electrode dramatically decreased upon increasing the cycle number (Figure 3.2.10). On the other hand, the discharge voltage of the EGLMO electrode maintained approximately 4.0 V from 1st to 100th cycles. *Ex*-situ XRD was carried out to investigate a structure change of the BLMO and EGLMO after 100 cycles (Figure 3.2.11). The XRD peaks of both electrodes were significantly broadened compared to those of powder before cycling. After cycling, the manganese compounds such as MnF, MnF_2[15] on the surface and the degraded crystallinity caused the broadening of XRD peaks. The XRD pattern of the BLMO showed the impurity phase of a tetragonal $Li_2Mn_2O_4$ (*I*41/*amd*), which was reported that under dynamic and non-equilibrium conditions, over-lithiated $Li_{1+x}Mn_2O_4$ phase was formed on the spinel surface as the degradation product of the cycled $LiMn_2O_4$ at ambient and elevated temperature. [46] However, no impurity peaks were observed in the XRD pattern of the EGLMO. This was believed to be that the layered phase on the EGLMO's surface suppressed the formation of tetragonal $Li_2Mn_2O_4$ (*I*41/*amd*). The discharge capacity variations of the BLMO and EGLMO stored in the charged state at 60 °C are exhibited in Figure 3.2.9c and d, respectively. The capacity loss of the EGLMO was only 1% after storing for 2 weeks, whereas the BLMO showed 10% loss of its initial capacity. It has been well established that the effects of manganese content in the spinel and layered phase on their electrochemical performances were entirely different. In the case of the spinel

cathode material, the relatively higher manganese content contributes to its higher gravimetric capacity, but its negative effect is the decrease in cycling performance due to the manganese dissolution.[40] On the other hand, the layered cathode material with relatively high manganese content exhibits a lower capacity but better cycling performance and thermal stability.[47] As a result, the improved cycling and storage performance of the EGLMO at 60 ^{o}C could be related to the Mn-rich layered phase formed on the EGLMO's surface. The newly developed material of the EGLMO has the advantages of the layered and spinel structures with high manganese contents. The bulk of spinel phase with a high manganese content delivers a high capacity because its valence state of manganese is +3.5 which shows the maximum capacity among the spinel materials. The layered phase on the EGLMO's surface provides a longer cycle life and better thermal stability by acting as the protecting layer that prevents the bulk spinel from being exposed directly a highly active electrolyte at 60 ^{o}C.

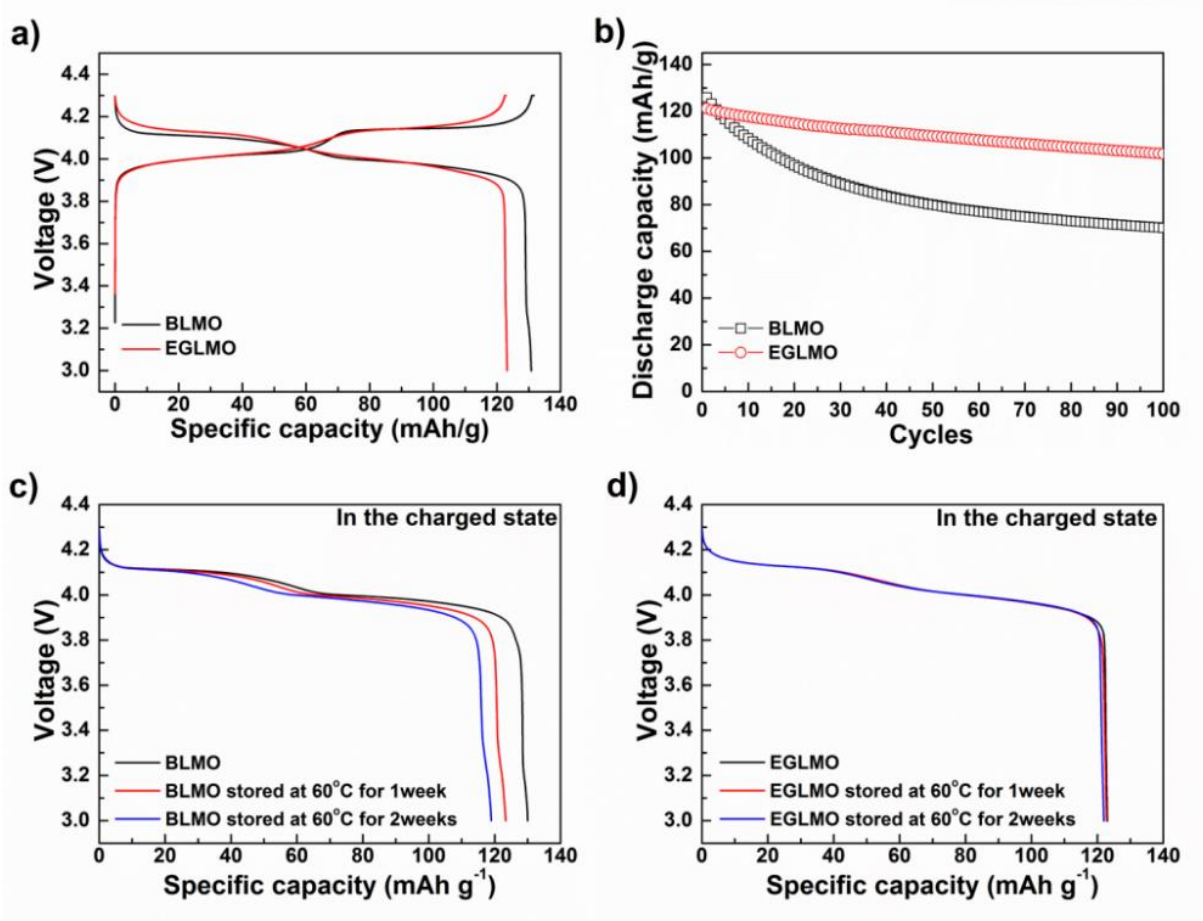

Figure 3.2.9. a) The first charge-discharge curves of BLMO and EGLMO at 0.1C rate at 24 ºC. b) Continuous cycling results of BLMO and EGLMO at 1C rate at 60 ºC. Discharge capacity variation of c) BLMO and d) EGLMO after stored in the charged state at 0.1C rate at 60 ºC.

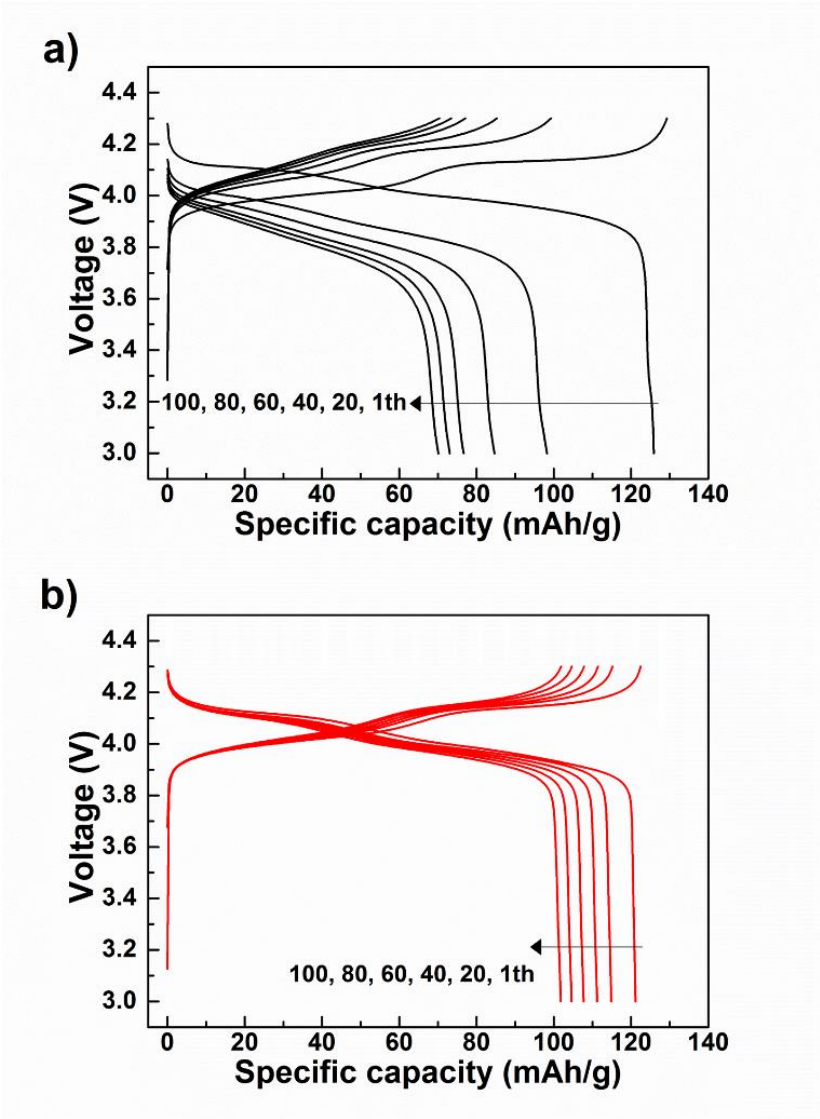

Figure 3.2.10. Charge and discharge profiles of a) BLMO and b) EGLMO at 60 °C after 1st, 20th, 40th, 60th, 80th, 100th cycles.

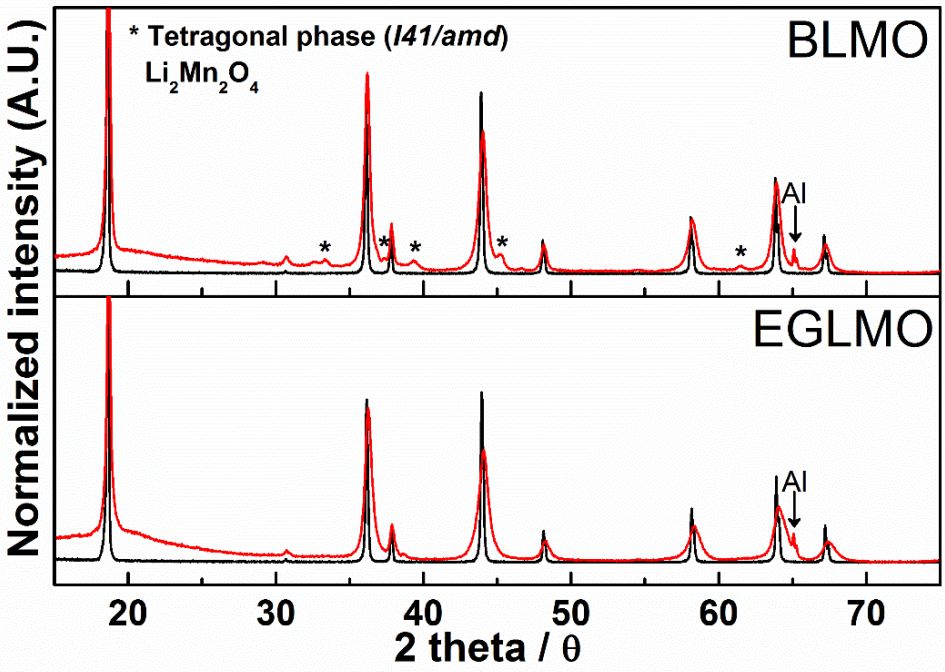

Figure 3.2.11. Ex-situ X-ray diffraction patterns of samples; as-prepared powders before cycling (black) and electrodes after 100 cycles at 60 ºC (red).

Figure 3.2.12a and b show the charge and discharge capacities of the BLMO and EGLMO as a function of various C rates from 0.5 C (65 mA g^{-1}) to 10 C (1300 mA g^{-1}) between 3.0 and 4.3 V at 24 ^{o}C. Either discharge or charge rate was fixed at 0.5 C rate. It is clearly shown that the rate capabilities of the EGLMO were much higher than that of the BLMO, especially at higher C-rates. For an example, the discharge capacity retention of the EGLMO electrode at 10 C rate was 74.2% (88 mAh g^{-1}) of its discharge capacity at 0.5 C rate, while that of the BLMO electrode delivered only 35.2% (41 mAh g^{-1}). Figure 3.2.12c and d show the discharge profiles of the BLMO and EGLMO as a function of temperature. With decreasing temperature, the EGLMO electrode exhibited much improved capacity retention relative to the BLMO. The capacity retention of the EGLMO and BLMO were 96% and 77% at -10 ^{o}C, 83% and 55% at -20 ^{o}C, respectively.

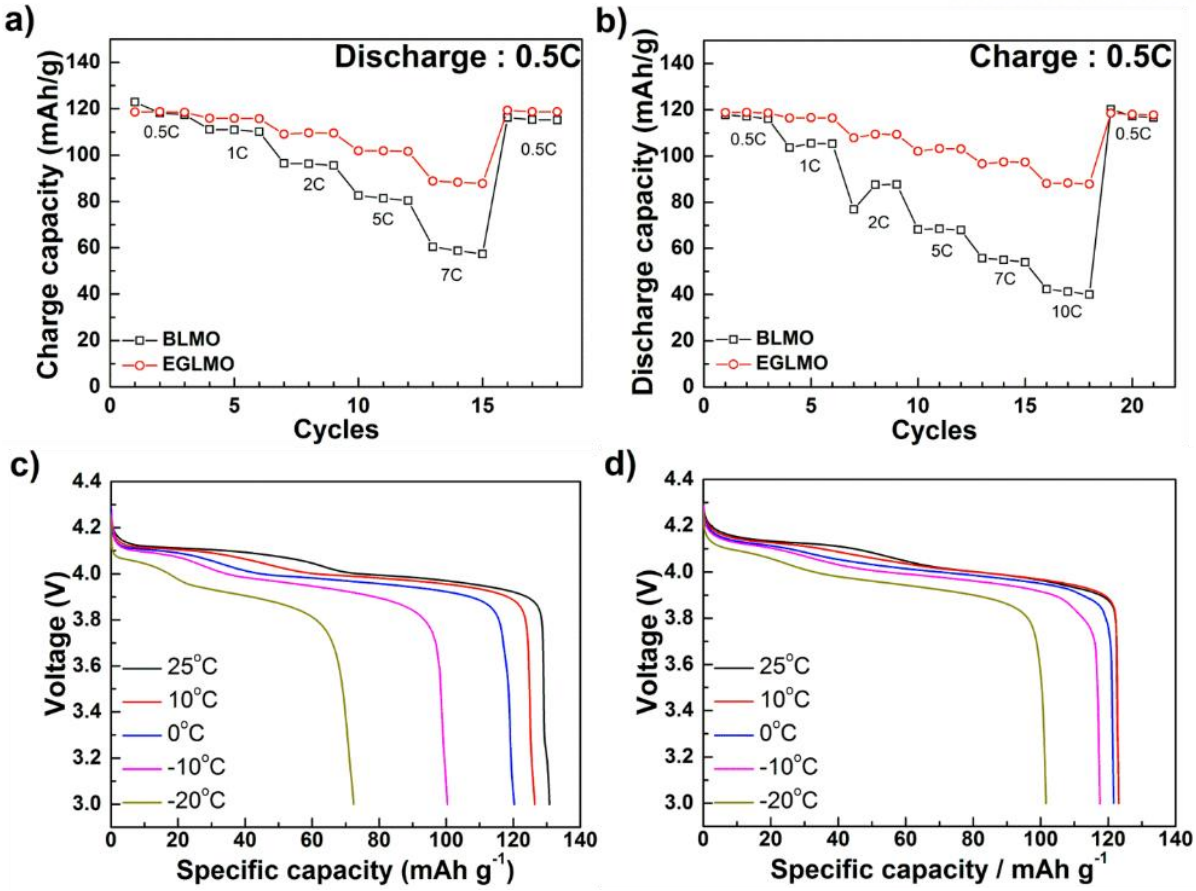

Figure 3.2.12. a) Charge and b) discharge capacity retention of BLMO and EGLMO as a function of various C rates from 0.5 C (65 mA g^{-1}) to 10 C (1300 mA g^{-1}) between 3.0 and 4.3 V at 24 °C. Discharge profiles of c) BLMO and d) EGLMO as a function of temperatures at 0.1 C rate.

In order to figure out the reasons why the EGLMO electrode presented higher rate capability and low temperature performance than the BLMO, we first performed an electrochemical impedance spectroscopy (EIS) which is a powerful technique of identifying the kinetics of Li ions in oxide cathodes. Figure 3.2.13a indicates the equivalent circuit of the impedance results with electronic resistance (R_e), surface film resistance (R_{sf}), two overlapped semicircles and Warburg impedance, and Figure 3.2.13b and c show typical Nyquist plots of the BLMO and EGLMO at different temperature from 25 ^oC to 0 ^oC. Even though it is very difficult to identify each of the above resistance value from the overlapped semicircles in the middle frequency region, it is obvious that the total impedance of the EGLMO is lower than that of the BLMO at any temperatures. Also the smaller circle of R_{sf} in the high frequency region supports that the side reactions were reduced in the present electrolyte on the surface due to the stable surface of the EGLMO.

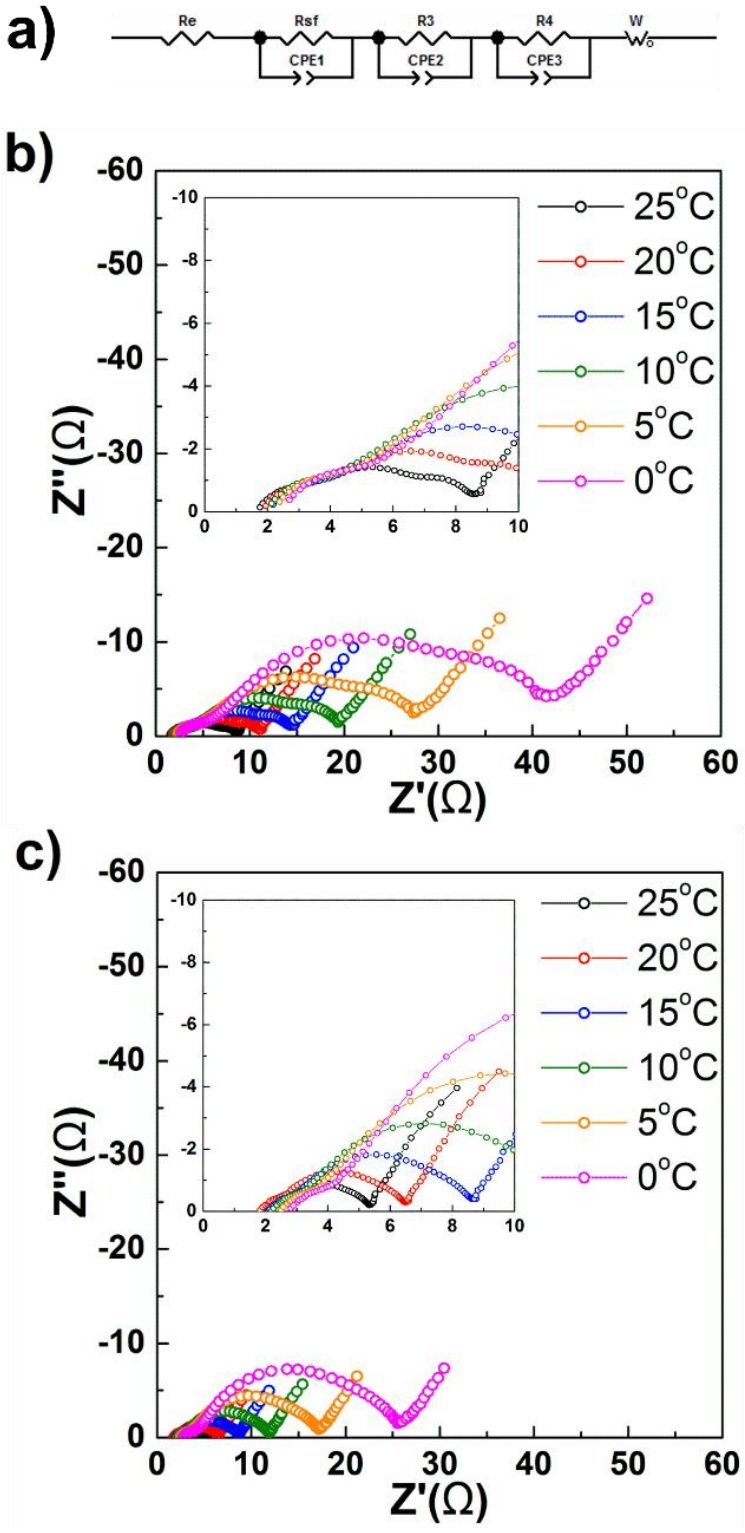

Figure 3.2.13. a) Equivalent circuit for the electrochemical impedance of BLMO and EGLMO. Nyquist plot for b) BLMO and c) EGLMO at different temperatures from 25 °C to 0 °C.

Secondly, we measured lithium diffusion coefficient which is an important kinetic parameter of intercalation materials and was determined by galvanostatic intermittent titration technique (GITT). [48] Before measurement, the cells were galvanostatically charged and discharged in two cycles at 0.1 C rate between 3.0 and 4.3 V at 24 °C. The GITT was employed at a constant current pulse of 13 mA g^{-1} (=0.1C rate) for 40 min, and then an open-circuit stands for 60 min to relax the cell voltage to the steady state. Based on GITT measurement and corresponding data calculation, the lithium diffusion coefficients as a function of the stoichiometry δ are presented in Figure 3.2.14a and b. During the charge and discharge process, the lithium diffusion coefficient of the BLMO was almost similar to that of the EGLMO in the region of $0.5 < \delta < 1.0$. However, it dramatically decreased at some specific stoichiometry δ ($0.05 < \delta < 0.4$ in charge process, $0.1 < \delta < 0.5$ in discharge process). In that stoichiometry region, the diffusivity of the EGLMO was much higher than that of the BLMO. Figure 3.2.14c shows an Arrhenius plots of the BLMO and EGLMO, respectively, indicating the temperature dependency for the lithium diffusion coefficient obtained from Warburg impedance in the low frequency region (Figure 3.2.13). [39, 49] The calculated activation energies of the BLMO and EGLMO were 50.7 kJ mol^{-1} and 34.3 kJ mol^{-1}, respectively. The improved kinetic parameters, lithium diffusion coefficient and activation energy, are related to the epitaxially grown surface of the layered phase. If the coating material only acts as a physical protection layer with defect, the lithium diffusion coefficient and activation energy should not be changed. The EGLMO has the stable surface which reduces the side reactions, and the surface phase is epitaxially connected to the host material without any defect, which provides the efficient path for lithium ion diffusion. Consequently, epitaxially grown nanoscale surface layer provides a chance for bare $LiMn_2O_4$ to show its innate properties not improved.

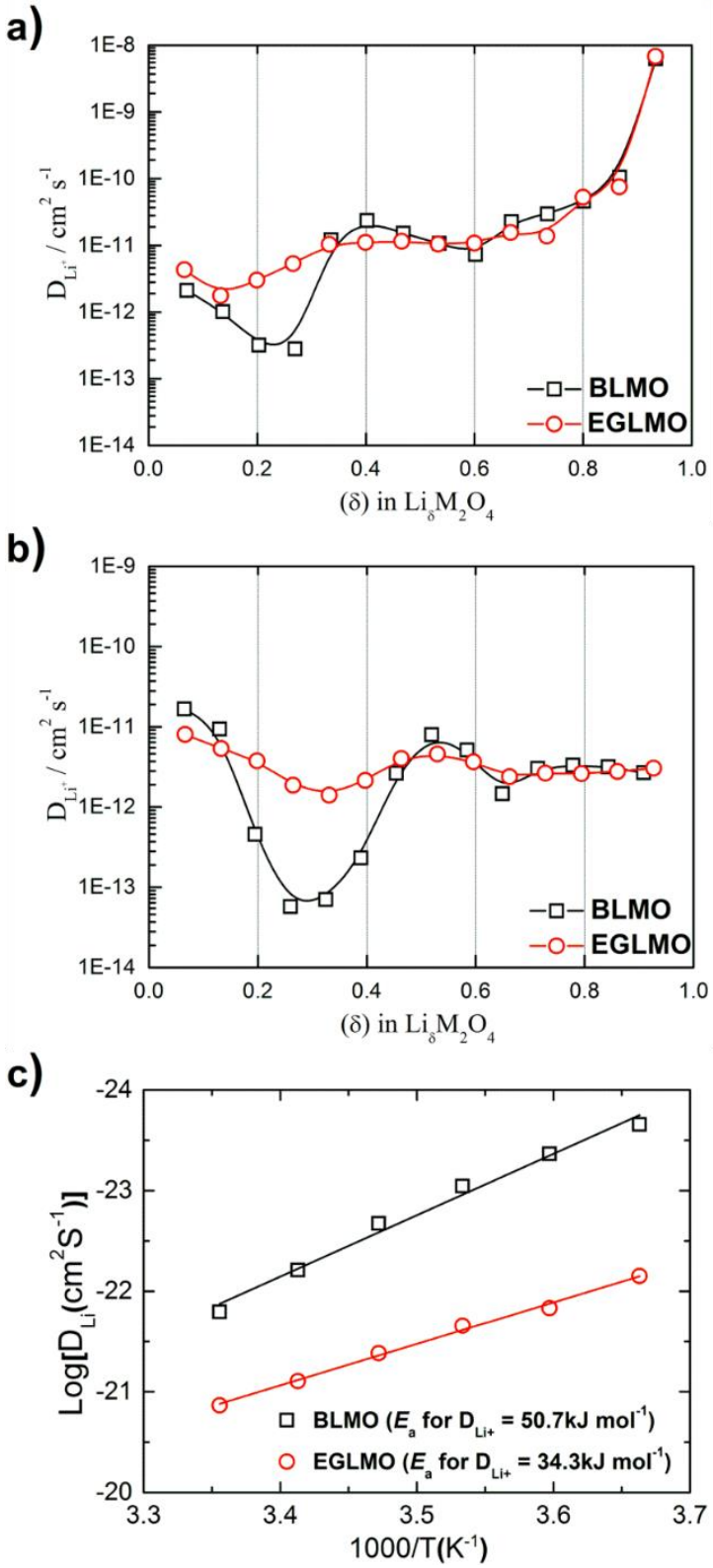

Figure 3.2.14. The lithium diffusion coefficients determined by the GITT curves as a function of the stoichiometry δ at current pulse of 13 mAg^{-1} during a) charge and b) discharge process. c) Arrhenius plots for lithium diffusion.

3. 2. 4. Conclusion

In summary, the hetero-structure $LiMn_2O_4$ that has the thin layered phase formed on the surface of the spinel bulk phase was synthesized. The coexistence of the layered structure ($R\bar{3}m$) and spinel structure ($Fd\bar{3}m$) without forming any defect was confirmed via STEM analysis. The newly developed material enhanced the cycle performance and thermal stabilities at the high temperature of 60 °C as well as improved the charge-discharge rate capability at various temperature ranges compared to those of the spinel $LiMn_2O_4$.

3. 3. Ultra-fast lithium ion insertion/extraction properties of spinel cathode material for Li-ion batteries.

3. 3. 1. Introduction

Lithium-ion batteries (LIBs) have been succeeded in small-sized battery markets since being used for portable devices due to the advantages of high energy density, low self-discharge rate and long cycle life. [5b, 19c, 50] Nowadays, the LIBs are considered to be the energy storage of choice for future electric vehicles (EVs). However, the EVs with present battery technology take several hours to fully charge the battery. Also, the driving range will be sharply reduced if the vehicle runs under severe conditions such as low temperature, a burst of speed, high velocity, and so on. Therefore, the battery with high power capability should be developed.

To meet the above requirements, 4V spinel cathode materials, $LiM_xMn_{2-x}O_4$ (M=Al, Mg, Co, Ni, etc.), have received significant attention as a cathode material of batteries for their use in electric vehicles (EVs) due to its advantages of high power properties, low cost, abundance, high safety and environmental friendly.[51] The spinel cathode materials (LMO) have a three-dimensional channel structure which is desirable for faster diffusion of lithium ion. Thus it offers fast charge and discharge properties compared to commonly used cathode materials such as layered $LiCoO_2$ etc. In order to strengthen the rate capability of spinel cathode materials, the nanostructured morphologies have been proposed. The nanosized materials have the advantages of shorter distance of lithium diffusion and larger surface area, facilitates faster electrochemical reaction and resulting in higher rate capability than microsized bulk materials.[33, 34d, 45, 52] However, it cannot fulfill high electrode density because of its larger surface-to-volume ratio. [36] Therefore, if the battery was manufactured by using the nanosized material, it should be bigger than that made by the microsized material in spite of their same cell capacity. The nanosized single particles agglomerated the microsized secondary particle may be a solution of electrode density issues. However, under high current operation, the electron transport from inner particle to the outermost surface should be delayed due to no conducting agent and large amount of grain boundary causing high overpotential.

Recently, as a solution of above drawbacks, our group reported carbon-coated spinel nanoparticle clusters. [36] The carbon layer was synthesized by sucrose carbonization. This concept acquired both advantages of nanosized and microsized materials: large surface area, short diffusion length and electrode density. Also the carbon coating layer provides facile electron pathway within the

secondary particle. This material affords fast lithium ion insertion/extraction resulting in significantly improved rate capability. However, the carbon coating by using organic compounds on the spinel cathode material is extremely difficult synthesis. For example, when the sucrose coated spinel $LiM_xMn_{2-x}O_4$ (M=Al, Mg, Co, Ni, etc.) was heated for carbonization in either air or oxygen atmosphere, the carbon preferentially takes oxygen from spinel lattice leading to the formation of oxygen defects (Figure 3.3.1) because the solid phase has higher oxygen concentration than the gas phase. Surely, it is impossible that spinel materials stay in inert or reduction atmosphere without oxygen release. Therefore, practically possible synthesis method toward high rate capability should be proposed as an alternative approach of carbon coating.

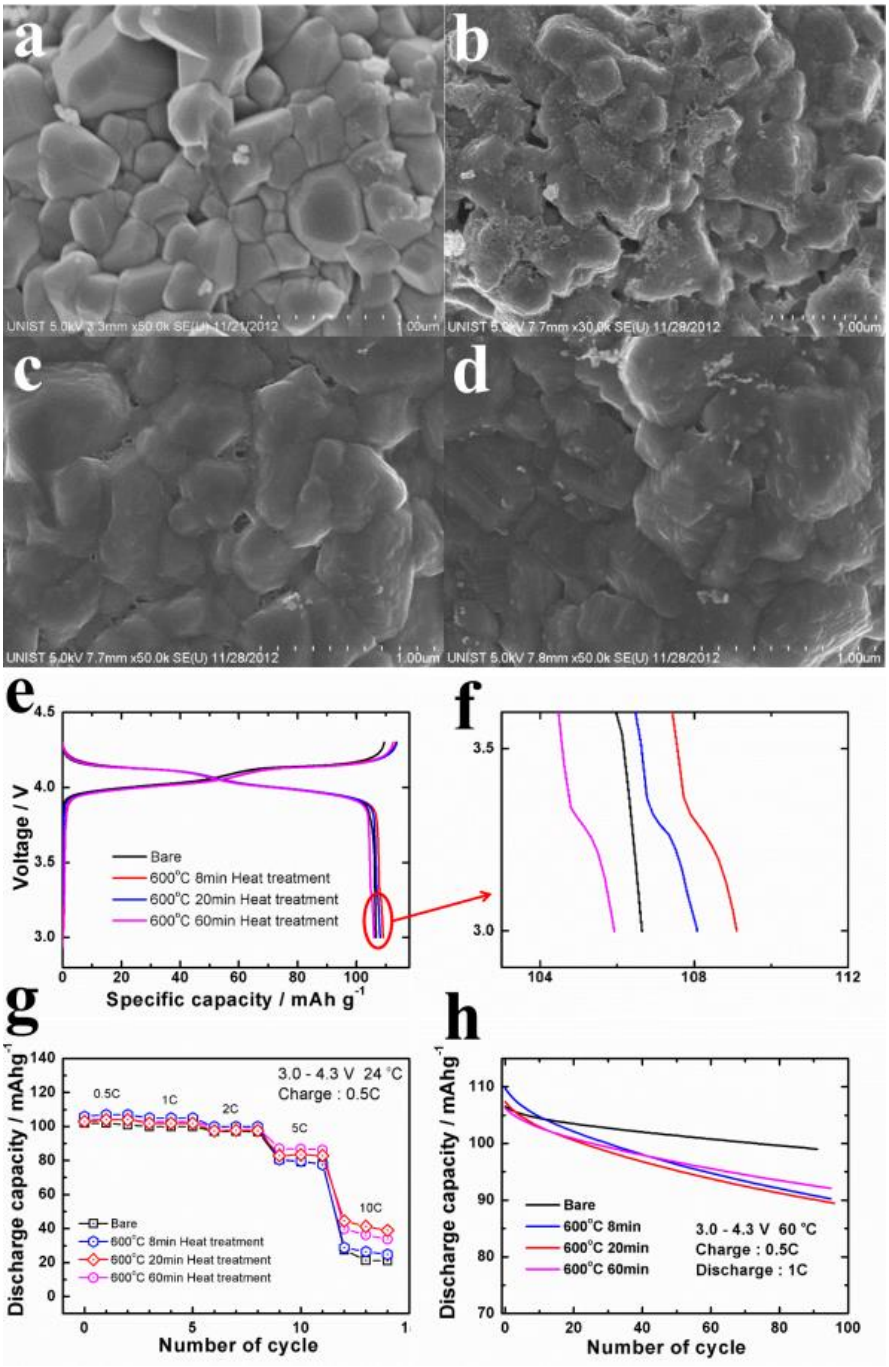

Figure 3.3.1. The carbon coating on the spinel cathode material was carried out by using sucrose-carbonization method. The coating amount of sucrose was 10 wt%. SEM images of a) bare b) heated at 600 °C for 8min after sucrose coating, c) 20min and d) 60min. As can be seen in formation profiles e) and f), the plateau related to oxygen deficiency between 3.2 and 3.4V can be found. g) The carbon layers can help increase rate capability. However, h) the cycling performance became worse than bare electrode due to structural instability.

Herein, we report a new concept of composites with super-p and nanosized spinel material (Denoted as nanosized LMO) (Figure 3.3.2). The nanosized single particles obtained by ball-milling and the acid-treated super-p were reassembled by spray-drying method resulting in the synthesis of 7~40 ㎛-sized secondary particles. This large particle ensured the high electrode density. Also the acid-treat super-p whose surface was changed from hydrophobic to hydrophilic by nitric acid can be well mixed with nanosized spinel particles in water. Therefore, the super-p can be properly distributed in a secondary particle after spray drying to form spherical secondary particle, which can provide facile electron pathway when high current loaded. The developed material showed extremely high charge and discharge rate capability even at low temperature resulting from reduced polarization.

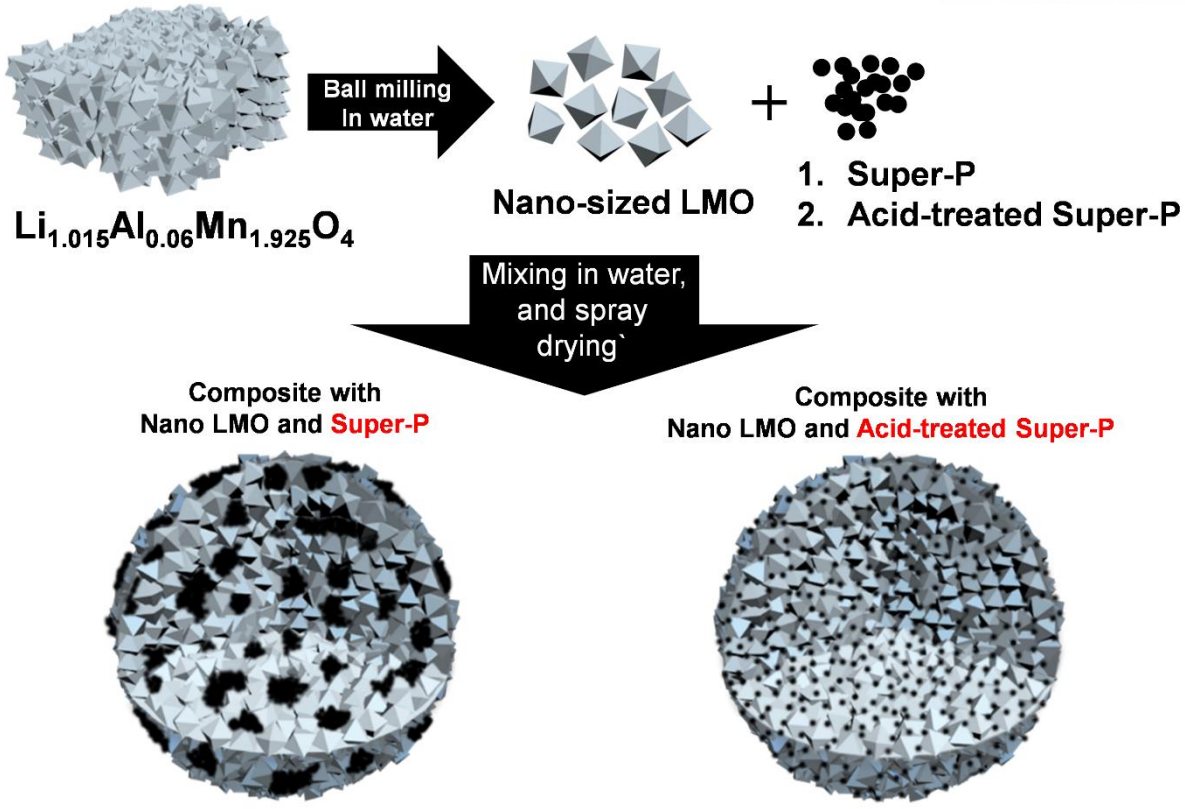

Figure 3.3.2. Schematic diagram of synthesis process and composite samples with nanosized spinel and two kinds of super-p.

3.3.2 Experimental Section

The Bare $Li_{1.015}Al_{0.06}Mn_{1.925}O_4$ powder was synthesized via a typical sol-gel reaction and further heat treatment. A desired amount of $Li(CH_3COO) \cdot 2H_2O$, $Al(NO_3)_3 \cdot 9H_2O$, and $Mn(CH_3COO)_2 \cdot 4H_2O$ was dissolved in distilled water with equivalent amount of citric acid as a chelating agent. The aqueous solution was concentrated to produce sols and then dried at 100 °C. The dried sample was heated at 400 °C for 5h and then thoroughly mixed. The mixed powder was calcined at 770 °C for 10h to obtain the bare spinel material. The nanosized spinel powder was prepared by ball-milling for 10h. The acid treatment on super-P was carried out with 40ml of 0.05 M nitric acid solution and 2 g of super-P. The mixture was stirred for 12 h, then filtered and washed several times to remove nitric acid. The obtained super-p was dried at 150 °C for 24 h. By using nanosized spinel powder and two kinds of super-p, the composite samples were prepared by spray drying process at 160 °C, then the dried powders were heated at 300 °C in inert atmosphere to eliminate residual moisture.

The crystalline structures were confirmed by powder X-ray diffractometer (XRD, D/MAX-2200 V, Rigaku) using Cu Ka radiation at 2θ = 10 °-80 °. The morphologies of three samples were checked by using scanning electron microscopy (SEM, S-4800, HITACHI).

The cathode electrodes were composed of cathode materials, super-p and polyvinylidene fluoride as a binder (80:10:10 for composite electrodes and 72:18:10 for bare electrode, weight ratio). The galvanostatic charge-discharge cycling was performed by using CR2032 coin-type cell, which consisted of a cathode electrode and a lithium metal as an anode separated by the porous polypropylene film. Coin-type cells were assembled in an argon-filled glove box and 1.15M $LiPF_6$ in ethylene carbonate/dimethyl carbonate/diethyl carbonate (3/4/3 vol.% Panax Staryle) was used as an electrolyte. Before electrochemical tests, the cells were galvanostatically charged to 4.5 V at 0.1 C rate, and kept at 4.5 V until the current decreased to 0.02 C rate, then discharged to 3.0 V vs Li/Li^+. The active material loading was 1 mg cm^{-2}. The gravimetric capacities were calculated based on the weight of spinel materials. The electrochemical impedance spectroscopy (EIS, IVIUM) was carried out to check impedance from 0.05 to 250 kHZ frequency range on coin-type half cells at SOC 100% in temperature bath. The obtained results were analyzed by using ZView software.

3.3.3 Result and discussions

The morphologies of samples, bare $Li_{1.015}Al_{0.06}Mn_{1.925}O_4$ (Denoted as BLMO), composite with super-p and nanosized particles (Denoted as CSLMO) and composite with acid-treated super-p and nanosized particles (Denoted as CASLMO) were confirmed by scanning electron microscopy (SEM). The BLMO synthesized by sol-gel reaction and further heat treatment resulted in irregular morphology (Figure 3.3.3a and b). After ball-milling, the nanosized single particles could be obtained (Figure 3.3.3c). By using this powder, two kinds of samples were synthesized. As can be seen, the CSLMO has a spherical morphology of 8-20 ㎛ sized secondary particle where the super-p and nanosized LMO coexisted in a particle (Figure 3.3.3d-f). However, it was confirmed that the nanosized LMO and super-p were not well mixed. On the other hand, in the case of CASLMO, it looks denser than CSLMO, and nanosized LMO and super-p were evenly distributed in secondary particle (Figure 3.3.3g-i). These results of super-p distribution were matched with the energy dispersed X-ray analysis (Figure 3.3.4). As can be seen, there are some regions of red dots with higher concentration in a CSLMO particle, which are consistent with the agglomerated super-p (Figure 3.3.4a) On the other hand, in the case of CASLMO, the carbon elements are evenly distributed throughout the secondary particle (Figure 3.3.4b). It is believed that better distribution of super-P for CASLMO will provide more efficient electron pathway. Also the pellet densities of BLMO, CSLMO and CASLMO were 2.6 g/cc, 2.33 g/cc and 2.41 g/cc, respectively. The slightly reduced pellet densities were attributed to the volume of super-p in secondary particles. The crystal structures of samples were identified by XRD analysis (Figure 3.3.5a). The patterns of three samples exhibited a well-defined cubic spinel phase of space group $Fd\bar{3}m$ without any discernible impurity peaks, which means there is no phase transition during synthesis process. The thermal gravimetric analysis (TGA) was carried out to confirm the amount of super-p. The rate of increasing temperature is 5 $^{o}C\ min^{-1}$. As can be seen in Figure xx, the content of super-p was 10 wt% as designed. (Figure 3.3.5b)

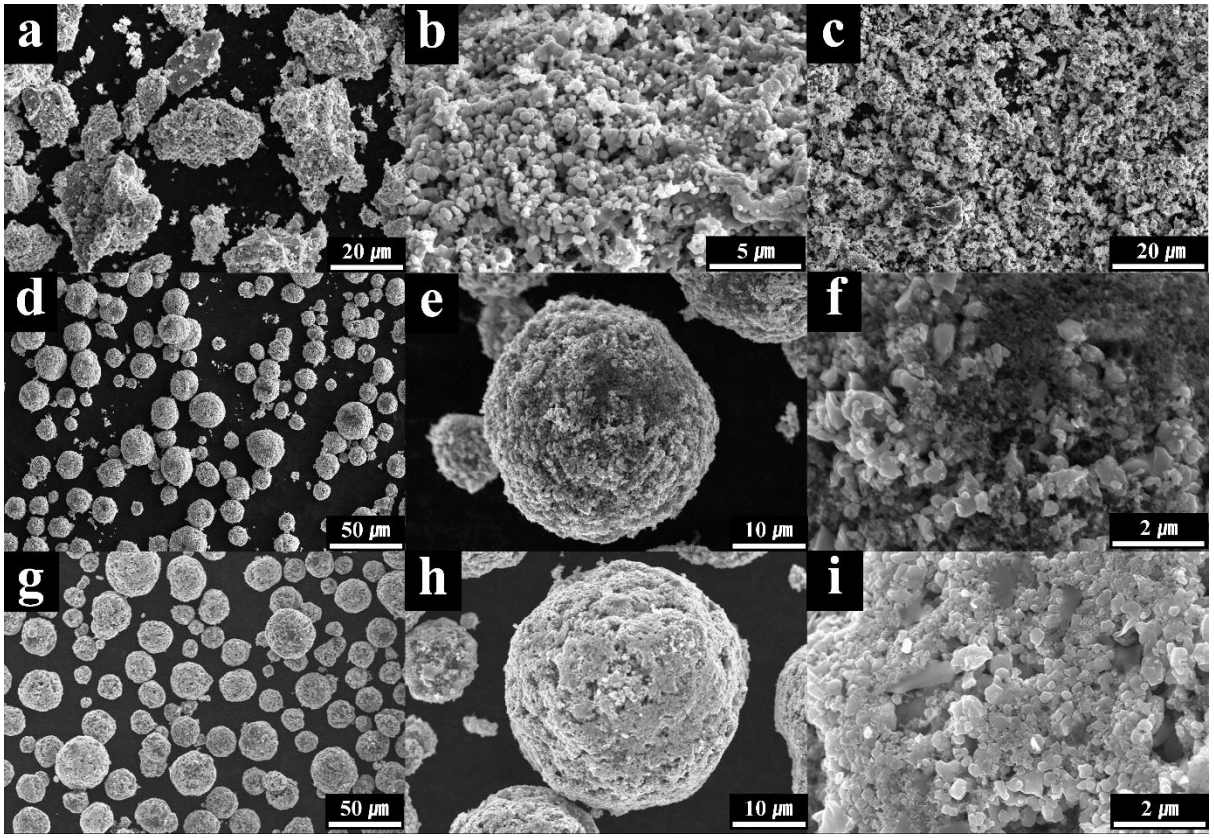

Figure 3.3.3. SEM images of (a) BLMO, (b) magnified image of (a), (c) BLMO after ball-milling, (d) CSLMO, (e and f) magnified images of (d), (g) CASLMO, and (h and i) magnified images of (g).

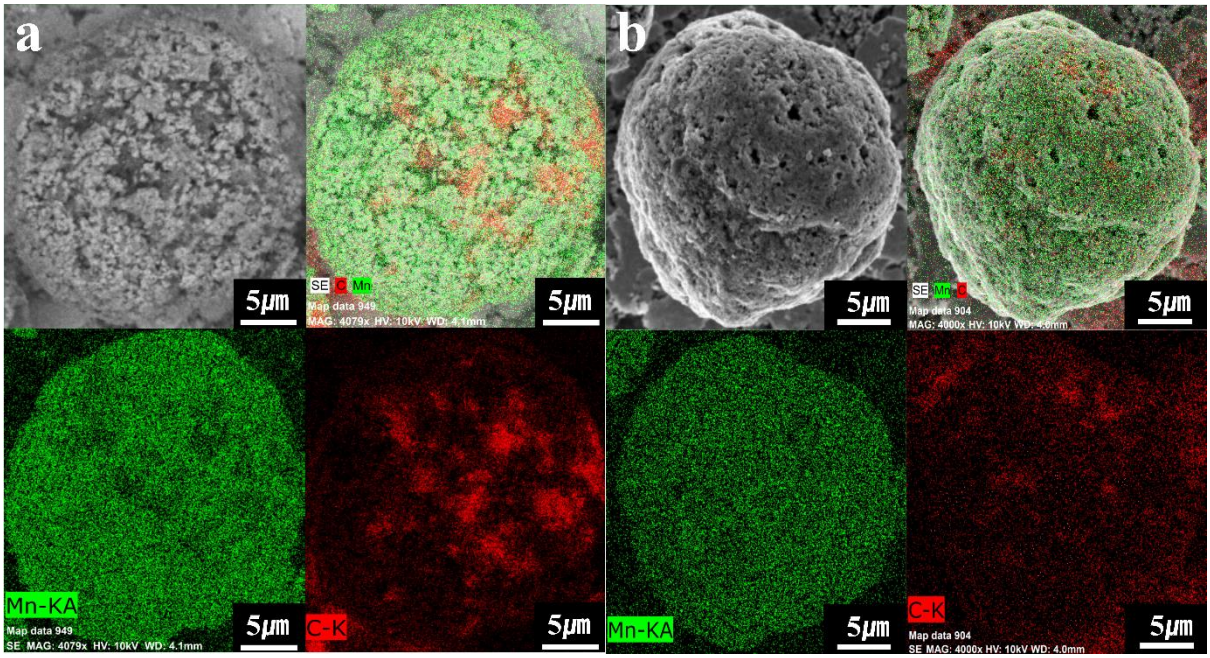

Figure 3.3.4. Energy dispersed X-ray mapping analysis of manganese and carbon of (a) CSLMO and (b) CASLMO.

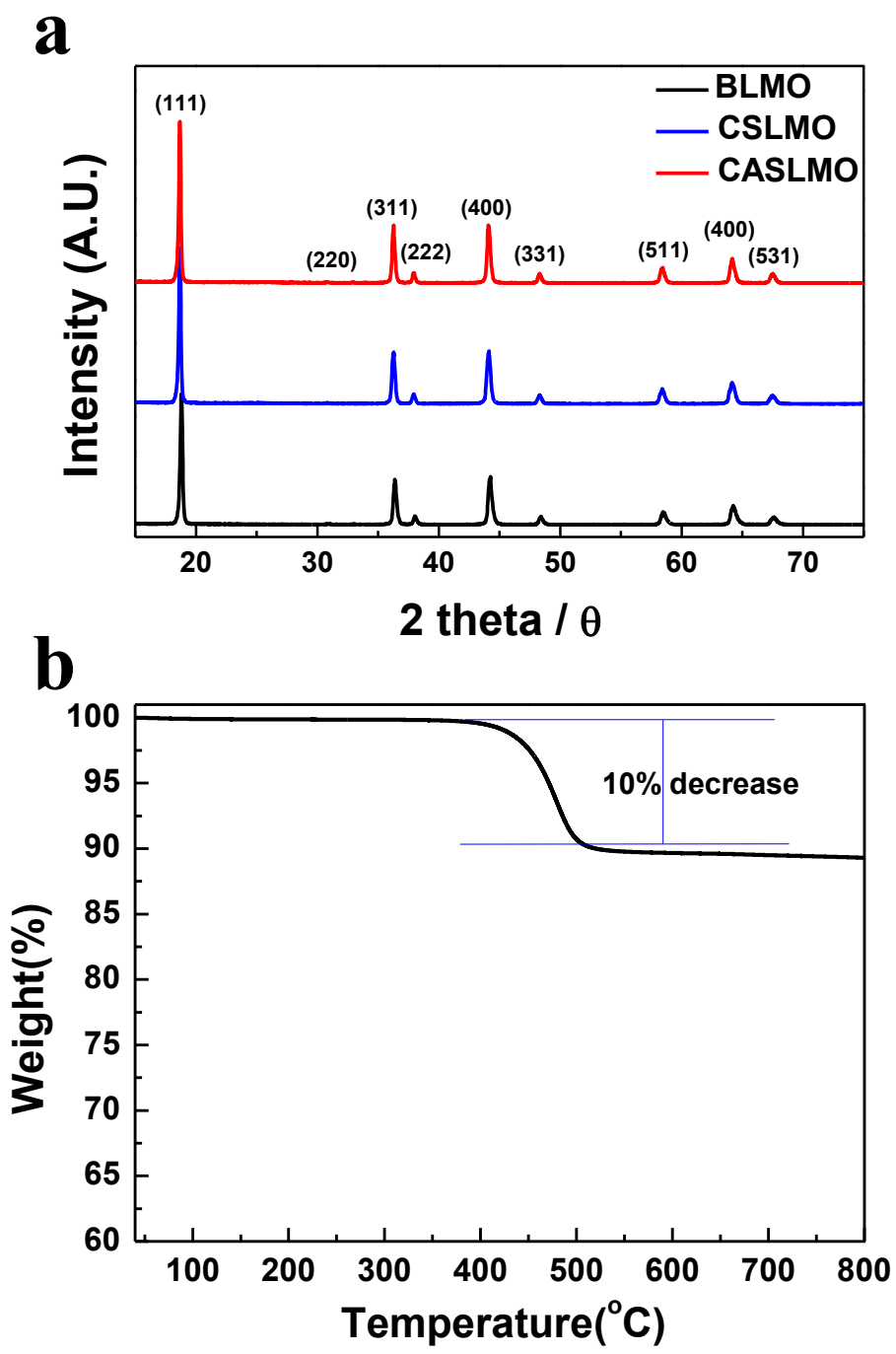

Figure 3.3.5. (a) Powder XRD patterns of BLMO, CSLMO and CASLMO. (b) TGA results of CASLMO with scan rate of 5 ^{o}C min^{-1}.

The electrochemical test of three electrodes were performed by coin-type half cells. The 1 C rate was fixed to 120 mA g^{-1}. Figure 3.3.6a exhibits the first charge and discharge curves of the BLMO, CSLMO and CASLMO between 3.0 and 4.5 V at 0.1C rate (12 mA g^{-1}) at 24 ^{o}C. The bare electrode delivered 117.1 mAh g^{-1}, while the CSLMO and CASLMO showed slightly higher capacities of 120.5 mAh g^{-1} and 120.5 mAh g^{-1}, respectively. It can be explained by reduced overpotential. In Figure 3.3.6b, it can be known that the charge capacity of BLMO from constant voltage (CV) mode was larger than those of composite samples (CSLMO and CASLMO). The difference with the measured and real voltage is polarization and its value can be defined as an overpotential. The loss of capacity due to polarization can be achieved by using CV mode at the end of charge. The large amount of capacity at CV mode is consistent with the large overpotential. From this results, we can know that the composite electrodes has significantly reduced overpotential compared to BLMO.

Figure 3.3.7 exhibits the charge capacities as a function of various C rates from 0.5 C (60 mA g^{-1}) to 300 C (36 A g^{-1}) between 3.0 and 4.5 V at 24 ^{o}C. The discharge current was fixed at 0.5 C rate. As can be seen in Figure 3.3.7a, the three electrodes showed similar charge capacities at 0.5 C. The capacity of BLMO dramatically decreased as increasing charging current because there is no conducting agent in secondary particles. It caused large amount of resistance at the electron transfer through grain boundary. However, the composite electrodes had much improved fast charging properties. The CSLMO and CASLMO had comparable capacity retentions until 10 C rate, whereas the charge rate capability of CASLMO was higher than that of CSLMO at higher C rate (> 10 C). The CSLMO has worse distribution of conducting agent in secondary particles. Some regions have higher concentration of super-p and others do not (Figure 3.3.4). When low current loaded, the amount of super-p surrounding nanosized LMO in low concentration region was enough to conduct certain amount of electrons, thus showing similar performance to CASLMO. However, the poor distribution of super-p provided insufficient electron pathway under higher current application leading to high overpotential, thus presenting worse charge rate capability. Consequently, the well distributed conducting agent acted a key role to electron conducting, therefore, the CASLMO showed the outstanding charge rate capability. For example, a cycle at 100 C rate takes only 26 seconds with the cell retaining 73% of its initial capacity. The discharge rate capabilities was also investigated by maintaining the charge rate of 0.5 C in the applied discharge current range between 0.5 C (60 mA g^{-1}) and 1000 C (120 A g^{-1}) (Figure 3.3.8). The results indicated similar trend to charge rate capability. The CASLMO presented the best discharge rate capability among three electrodes. It retained 98.8% at 10 C and 77.8 % at 500 C compared to its capacity at 0.5 C, while the BLMO and CSLMO showed worse capacity retention of 86.8% and 98.0 % at 10C, and 2.2% and 16.6% at 500 C, respectively. Also the CASLMO showed significant improvement in low temperature performance (Figure 3.3.9). At -10 ^{o}C, it exhibited superior capacity retention

compared to BLMO and CSLMO from 0.5 C rate to 200 C rate. Many factors could affect the battery performance at low temperature (< 0 ºC). The viscosity of electrolyte increases resulting in low ionic conductivity, thus, the kinetics of electrochemical cell will be deteriorated.[53] Also the charge delivery hinders leading to increasing the charge transfer and ohmic resistances.[54] Therefore, the efficient structure for facile electron pathway of CASLMO facilitated the charge delivery to the surface of material resulting in the faster charge transfer reaction. Consequently, the CASLMO showed faster kinetic properties than CSLMO and BLMO at -10 ºC.

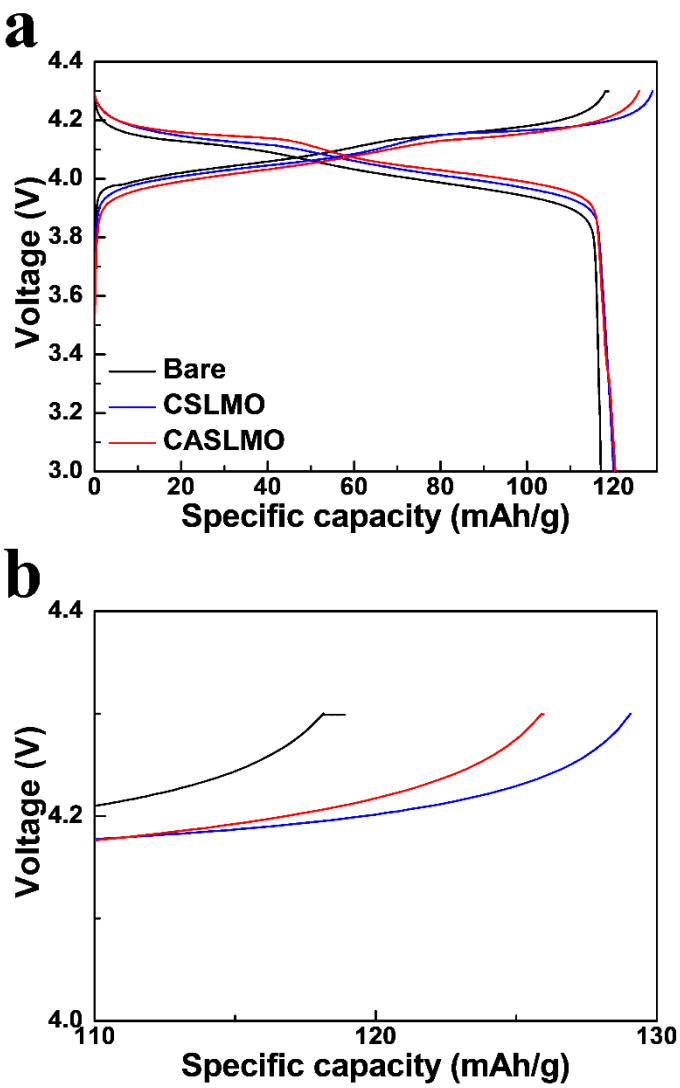

Figure 3.3.6. (a) First charge-discharge curves of BLMO, CSLMO and CASLMO at 0.1 C rate (12 mA g^{-1}) at 24 ^{o}C. (b) Expended image of (a).

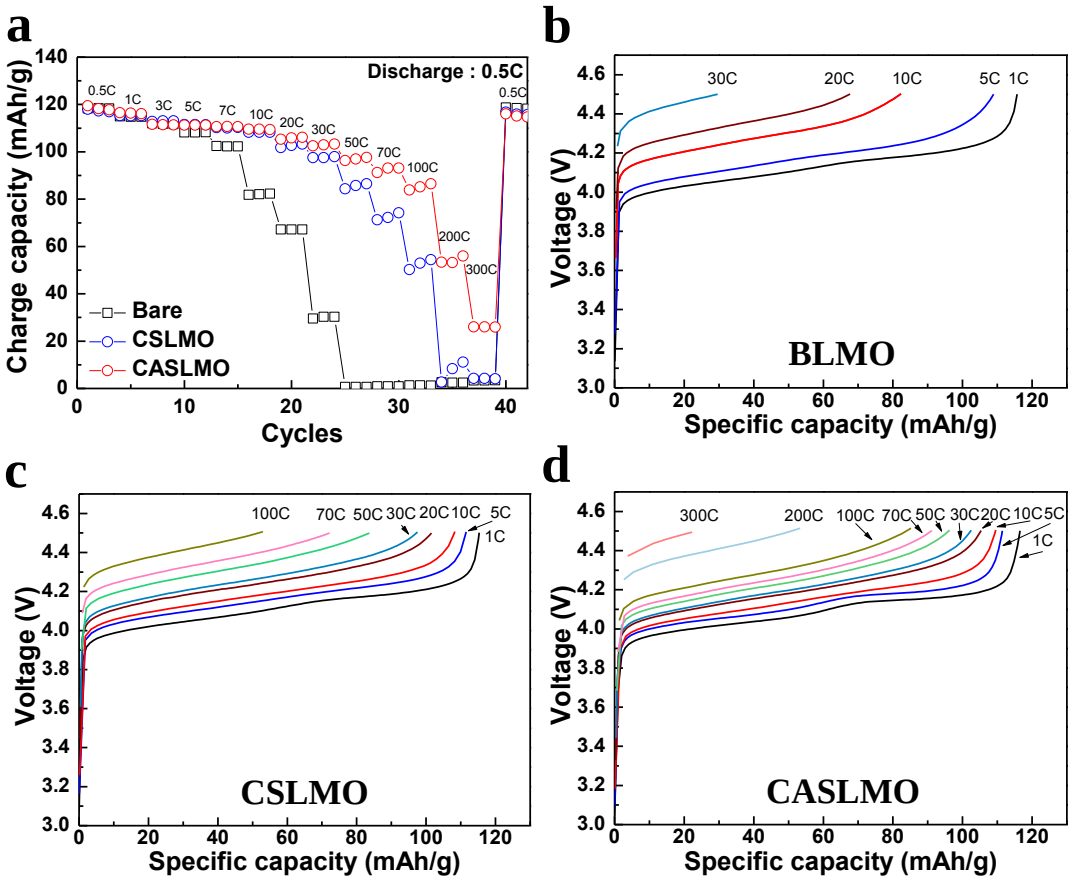

Figure 3.3.7. (a) Charge capacity retention of three electrode as a function of various from 0.5 C (60 mA g^{-1}) to 300 C (36 A g^{-1}) between 3.0 and 4.5 V at 24 ºC. The discharge current was fixed at 0.5 C. Charge voltage profiles of (b) BLMO, (c) CSLMO, and (d) CASLMO.

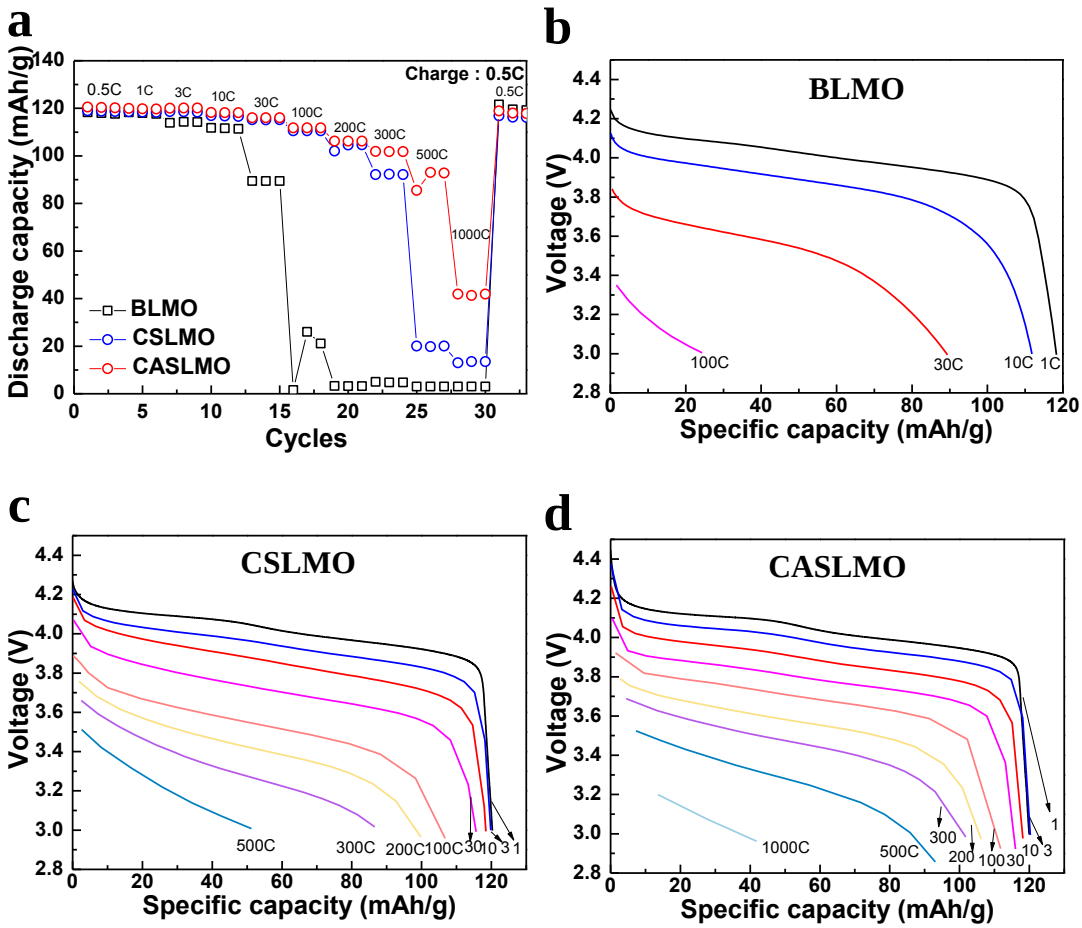

Figure 3.3.8. (a) Discharge capacity retention of three electrode as a function of various from 0.5 C (60 mA g^{-1}) to 1000 C (120 A g^{-1}) between 3.0 and 4.5 V at 24 ºC. The charge current was fixed at 0.5 C. Discharge voltage profiles of (b) BLMO, (c) CSLMO, and (d) CASLMO.

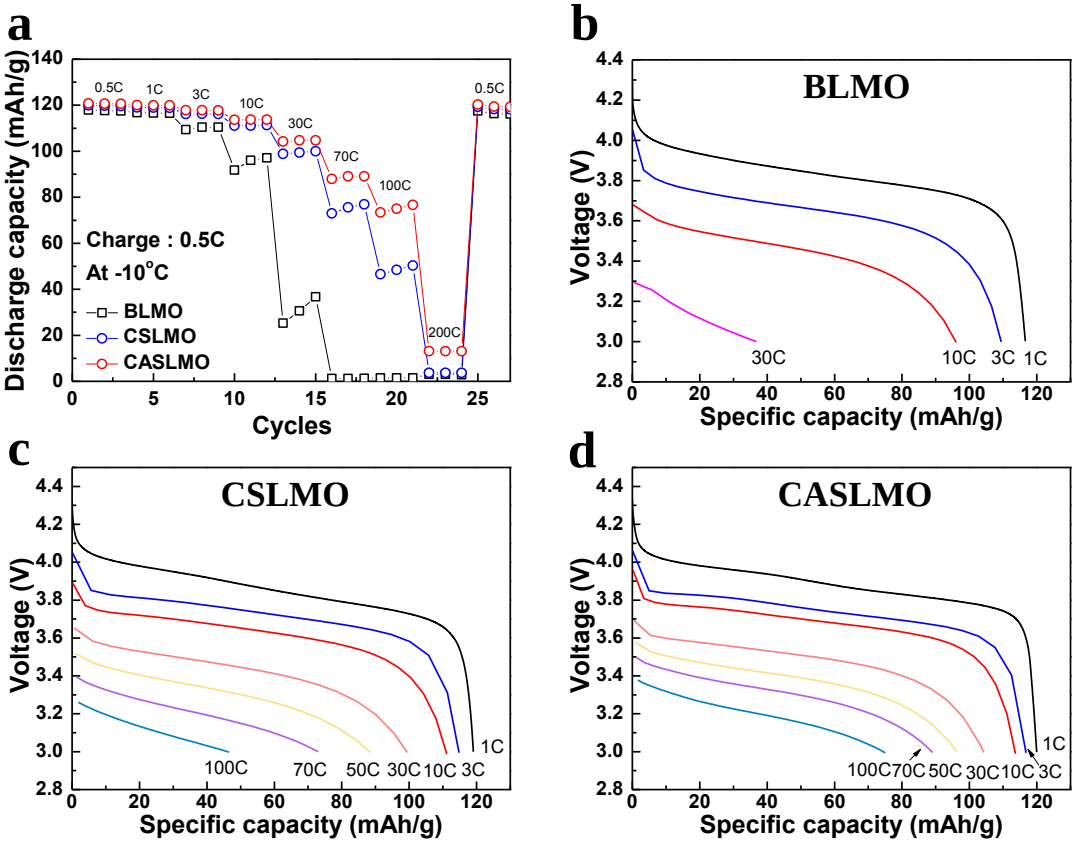

Figure 3.3.9. (a) Discharge capacity retention of three electrode as a function of various from 0.5 C (60 mA g^{-1}) to 200 C (24 A g^{-1}) between 3.0 and 4.5 V at -10 ºC. The charge current was fixed at 0.5 C. Discharge voltage profiles of (b) BLMO, (c) CSLMO, and (d) CASLMO.

Figure 3.3.10a-c show the electrochemical impedance results of BLMO, CSLMO and CASLMO as a function of temperature from 25 ºC to 5 ºC. The cell was charged at 5 C at SOC 100%. As can be seen, with decrease in temperatures, total impedances of three electrode steeply increased. The BLMO electrode showed slightly lower impedance than composite electrodes, whereas it exhibited much highest values at the lower temperatures. Also the impedance of CASLMO presented slightly lower than that of CSLMO. The activation energies (Ea) for charge transfer were calculated from temperature dependencies of EIS results by using Arrhenius equation which is described below

$$k = \mathrm{A} \cdot exp\left(-\frac{Ea}{RT}\right)$$

(k= rate constant of reaction, A is pre-exponential factor, R is gas constant, and T is absolute temperature.)

The activation energies for charge-transfer reaction are given in Figure 3.3.8d. The values of BLMO, CSLMO and CASLMO were 68.1, 55.7 and 51.9 kJ mol^{-1}, respectively. The one of factor of rate capability is the charge transfer reaction. The lower activation barrier indicates a higher charge transfer reaction kinetics in CASLMO.

The higher rate capability depends on the polarization as well as the charge transfer reaction. The polarizations of three electrode were measured by means of galvanostatic intermittent titration technique (GITT). The constant current of 3 C rate (360 mA g^{-1}) for 90 seconds and rest for 60 min to relax the cell voltage were alternately applied for GITT measurement during charge and discharge (Figure 3.3.11a and b). As can be seen in Figure 3.3.11c-f, the composite electrodes showed much lower overpotential throughout the entire state of charge (SOC) and depth of discharge (DOD). Also the polarization of CASLMO is smaller than that of CSLMO. The electrodes and materials which are used for battery are not ideal. The large size particle with polycrystalline structure has a lot of grain boundary. So the electron conduction from inside of particle takes relative longer time than outside. Also the sufficient amount of conductive agent is not added in electrode due to concern for decreasing cell capacity even though it is known that larger amount of conductive carbon results in higher rate capability. Hence, the rate determined step for fast charge and discharge may be the electron delivery. When the relatively high currents are applied, the lithium ions that are not reacted may be accumulated on the surface of electrode material because the lower kinetics of electrons from current collector and materials. As a result, the concentration gradient appears between the surface of material and inside of material. During the rest time after constant current pulse applied in GITT test, the concentration gradient will be reduced by accepting electrons until reaching equilibrium state, which leads to decreasing (charge) and

increasing (discharge) voltages (Figure 3.3.11 g and h). The CASLMO took the shortest time to be equilibrium state among three electrodes because of the facile electron pathway. Consequently, the lowest activation energy for charge transfer reaction and the smallest polarization of CASLMO during charge and discharge are ascribed to the best rate capability during three electrode.

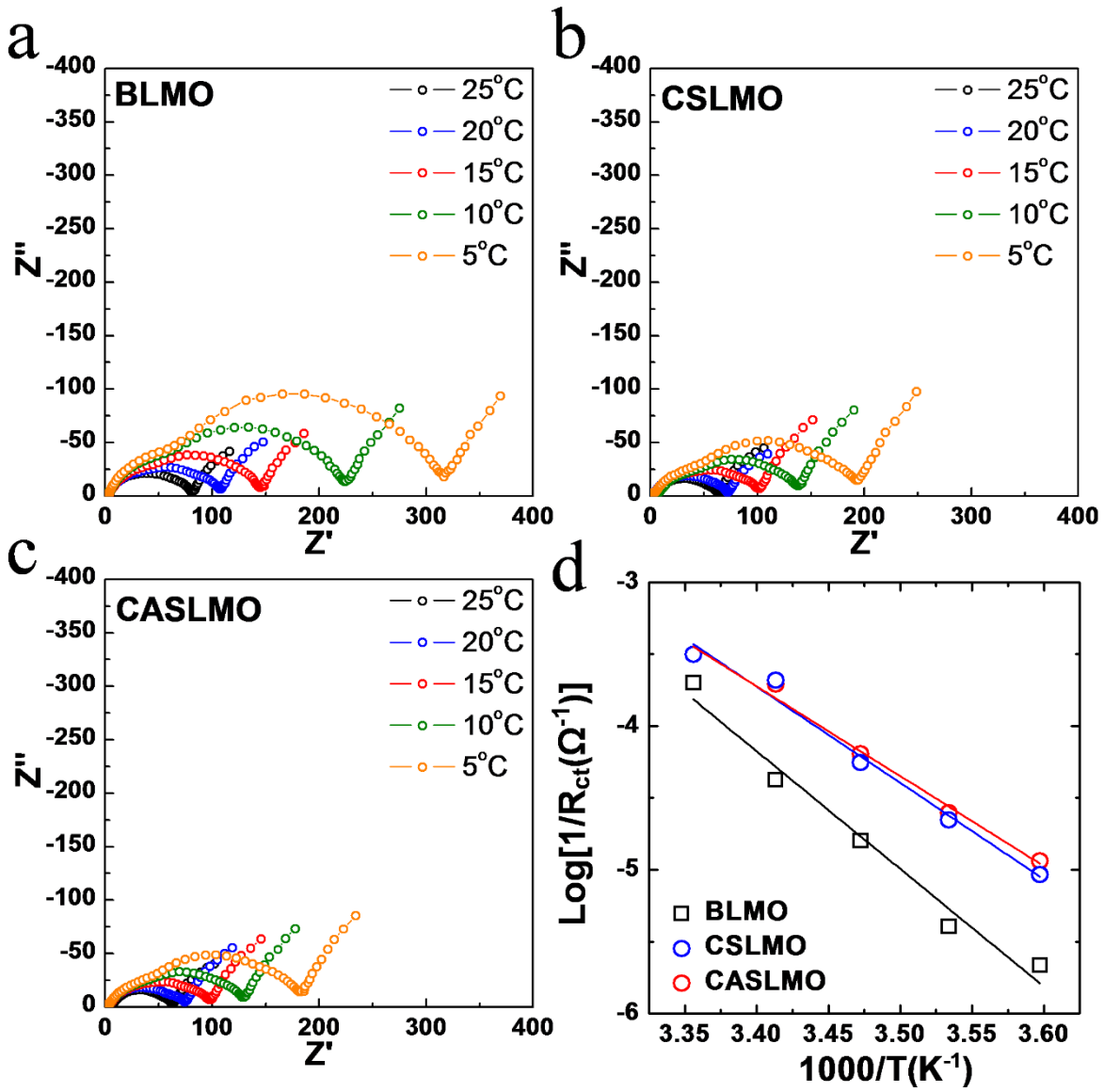

Figure 3.3.10. Nyquist plot of (a) BLMO, (b) CSLMO and (c) CALMO as a function of temperatures from 25 ºC to 5 ºC. (d) Arrhenius plots of the charge-transfer reaction for BLMO, CSLMO and CASLMO.

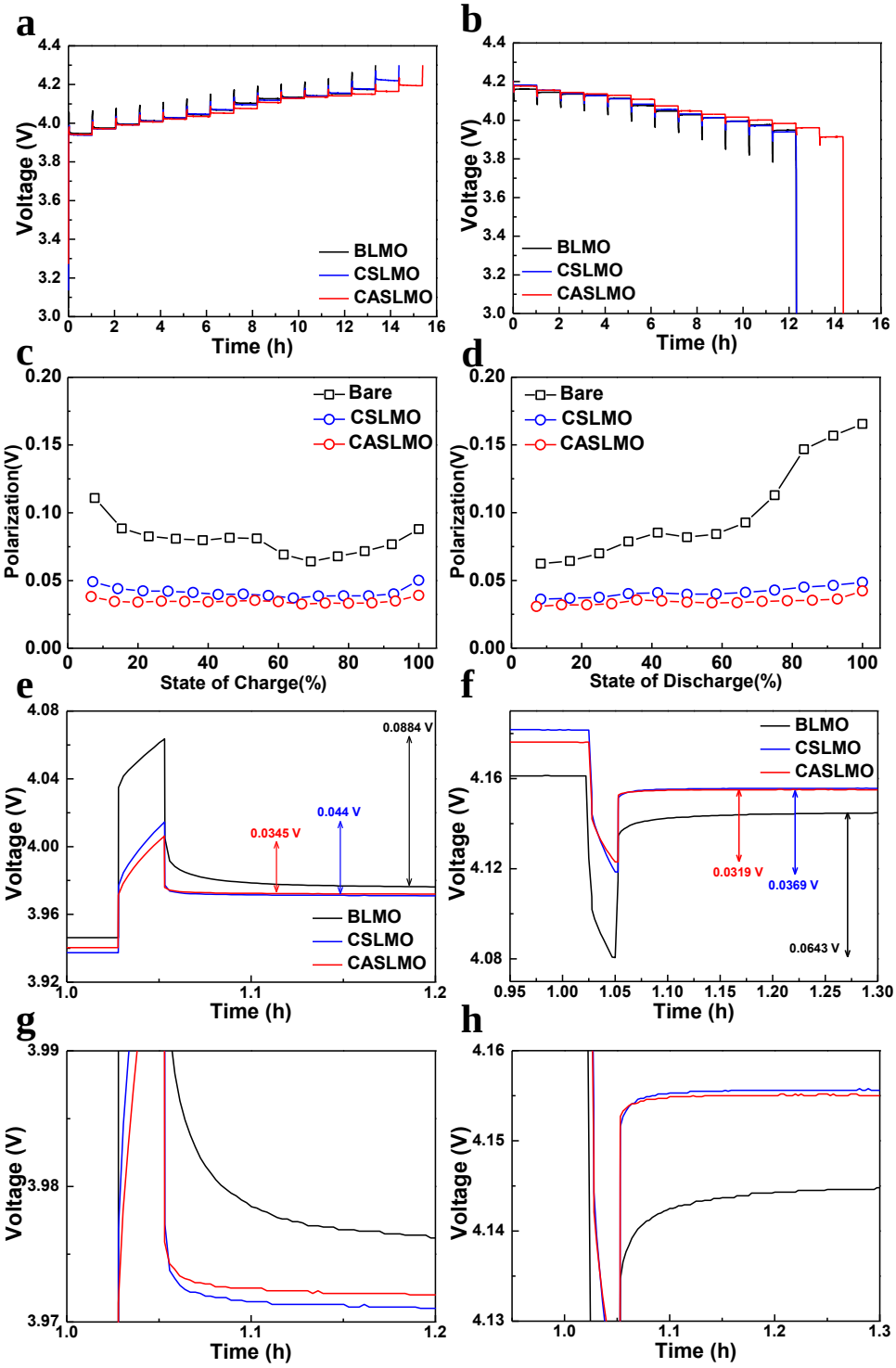

Figure 3.3.11. GITT potential response during (a) charge and (b) discharge. Polarization of BLMO, CSLMO and CASLMO during (c) charge and (d) discharge. (e and f) expended images of the regions in (a and b), respectively. (g and h) expended images of the regions in (e and f), respectively.

3. 2. 4. Conclusion

In, summary, we successfully synthesized microsized composite secondary particles consisting of super-p and nanosized spinel with minimizing the loss of electrode density. The acid treatment was carried out to change the state of surface from hydrophobic to hydrophilic, thus, super-p could be evenly distributed in a secondary particle when the water based solution was spray-dried, which was obviously observed by EDX analysis. As a result, the well mixed acid-treated super-p can provide more facile charge delivery compare to bare and composite with normal super-p. The newly developed material showed outstanding lithium ions insertion/extraction properties at -10 ^{o}C as well as 24 ^{o}C. The reasons are attributed to: 1) fast lithium ion diffusion in solid state due to nanosized primary particles, 2) lower activation energy for charge transfer reaction owing to facile electron pathway, and 3) low polarization during charge and discharge due to 1) and 2). We believe that this concept could provide a direct path to improving battery performances leading to commercialization of high performance electric vehicles.

4. References

1. Reimers, J. N.; Dahn, J. R., Electrochemical and In Situ X-Ray Diffraction Studies of Lithium Intercalation in Li x CoO2. *Journal of The Electrochemical Society* **1992,** *139* (8), 2091-2097.

2. Ohzuku, T.; Ueda, A., Solid-State Redox Reactions of LiCoO2 (R$\bar{3}$m) for 4 Volt Secondary Lithium Cells. *Journal of The Electrochemical Society* **1994,** *141* (11), 2972-2977.

3. (a) Cho, J.; Kim, Y. J.; Kim, T.-J.; Park, B., Zero-Strain Intercalation Cathode for Rechargeable Li-Ion Cell. *Angewandte Chemie* **2001,** *113* (18), 3471-3473; (b) Cho, J.; Lee, J.-G.; Kim, B.; Park, B., Effect of P2O5 and AlPO4 Coating on LiCoO2 Cathode Material. *Chemistry of Materials* **2003,** *15* (16), 3190-3193; (c) Cho, J.; Kim, Y.-W.; Kim, B.; Lee, J.-G.; Park, B., A Breakthrough in the Safety of Lithium Secondary Batteries by Coating the Cathode Material with AlPO4 Nanoparticles. *Angewandte Chemie International Edition* **2003,** *42* (14), 1618-1621.

4. Dyer, L. D.; Borie, B. S.; Smith, G. P., Alkali Metal-Nickel Oxides of the Type MNiO2. *Journal of the American Chemical Society* **1954,** *76* (6), 1499-1503.

5. (a) Ohzuku, T.; Ueda, A.; Nagayama, M., Electrochemistry and Structural Chemistry of LiNiO2 (R$\bar{3}$m) for 4 Volt Secondary Lithium Cells. *Journal of The Electrochemical Society* **1993,** *140* (7), 1862-1870; (b) Liu, W.; Oh, P.; Liu, X.; Lee, M.-J.; Cho, W.; Chae, S.; Kim, Y.; Cho, J., Nickel-Rich Layered Lithium Transition-Metal Oxide for High-Energy Lithium-Ion Batteries. *Angewandte Chemie International Edition* **2015,** *54* (15), 4440-4457.

6. Koyama, Y.; Makimura, Y.; Tanaka, I.; Adachi, H.; Ohzuku, T., Systematic Research on Insertion Materials Based on Superlattice Models in a Phase Triangle of LiCoO2 - LiNiO2 - LiMnO2 : I. First-Principles Calculation on Electronic and Crystal Structures, Phase Stability and New LiNi 1 / 2 Mn 1 / 2 O 2 Material. *Journal of The Electrochemical Society* **2004,** *151* (9), A1499-A1506.

7. (a) Ohzuku, T.; Makimura, Y., Layered lithium insertion material of LiCo1/3Ni1/3Mn1/3O2 for lithium-ion batteries. *Chemistry Letters* **2001,** *30* (7), 642-643; (b) Ohzuku, T.; Makimura, Y., Layered Lithium Insertion Material of LiNi1/2Mn1/2O2: A Possible Alternative to LiCoO2 for Advanced Lithium-Ion Batteries. *Chemistry Letters* **2001,** (8), 744-745.

8. Kang, S. H.; Thackeray, M. M., Enhancing the rate capability of high capacity xLi(2)MnO(3) center dot (1-x)LiMO2 (M = Mn, Ni, Co) electrodes by Li-Ni-PO4 treatment. *Electrochemistry Communications* **2009,** *11* (4), 748-751.

9. Yabuuchi, N.; Yoshii, K.; Myung, S.-T.; Nakai, I.; Komaba, S., Detailed Studies of a High-Capacity Electrode Material for Rechargeable Batteries, Li2MnO3−LiCo1/3Ni1/3Mn1/3O2. *J. Am. Chem. Soc.* **2011,** *133* (12), 4404-4419.

10. (a) Xu, B.; Fell, C. R.; Chi, M.; Meng, Y. S., Identifying surface structural changes in layered Li-excess nickel manganese oxides in high voltage lithium ion batteries: A joint experimental and theoretical study. *Energy Environ. Sci.* **2011,** *4* (6), 2223-2233; (b) Oh, P.; Ko, M.; Myeong, S.; Kim, Y.; Cho, J., A Novel Surface Treatment Method and New Insight into Discharge Voltage Deterioration for High-Performance 0.4Li2MnO3–0.6LiNi1/3Co1/3Mn1/3O2 Cathode Materials. *Adv. Energy Mater.* **2014**, n/a-n/a.

11. (a) Huang, R.; Ikuhara, Y. H.; Mizoguchi, T.; Findlay, S. D.; Kuwabara, A.; Fisher, C. A. J.; Moriwake, H.; Oki, H.; Hirayama, T.; Ikuhara, Y., Oxygen-Vacancy Ordering at Surfaces of Lithium

Manganese(III,IV) Oxide Spinel Nanoparticles. *Angewandte Chemie International Edition* **2011,** *50* (13), 3053-3057; (b) Sickafus, K. E.; Wills, J. M.; Grimes, N. W., Structure of Spinel. *Journal of the American Ceramic Society* **1999,** *82* (12), 3279-3292.

12. Xu, B.; Meng, S., Factors affecting Li mobility in spinel LiMn2O4—A first-principles study by GGA and GGA+U methods. *J. Power Sources* **2010,** *195* (15), 4971-4976.

13. Ohzuku, T.; Kitagawa, M.; Hirai, T., Electrochemistry of Manganese Dioxide in Lithium Nonaqueous Cell. *J. Electrochem. Soc.* **1990,** *137* (3), 769-775.

14. (a) Tokura, Y.; Tomioka, Y., Colossal magnetoresistive manganites. *Journal of Magnetism and Magnetic Materials* **1999,** *200* (1–3), 1-23; (b) Yamada, A.; Tanaka, M., Jahn-Teller structural phase transition around 280K in LiMn2O4. *Materials Research Bulletin* **1995,** *30* (6), 715-721.

15. Park, O. K.; Cho, Y.; Lee, S.; Yoo, H.-C.; Song, H.-K.; Cho, J., Who will drive electric vehicles, olivine or spinel? *Energy Environ. Sci.* **2011,** *4* (5), 1621-1633.

16. Wang, X.; Nakamura, H.; Yoshio, M., Capacity fading mechanism for oxygen defect spinel as a 4 V cathode material in Li-ion batteries. *J. Power Sources* **2002,** *110* (1), 19-26.

17. Xia, Y.; Yoshio, M., Studies on Li-Mn-O spinel system (obtained from melt-impregnation method) as a cathode for 4 V lithium batteries Part IV. High and low temperature performance of LiMn2O4. *J. Power Sources* **1997,** *66* (1–2), 129-133.

18. Kanno, R.; Kondo, A.; Yonemura, M.; Gover, R.; Kawamoto, Y.; Tabuchi, M.; Kamiyama, T.; Izumi, F.; Masquelier, C.; Rousse, G., The relationships between phases and structures of lithium manganese spinels. *J. Power Sources* **1999,** *81–82* (0), 542-546.

19. (a) Choi, N.-S.; Chen, Z.; Freunberger, S. A.; Ji, X.; Sun, Y.-K.; Amine, K.; Yushin, G.; Nazar, L. F.; Cho, J.; Bruce, P. G., Challenges Facing Lithium Batteries and Electrical Double-Layer Capacitors. *Angewandte Chemie International Edition* **2012,** *51* (40), 9994-10024; (b) Dunn, B.; Kamath, H.; Tarascon, J.-M., Electrical Energy Storage for the Grid: A Battery of Choices. *Science* **2011,** *334* (6058), 928-935; (c) Thackeray, M. M.; Wolverton, C.; Isaacs, E. D., Electrical energy storage for transportation-approaching the limits of, and going beyond, lithium-ion batteries. *Energy Environ. Sci.* **2012,** *5* (7), 7854-7863.

20. (a) Sun, Y.-K.; Lee, M.-J.; Yoon, C. S.; Hassoun, J.; Amine, K.; Scrosati, B., The Role of AlF3 Coatings in Improving Electrochemical Cycling of Li-Enriched Nickel-Manganese Oxide Electrodes for Li-Ion Batteries. *Adv. Mat.* **2012,** *24* (9), 1192-1196; (b) Gu, M.; Belharouak, I.; Genc, A.; Wang, Z.; Wang, D.; Amine, K.; Gao, F.; Zhou, G.; Thevuthasan, S.; Baer, D. R.; Zhang, J.-G.; Browning, N. D.; Liu, J.; Wang, C., Conflicting Roles of Nickel in Controlling Cathode Performance in Lithium Ion Batteries. *Nano Lett.* **2012,** *12* (10), 5186-5191; (c) Yu, H.; Ishikawa, R.; So, Y.-G.; Shibata, N.; Kudo, T.; Zhou, H.; Ikuhara, Y., Direct Atomic-Resolution Observation of Two Phases in the Li1.2Mn0.567Ni0.166Co0.067O2 Cathode Material for Lithium-Ion Batteries. *Angewandte Chemie International Edition* **2013,** *52* (23), 5969-5973.

21. (a) Makimura, Y.; Ohzuku, T., Lithium insertion material of LiNi1/2Mn1/2O2 for advanced lithium-ion batteries. *J. Power Sources* **2003,** *119–121* (0), 156-160; (b) Sun, Y.-K.; Myung, S.-T.; Park, B.-C.; Prakash, J.; Belharouak, I.; Amine, K., High-energy cathode material for long-life and safe lithium batteries. *Nat Mater* **2009,** *8* (4), 320-324; (c) Cho, Y.; Oh, P.; Cho, J., A New Type of Protective Surface Layer for High-Capacity Ni-Based Cathode Materials: Nanoscaled Surface Pillaring Layer. *Nano Lett.* **2013,** *13* (3), 1145-1152.

22. (a) Wu, C. R.; Fang, X. P.; Guo, X. W.; Mao, Y.; Ma, J.; Zhao, C. C.; Wang, Z. X.; Chen, L. Q.,

Surface modification of Li1.2Mn0.54Co0.13Ni0.13O2 with conducting polypyrrole. *Journal of Power Sources* **2013,** *231*, 44-49; (b) Yabuuchi, N.; Lu, Y. C.; Mansour, A. N.; Chen, S.; Shao-Horn, Y., The Influence of Heat-Treatment Temperature on the Cation Distribution of LiNi0.5Mn0.5O2 and Its Rate Capability in Lithium Rechargeable Batteries. *J. Electrochem. Soc.* **2011,** *158* (2), A192-A200; (c) Croy, J. R.; Kim, D.; Balasubramanian, M.; Gallagher, K.; Kang, S. H.; Thackeray, M. M., Countering the Voltage Decay in High Capacity xLi(2)MnO(3)center dot(1-x)LiMO2 Electrodes (M=Mn, Ni, Co) for Li+-Ion Batteries. *Journal of the Electrochemical Society* **2012,** *159* (6), A781-A790; (d) Wang, J.; Yuan, G. X.; Zhang, M. H.; Qiu, B.; Xia, Y. G.; Liu, Z. P., The structure, morphology, and electrochemical properties of Li1+xNi1/6Co1/6Mn4/6O2.25+x/2 (0.1 <= x <= 0.7) cathode materials. *Electrochimica Acta* **2012,** *66*, 61-66.

23. (a) Jung, Y. S.; Cavanagh, A. S.; Yan, Y. F.; George, S. M.; Manthiram, A., Effects of Atomic Layer Deposition of Al2O3 on the Li Li0.20Mn0.54Ni0.13Co0.13 O-2 Cathode for Lithium-Ion Batteries. *Journal of the Electrochemical Society* **2011,** *158* (12), A1298-A1302; (b) Park, M. S.; Lee, J. W.; Choi, W.; Im, D.; Doo, S. G.; Park, K. S., On the surface modifications of high-voltage oxide cathodes for lithium-ion batteries: new insight and significant safety improvement. *Journal of Materials Chemistry* **2010,** *20* (34), 7208-7213; (c) Zhang, X. F.; Belharouak, I.; Li, L.; Lei, Y.; Elam, J. W.; Nie, A. M.; Chen, X. Q.; Yassar, R. S.; Axelbaum, R. L., Structural and Electrochemical Study of Al2O3 and TiO2 Coated Li1.2Ni0.13Mn0.54Co0.13O2 Cathode Material Using ALD. *Adv. Energy Mater.* **2013,** *3* (10), 1299-1307; (d) Qiao, Q. Q.; Zhang, H. Z.; Li, G. R.; Ye, S. H.; Wang, C. W.; Gao, X. P., Surface modification of Li-rich layered Li(Li0.17Ni0.25Mn0.58)O-2 oxide with Li-Mn-PO4 as the cathode for lithium-ion batteries. *Journal of Materials Chemistry A* **2013,** *1* (17), 5262-5268.

24. (a) Kang, S. H.; Johnson, C. S.; Vaughey, J. T.; Amine, K.; Thackeray, M. M., The effects of acid treatment on the electrochemical properties of 0.5 Li2MnO3 center dot 0.5 LiNi0.44Co0.25Mn0.31O2 electrodes in lithium cells. *J. Electrochem. Soc.* **2006,** *153* (6), A1186-A1192; (b) Xu, G. F.; Li, J. L.; Xue, Q. R.; Ren, X. P.; Yan, G.; Wang, X. D.; Kang, F. Y., Enhanced oxygen reducibility of 0.5Li(2)MnO(3 center dot)0.5LiNi(1/3)Co(1/3)Mn(1/3)O(2) cathode material with mild acid treatment. *J. Power Sources* **2014,** *248*, 894-899; (c) Kim, J. S.; Johnson, C. S.; Vaughey, J. T.; Thackeray, M. M., Pre-conditioned layered electrodes for lithium batteries. *J. Power Sources* **2006,** *153* (2), 258-264.

25. Oh, P.; Myeong, S.; Cho, W.; Lee, M.-J.; Ko, M.; Jeong, H. Y.; Cho, J., Superior Long-Term Energy Retention and Volumetric Energy Density for Li-Rich Cathode Materials. *Nano Lett.* **2014,** *14* (10), 5965-5972.

26. Wu, F.; Li, N.; Su, Y.; Zhang, L.; Bao, L.; Wang, J.; Chen, L.; Zheng, Y.; Dai, L.; Peng, J.; Chen, S., Ultrathin Spinel Membrane-Encapsulated Layered Lithium-Rich Cathode Material for Advanced Li-Ion Batteries. *Nano Lett.* **2014,** *14* (6), 3550-3555.

27. (a) Kim, Y.; Cho, J., Lithium-Reactive Co3 (PO4) 2 Nanoparticle Coating on High-Capacity LiNi0.8Co0.16Al0.04O2 Cathode Material for Lithium Rechargeable Batteries. *J. Electrochem. Soc.* **2007,** *154* (6), A495-A499; (b) Park, M.-H.; Noh, M.; Lee, S.; Ko, M.; Chae, S.; Sim, S.; Choi, S.; Kim, H.; Nam, H.; Park, S.; Cho, J., Flexible High-Energy Li-Ion Batteries with Fast-Charging Capability. *Nano Lett.* **2014,** *14* (7), 4083-4089.

28. Lee, M.-J.; Lee, S.; Oh, P.; Kim, Y.; Cho, J., High Performance LiMn2O4 Cathode Materials Grown with Epitaxial Layered Nanostructure for Li-Ion Batteries. *Nano Lett.* **2014,** *14* (2), 993-999.

29. Thackeray, M. M.; Kang, S. H.; Johnson, C. S.; Vaughey, J. T.; Benedek, R.; Hackney, S. A., Li(2)MnO(3)-stabilized LiMO(2) (M = Mn, Ni, Co) electrodes for lithium-ion batteries. *Journal of Materials Chemistry* **2007,** *17* (30), 3112-3125.

30. Johnson, C. S.; Li, N.; Vaughey, J. T.; Hackney, S. A.; Thackeray, M. M., Lithium-manganese oxide electrodes with layered-spinel composite structures xLi(2)MnO(3)center dot(1-x)Li1+yMn2-yO4 ($0 < x < 1$, $0 <= y <= 0.33$) for lithium batteries. *Electrochemistry Communications* **2005,** *7* (5), 528-536.

31. Wu, F.; Li, N.; Su, Y.; Shou, H.; Bao, L.; Yang, W.; Zhang, L.; An, R.; Chen, S., Spinel/Layered Heterostructured Cathode Material for High-Capacity and High-Rate Li-Ion Batteries. *Adv. Mat.* **2013,** *25* (27), 3722-3726.

32. (a) Ohzuku, T.; Takeda, S.; Iwanaga, M., Solid-state redox potentials for Li[Me1/2Mn3/2]O4 (Me: 3d-transition metal) having spinel-framework structures: a series of 5 volt materials for advanced lithium-ion batteries. *J. Power Sources* **1999,** *81–82* (0), 90-94; (b) Kim, J. H.; Myung, S. T.; Yoon, C. S.; Kang, S. G.; Sun, Y. K., Comparative Study of LiNi0.5Mn1.5O4-δ and LiNi0.5Mn1.5O4 Cathodes Having Two Crystallographic Structures: Fd3̄m and P4332. *Chem. Mat.* **2004,** *16* (5), 906-914; (c) Han, D.-W.; Kang, Y.-M.; Yin, R.-Z.; Song, M.-S.; Kwon, H.-S., Effects of Fe doping on the electrochemical performance of LiCoPO4/C composites for high power-density cathode materials. *Electrochemistry Communications* **2009,** *11* (1), 137-140; (d) Rui, X.; Zhao, X.; Lu, Z.; Tan, H.; Sim, D.; Hng, H. H.; Yazami, R.; Lim, T. M.; Yan, Q., Olivine-Type Nanosheets for Lithium Ion Battery Cathodes. *ACS Nano* **2013,** *7* (6), 5637-5646.

33. Lee, H.-W.; Muralidharan, P.; Ruffo, R.; Mari, C. M.; Cui, Y.; Kim, D. K., Ultrathin Spinel LiMn2O4 Nanowires as High Power Cathode Materials for Li-Ion Batteries. *Nano Lett.* **2010,** *10* (10), 3852-3856.

34. (a) Gummow, R. J.; de Kock, A.; Thackeray, M. M., Improved capacity retention in rechargeable 4 V lithium/lithium-manganese oxide (spinel) cells. *Solid State Ionics* **1994,** *69* (1), 59-67; (b) Pasquier, A. D.; Blyr, A.; Courjal, P.; Larcher, D.; Amatucci, G.; Gerand, B.; Tarascon, J.-M., Mechanism for Limited 55[degree]C Storage Performance of Li[sub 1.05]Mn[sub 1.95]O[sub 4] Electrodes. *J. Electrochem. Soc.* **1999,** *146* (2), 428-436; (c) Xia, Y.; Zhou, Y.; Yoshio, M., Capacity Fading on Cycling of 4 V Li / LiMn2 O 4 Cells. *J. Electrochem. Soc.* **1997,** *144* (8), 2593-2600; (d) Kim, J.-S.; Kim, K.; Cho, W.; Shin, W. H.; Kanno, R.; Choi, J. W., A Truncated Manganese Spinel Cathode for Excellent Power and Lifetime in Lithium-Ion Batteries. *Nano Lett.* **2012,** *12* (12), 6358-6365.

35. (a) Liu, D.-Q.; Liu, X.-Q.; He, Z.-Z., The elevated temperature performance of LiMn2O4 coated with Li4Ti5O12 for lithium ion battery. *Materials Chemistry and Physics* **2007,** *105* (2–3), 362-366; (b) Park, S. B.; Shin, H. C.; Lee, W.-G.; Cho, W. I.; Jang, H., Improvement of capacity fading resistance of LiMn2O4 by amphoteric oxides. *J. Power Sources* **2008,** *180* (1), 597-601; (c) Cho, J.; Kim, Y. J.; Kim, T.-J.; Park, B., Enhanced Structural Stability of o-LiMnO2 by Sol−Gel Coating of Al2O3. *Chem. Mat.* **2000,** *13* (1), 18-20; (d) Arumugam, D.; Paruthimal Kalaignan, G., Synthesis and electrochemical characterizations of Nano-SiO2-coated LiMn2O4 cathode materials for rechargeable lithium batteries. *Journal of Electroanalytical Chemistry* **2008,** *624* (1–2), 197-204; (e) Liu, Y.; Lv, J.; Fei, Y.; Huo, X.; Zhu, Y., Improvement of storage performance of LiMn2O4/graphite battery with AlF3-coated LiMn2O4. *Ionics* **2013,** *19* (9), 1241-1246; (f) Lim, S.; Cho, J., PVP-Assisted ZrO2 coating on LiMn2O4 spinel cathode nanoparticles prepared by MnO2 nanowire templates. *Electrochemistry Communications* **2008,** *10* (10), 1478-1481.

36. Lee, S.; Cho, Y.; Song, H.-K.; Lee, K. T.; Cho, J., Carbon-Coated Single-Crystal LiMn2O4 Nanoparticle Clusters as Cathode Material for High-Energy and High-Power Lithium-Ion Batteries. *Angewandte Chemie International Edition* **2012,** *51* (35), 8748-8752.

37. (a) Myung, S.-T.; Lee, K.-S.; Kim, D.-W.; Scrosati, B.; Sun, Y.-K., Spherical core-shell Li[(Li0.05Mn0.95)0.8(Ni0.25Mn0.75)0.2]2O4 spinels as high performance cathodes for lithium batteries. *Energy Environ. Sci.* **2011,** *4* (3), 935-939; (b) Cho, J.; Kim, G. B.; Lim, H. S.; Kim, C. S.;

Yoo, S. I., Improvement of Structural Stability of LiMn2 O 4 Cathode Material on 55 ° C Cycling by Sol-Gel Coating of LiCoO2. *Electrochemical and Solid-State Letters* **1999,** *2* (12), 607-609; (c) Yuan, Y. F.; Wu, H. M.; Guo, S. Y.; Wu, J. B.; Yang, J. L.; Wang, X. L.; Tu, J. P., Preparation, characteristics and electrochemical properties of surface-modified LiMn2O4 by doped LiNi0.05Mn1.95O4. *Applied Surface Science* **2008,** *255* (5, Part 1), 2225-2229.

38. (a) Hinuma, Y.; Meng, Y. S.; Kang, K.; Ceder, G., Phase Transitions in the LiNi0.5Mn0.5O2 System with Temperature. *Chem. Mat.* **2007,** *19* (7), 1790-1800; (b) Park, B. C.; Bang, H. J.; Yoon, C. S.; Myung, S. T.; Prakash, J.; Sun, Y. K., Structural transformation of Li Ni0.5-xCo2xMn0.5-x O-2 (2x <= 0.1) charged in high-voltage range (4.5 V). *J. Electrochem. Soc.* **2007,** *154* (6), A520-A526.

39. Chen, Z.; Dahn, J. R., Studies of LiCoO2 Coated with Metal Oxides. *Electrochemical and Solid-State Letters* **2003,** *6* (11), A221-A224.

40. (a) Lee, J. H.; Hong, J. K.; Jang, D. H.; Sun, Y. K.; Oh, S. M., Degradation mechanisms in doped spinels of LiM0.05Mn1.95O4 (M=Li, B, Al, Co, and Ni) for Li secondary batteries. *J. Power Sources* **2000,** *89* (1), 7-14; (b) Lee, S.; Jeong, M.; Cho, J., Optimized 4-V Spinel Cathode Material with High Energy Density for Li-Ion Cells Operating at 60 °C. *Adv. Energy Mater.* **2013**, n/a-n/a.

41. (a) Wang, J.; Neaton, J. B.; Zheng, H.; Nagarajan, V.; Ogale, S. B.; Liu, B.; Viehland, D.; Vaithyanathan, V.; Schlom, D. G.; Waghmare, U. V.; Spaldin, N. A.; Rabe, K. M.; Wuttig, M.; Ramesh, R., Epitaxial BiFeO3 Multiferroic Thin Film Heterostructures. *Science* **2003,** *299* (5613), 1719-1722; (b) Hirayama, M.; Ido, H.; Kim, K.; Cho, W.; Tamura, K.; Mizuki, J. i.; Kanno, R., Dynamic Structural Changes at LiMn2O4/Electrolyte Interface during Lithium Battery Reaction. *J. Am. Chem. Soc.* **2010,** *132* (43), 15268-15276.

42. Thackeray, M. M., Structural Considerations of Layered and Spinel Lithiated Oxides for Lithium Ion Batteries. *J. Electrochem. Soc.* **1995,** *142* (8), 2558-2563.

43. Jiao, F.; Harrison, A.; Hill, A. H.; Bruce, P. G., Mesoporous Mn2O3 and Mn3O4 with Crystalline Walls. *Adv. Mat.* **2007,** *19* (22), 4063-4066.

44. Cho, Y.; Lee, S.; Lee, Y.; Hong, T.; Cho, J., Spinel-Layered Core-Shell Cathode Materials for Li-Ion Batteries. *Adv. Energy Mater.* **2011,** *1* (5), 821-828.

45. Shaju, K. M.; Bruce, P. G., A Stoichiometric Nano-LiMn2O4 Spinel Electrode Exhibiting High Power and Stable Cycling. *Chem. Mat.* **2008,** *20* (17), 5557-5562.

46. (a) Cho, J.; Thackeray, M. M., Structural changes of LiMn2O4 spinel electrodes during electrochemical cycling. *J. Electrochem. Soc.* **1999,** *146* (10), 3577-3581; (b) Thackeray, M. M.; Shao-Horn, Y.; Kahaian, A. J.; Kepler, K. D.; Skinner, E.; Vaughey, J. T.; Hackney, S. A., Structural Fatigue in Spinel Electrodes in High Voltage (4 V) Li / Li x Mn2 O 4 Cells. *Electrochemical and Solid-State Letters* **1998,** *1* (1), 7-9.

47. Noh, H.-J.; Youn, S.; Yoon, C. S.; Sun, Y.-K., Comparison of the structural and electrochemical properties of layered Li[NixCoyMnz]O2 (x = 1/3, 0.5, 0.6, 0.7, 0.8 and 0.85) cathode material for lithium-ion batteries. *J. Power Sources* **2013,** *233* (0), 121-130.

48. (a) Weppner, W.; Huggins, R. A., DETERMINATION OF THE KINETIC PARAMETERS OF MIXED-CONDUCTING ELECTRODES AND APPLICATION TO THE SYSTEM Li//3Sb. *J. Electrochem. Soc.* **1977,** *124* (10), 1569-1578; (b) Shaju, K. M.; Subba Rao, G. V.; Chowdari, B. V. R., Li ion kinetic studies on spinel cathodes, Li(M1/6Mn11/6)O4 (M = Mn, Co, CoAl) by GITT and EIS. *J. Mater. Chem.* **2003,** *13* (1), 106-113.

49. Bard, A. J.; Faulkner, L. R., *Electrochemical methods: fundamentals and applications*. Wiley New York: 1980; Vol. 2.

50. Lee, K. T.; Jeong, S.; Cho, J., Roles of Surface Chemistry on Safety and Electrochemistry in Lithium Ion Batteries. *Acc. Chem. Res.* **2012,** *46* (5), 1161-1170.

51. Li, J.; Zhu, Y.; Wang, L.; Cao, C., Lithium Titanate Epitaxial Coating on Spinel Lithium Manganese Oxide Surface for Improving the Performance of Lithium Storage Capability. *ACS Applied Materials & Interfaces* **2014,** *6* (21), 18742-18750.

52. (a) Hosono, E.; Kudo, T.; Honma, I.; Matsuda, H.; Zhou, H., Synthesis of Single Crystalline Spinel LiMn2O4 Nanowires for a Lithium Ion Battery with High Power Density. *Nano Lett.* **2009,** *9* (3), 1045-1051; (b) Cheng, F.; Wang, H.; Zhu, Z.; Wang, Y.; Zhang, T.; Tao, Z.; Chen, J., Porous LiMn2O4 nanorods with durable high-rate capability for rechargeable Li-ion batteries. *Energy Environ. Sci.* **2011,** *4* (9), 3668-3675; (c) Ding, Y.-L.; Xie, J.; Cao, G.-S.; Zhu, T.-J.; Yu, H.-M.; Zhao, X.-B., Single-Crystalline LiMn2O4 Nanotubes Synthesized Via Template-Engaged Reaction as Cathodes for High-Power Lithium Ion Batteries. *Adv. Funct. Mater.* **2011,** *21* (2), 348-355; (d) Ding, Y.-L.; Zhao, X.-B.; Xie, J.; Cao, G.-S.; Zhu, T.-J.; Yu, H.-M.; Sun, C.-Y., Double-shelled hollow microspheres of LiMn2O4 for high-performance lithium ion batteries. *J. Mater. Chem.* **2011,** *21* (26), 9475-9479.

53. (a) Smart, M. C.; Ratnakumar, B. V.; Surampudi, S., Electrolytes for Low-Temperature Lithium Batteries Based on Ternary Mixtures of Aliphatic Carbonates. *J. Electrochem. Soc.* **1999,** *146* (2), 486-492; (b) Plichta, E. J.; Hendrickson, M.; Thompson, R.; Au, G.; Behl, W. K.; Smart, M. C.; Ratnakumar, B. V.; Surampudi, S., Development of low temperature Li-ion electrolytes for NASA and DoD applications. *J. Power Sources* **2001,** *94* (2), 160-162.

54. (a) Sides, C. R.; Martin, C. R., Nanostructured Electrodes and the Low-Temperature Performance of Li-Ion Batteries. *Adv. Mat.* **2005,** *17* (1), 125-128; (b) Zhang, S. S.; Xu, K.; Jow, T. R., The low temperature performance of Li-ion batteries. *J. Power Sources* **2003,** *115* (1), 137-140.

Publications

1. Yang-Kook Sun*, **Min-Joon Lee**, Chong S. Yoon*, Jusef Hassoun, Khalil Amine, Bruno Scrosati*, The Role of AlF_3 Coatings in Improving Electrochemical Cycling of Li-Enriched Nickel-Manganese Oxide Electrodes for Li-Ion Batteries, ***Advanced Materials*** 2012; 24, 1192–1196.

2. **Min-Joon Lee**, Sanghan Lee, Pilgun Oh, Youngsik Kim, Jaephil Cho*, High Performance LiMn2O4 Cathode Materials Grown with Epitaxial Layered Nanostructure for Li-Ion Batteries, ***Nano letters*** 2014; 14, 993-999.

3. Pilgun Oh, Seungjun Myeong, Woongrae Cho, **Min-Joon Lee**, Minseong Ko, Hu Young Jeong, Jaephil Cho*, Superior Long-Term Energy Retention and Volumetric Energy Density for Li-Rich Cathode Materials, ***Nano letters*** 2014;14, 5965-5972.

4. Sanghan Lee, Gabin Yoon, Minseul Jeong, **Min-Joon Lee**, Kisuk Kang, Jaephil Cho*, Hierarchical Surface Atomic Structure of a Manganese-Based Spinel Cathode for Lithium-Ion Batteries, ***Angewandte Chemie International Edition*** 2015; 54, 1153-1158.

5. Wen Liu, Pilgun Oh, Xien Liu, **Min-Joon Lee**, Woongrae Cho, Sujong Chae, Youngsik Kim, Jaephil Cho*, Nickel-Rich Layered Lithium Transition-Metal Oxide for High-Energy Lithium-Ion Batteries, ***Angewandte Chemie International Edition*** 2015; 54, 4440-4457.

6. Minseul Jeong, **Min-Joon Lee**, Jaephil Cho* and Sanghan Lee*, Surface Mn Oxidation State Controlled Spinel $LiMn_2O_4$ as a Cathode Material for High-Energy Li-Ion Batteries, ***Advanced Energy Materials*** 2015; DOI: 10.1002/aenm.201500440.

7. Hyungki Kim, Yoonkook Son, Chibeom Park, **Min-Joon Lee**, Misun Hong, Jungah Kim, Minkyung Lee, Jaephil Cho*, and Hee Cheul Choi*, Germanium Silicon Alloy Anode Material Capable of Tunable Overpotential by Nanoscale Si Segregation, ***Nano letters*** 2015; DOI: 10.1021/acs.nanolett.5b01257.

8. **Min-Joon Lee**†, Mijung Noh†, Mi-Hee Park, Minki Jo, Hyejung Kim, Haisol Nam, Jaephil Cho* Role of Nanoscale-range Vanadium Treatment on $LiNi_{0.8}Co_{0.15}Al_{0.05}O_2$ Cathode Materials for Liion Batteries at Elevated Temperatures, ***Journal of Materials Chemistry A*** 2015; DOI: 10.1039/C5TA01974E. (†Equally contribution) DOI: 10.1039/C5TA01974E.

Acknowledgements

NESM에 온지 벌써3년이 다 되어갑니다. 입학한지가 엊그제 같은데 벌써 졸업이라니…많은 것을 배우고 느끼고 얻어나가는 것 같습니다. 박사과정 동안 곁에서 항상 도와주시고 신경 써 주셨던 모든 분들을 꼭 기억하고 더 크게 보답하고 싶습니다.

먼저 박사과정동안 부족한 저를 지도해주신 조재필 교수님.

많은 가르침을 받은 것 같습니다. 교수님의 사랑과 격려에 언제나 감사드리며, 특히 교수님께 배운 열정이 제가 사회에 나가서 쓸 수 있는 가장 큰 무기가 될 것 같습니다.

졸업하신 용현이형, 상한형, 장수형, 정수경형, 그리고 노미정누나.

언제나 물심양면으로 도와주시고 귀한 조언 주신 것 감사드립니다. 특히 스피넬 팀 왕사수 이상한형. 형한테 정말 많은 것을 배운 것 같아요. 지금도 자주 연락하고 있지만 앞으로도 더 자주 연락드릴께요.

그 밖에 졸업하신 후배님들 및 연구실 랩원들.

열심히 해라.

Jul. 2015